Graphene-Based Nanophotonic Structures

by

Seyyed Mohsen Raeis Zadeh Bajestani

A thesis
presented to the University of Waterloo
in fulfillment of the
thesis requirement for the degree of
Doctor of Philosophy
in
Electrical and Computer Engineering

Waterloo, Ontario, Canada, 2016

I hereby declare that I am the sole author of this thesis. This is a true copy of the thesis, including any required final revisions, as accepted by my examiners.

Abstract

Terahertz (THz) technology offers a rich playground for a vast number of research topics and applications. High resolution imaging for biomedical applications, long-wavelength spectroscopy for interstellar applications, security monitoring, communication, quality control, and process monitoring are just among a few possible applications of the THz technology. While the lack of an efficient source is a huge obstacle in flourishing of THz technology, the potentially huge impact of THz technology in many areas of every day human life has motivated extensive world-wide research efforts in this area. In response to the widespread need for the cost-effective miniaturized THz active devices, this thesis describes theoretical and practical methods developed for the analysis, the design optimization, and the fabrication of a graphene-based THz photomixing sources.

The main contributions, from an analysis point of view, include a new computationally efficient multipole-based method with a surface boundary condition (SBC) to analyze the wave interaction with graphene and also development of a comprehensive theoretical model for modeling of the difference frequency generation (DFG) in graphene. The proposed multipole-based method is deployed to find the linear interaction of light with graphene and also to verify the volumetric model that will be used in the design optimization of the THz photomixing structure. In the nonlinear analysis, symmetry breaking and the advent of second order processes such as the DFG in graphene are discussed in detail. I, specifically, explore the role of DC biasing and the wave momentum as two mechanisms effective in symmetry breaking. As a result, nonlinear conductivity of the graphene layer is calculated for an obliquely incident wave and in the presence of a DC current using a quantum mechanical approach.

From a design optimization point of view, design of a new nanoplasmonic structure for the DFG enhancement and a THz antenna for the efficient radiation of the generated THz signal are the main focuses of this work. I start by verifying the plasmon enhanced wave interaction with the graphene layer via the Raman spectroscopy. Next, I use the obtained nonlinearity in conjunction with the volumetric model to design and analyze the complex structure of photomixer in the perturbation limit. The nonlinear analysis shows the achievable THz power of $1\mu W$ from an incident laser pulse with the fluence of $15mW/cm^2$. I then investigate the effect of designed log-periodic antenna and I show how the antenna can be used to control the generated THz power.

Finally, the new recipe developed for the fabrication of the graphene-based photomixer structure is presented. The developed recipe ensures a reliable and repeatable fabrication process even for large area graphene devices. In addition, a comparison between the de-

veloped recipe and those typically used in nanofabrication is depicted. This work ends by showing the measurement setups and the measurement results for the fabricated devices.

Acknowledgements

He is Allah, the One and Only
Allah, the Eternal, Absolute
He begets not, not is he begotten
and there is non comparable unto him. (Quran 112:1-4)

This thesis is the result of the help and support of many amazing colleagues whom I had a pleasure to work with. First and foremost, I thank my supervisor, Professor Safieddin (Ali) Safavi-Naeini. The encouragement and motivation he provided me during my work and at the time of adversity was exemplary. It has been a fantastic experience working with Ali whose solid diverse knowledge and intuition in new applications have brought about fascinating new topics and research approaches to our group. After five years of working with him, I am still amazed by how much he is capable of.

I am indebted to Reza Khorasani, who has taught me most of what I know about the fabrication. As a new student, I was following him in the lab and he was kind and supportive to explain everything in detail to me. It was his unstopping tenacious work that gave me the encouragement for the fabrications I have done later on. It was a real pleasure to work with him. In addition to guidance from Reza, I have learned a great deal from Dr. Nathan Fitzpatrick, Brian Goddard, Rod Salandanan, and Dr. Anita Fadavi. I should also thank Alireza Zandieh, who spent much of his free time to teach me about the TDS setup and the optical lab measurements.

Thank you to Professor Donna Strickland, whom I had a pleasure to work with for a short yet a valuable period. When it comes to nonlinear measurement, she is a magician that I aspire to be, one day. I am really grateful to my Committee Members; Professors Dayan Ban, Simarjeet Saini, and Matteo Mariantoni. My special thanks to professor Ban for allowing me to use his lab for TDS measurements.

Last but not least, my special thanks to group CIARS members; Chris Schroeder for her administrative support and revising my thesis; Aidin Taeb and Mehrbod Mohajer who taught me about life and I had their support with the VNA and the laser machine; Behrooz Semnani and Mohammad Haghtalab whom I had a pleasure to do collaboration with; Naeimeh Ghafarian who taught me how to transfer graphene; Hussam Al-Saedi who cheered me up when I was down and had the patience to hear me when I most needed it. With special thanks to my close friends Hadi Amarloo and Dr. Wael M. Abdel-Wahab who were (and absolutely are) always there to support me and had the patience to participate in my discussions and to lead me through different topic of research and life.

I am forever indebted to my family for the love and support they provide. The best compliments in words pale in comparison to the sacrifice they have made. I just want them to know how much I love them.

Dedicated to my Parents,

S. Hossein Raeis-Zadeh

Tahereh Mokhtari

Table of Contents

List of Figures

List of Tables

Chapter 1

Introduction

Two dimensional (2D) materials or 3D anomalies [1] offer unique electrical and thermal properties because of the plane-confined heat and charge transfer. From a chronological point of view, the first member of 2D materials is graphene which was discovered in 2004 by Geim and Novoselov. Since their ground breaking experiment, every now and then, a new allotrope is added to the list of 2D crystals. Hexagonal boron nitride, germanane, molybdnum disolphyte (MoS_2), and WSe_2 are among the most studied 2D crystals [2].

Beside their amazing capability in device miniaturization, each of these materials offers inherently unique properties such as high carrier mobility [3–5], controllable band gap [6], and flexibility [7] that can surpass the commercialized Si and $GaAs$ technologies. No need to mention the importance of mobility in the device speed, controllable band gap in electro-optic interaction, and the flexibility in every day life applications [7].

Historically, $LTGaAs$ was among the first materials used for terahertz (THz) wave generation. As a result of its high carrier mobility, it is possible to generate short pulses extended to the THz range of frequency. However, the loss of $LTGaAs$ in THz range is a fundamental drawback preventing the realization of a fully integrated THz chip. Having the concept of replacing the bulky materials with the 2D counterparts for miniaturization, one can think of graphene as a replacement for $LTGaAs$. The higher mobility of graphene as compared to that of $LTGaAs$ and the feasibility of integration with Si technology are the attractive factors to investigate a graphene-based THz generator. In this thesis, I have performed a comprehensive study and investigation of such a device from both analytical and experimental points of view.

1.1 The physics of graphene

Carbon atom, one of the most abundant elements in the universe, has different allotropes, each of which has distinct and interesting features. Among them, diamond, graphite, and carbon nano-tubes are well-known structures. The graphite layer, particularly, is made of stacks of two dimensional carbon sheets which are bounded by weak Van der Waals forces. Each layer of these two dimensional carbon sheets is known as graphene. The existence of isolated two dimensional crystal structures, e. g. graphene, was presumed to be impossible due to the thermal effects in a low-dimensional system [8]. However, in 2004, a trivial yet clever process involving the peel off of the graphite was proposed to isolate islands of graphene [9].

Graphene is atomic layer thick substance in which the carbon atoms are arranged in hexagonal structures (Figure 1.1 (a)). The distance between two adjacent carbon atoms is $a = 1.42$. Each carbon atom has three covalent bonds with the neighboring atoms in a sp^2 configuration leaving one free electron in the p_z orbital. The electrons bounded by covalent bonding barely contribute to the electrical properties of graphene. The electron in the p_z orbital, however, has the most contribution to electrical and optical properties.

1.1.1 The crystal structure of graphene

The honeycomb lattice of graphene is shown in Figure 1.1 (a). It can be verified that the honeycomb structure is a Bravais lattice with a basis including two adjacent carbon atoms. The direct lattice translation vectors are (The whole structure of lattice can be built by translating the basis along an integer multiple of these vectors):

$$\mathbf{a}_1 = \frac{3a}{2}(1, 1/\sqrt{3}) \tag{1.1}$$

$$\mathbf{a}_2 = \frac{3a}{2}(1, -1/\sqrt{3}) \tag{1.2}$$

where $a = 1.42$ is the lattice constant. The Berillouin zone of graphene crystal and its translation vectors $\mathbf{b}_1$ and $\mathbf{b}_2$ are plotted in Figure 1.1 (b). The vectors $\mathbf{b}_1$ and $\mathbf{b}_2$ are as follows:

$$\mathbf{b}_1 = \frac{2\pi}{3a}(1, \sqrt{3}) \tag{1.3}$$

$$\mathbf{b}_2 = \frac{2\pi}{3a}(1, -\sqrt{3}) \tag{1.4}$$

As we will see shortly, the two point K and K' (denoted as Dirac points) are very important to describe the electronic properties of graphene. The location of these two points in the reciprocal space are,

$$\mathbf{K} = \frac{2\pi}{3a}(1, 1/\sqrt{3})$$
$$\mathbf{K}' = \frac{2\pi}{3a}(1, -1/\sqrt{3}).$$

1.2 The band-structure of graphene

The band-diagram of graphene, obtained using the tight-binding method and considering the nearest neighbor and the next nearest neighbor hopping, is as follows [10]:

$$E(\vec{k}) = \pm t\sqrt{3 + f(\vec{k})} - t' f(\vec{k}), \quad (t < 0, t' > 0)$$
$$f(\vec{k}) = e^{j\mathbf{k}.\delta_1} + e^{j\mathbf{k}.\delta_2} + e^{j\mathbf{k}.\delta_3} \tag{1.5}$$

where $t = 3eV$ and $t' = 0$ are the nearest neighbors and the next nearest neighbor hopping energies. Vector $\vec{k}$ is the electron wave vector on the graphene plane and the vectors $\boldsymbol{\delta}_1 - \boldsymbol{\delta}_3$ are shown in Figure 1.1. The energy band-diagram of graphene in the Berillouin zone is plotted in Figure 1.2. The intersection points of the valance and the conduction bands, known as Dirac points, are important in dynamics of electron in the low energy limit. Inset of Figure 1.2 shows the enlarged picture of band-diagram near one of these points. The cone-shape structure of band-diagram near these points suggest the existence of massless Dirac fermion near the Dirac points K and K'.

Since all the carriers are bounded to the region near the Dirac points in the low energy limit, we only need Hamiltonian around these points to describe the carriers transfer and scattering. The Hamiltonian of graphene around the Dirac points K and K' can be conveniently written as [10]:

$$H_0 = \begin{pmatrix} 0 & k_x - \xi k_y \\ k_x + \xi k_y & 0 \end{pmatrix} \tag{1.6}$$

where H_0 is the Hamiltonian of the free standing graphene layer, $\xi = 1$ for the Dirac cone K and $\xi = -1$ for the Dirac cone K'. The Hamiltonian equation, near the Dirac points, can also be written as follows:

$$H_0\psi(\mathbf{r}) = \mathcal{E}\psi(\mathbf{r})$$
$$H_0 = \nu_F(\hat{p}_x\sigma_x + \xi\hat{p}_y\sigma_y) \tag{1.7}$$

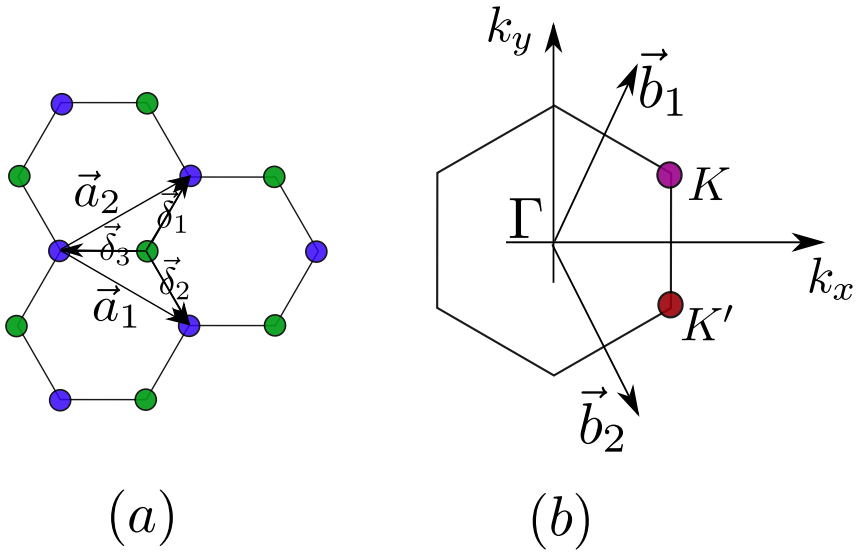

Figure 1.1: The direct (a) and the reciprocal (b) lattice of graphene.

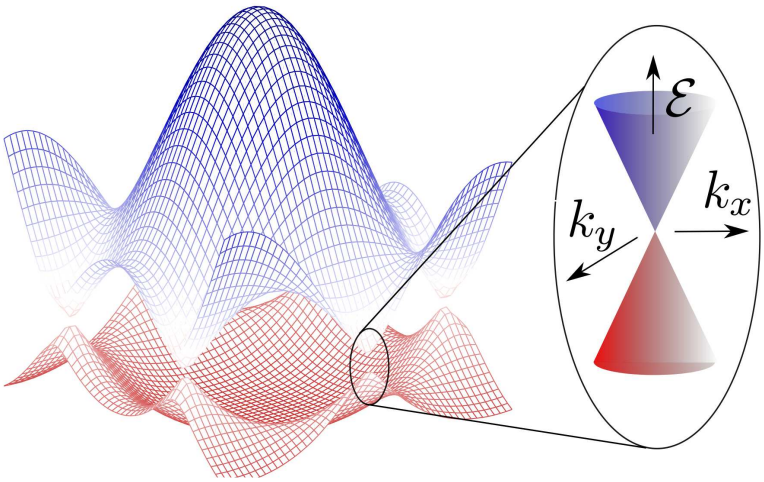

Figure 1.2: The band-diagram of graphene. The inset shows the cone-shaped band-diagram near the Dirac points.

where $\nu_F \approx c/300$ is the Fermi velocity in graphene, $\boldsymbol{\sigma}$'s are the Pauli matrices, $\mathcal{E}$ is the energy of the electron, and $\psi(\mathbf{r})$ is the electron spinor in graphene. For an infinite graphene layer, the eigenfunctions of the Dirac equation 1.7 are [10]:

$$\Psi_{\pm,K} = \frac{1}{\sqrt{2}} \begin{pmatrix} e^{-j\phi/2} \\ \pm e^{j\phi/2} \end{pmatrix} e^{j(\vec{k}.\vec{r}-\mathcal{E}/\hbar t)}, \qquad \Psi_{\pm,K'} = \frac{1}{\sqrt{2}} \begin{pmatrix} e^{j\phi/2} \\ \pm e^{-j\phi/2} \end{pmatrix} e^{j(\vec{k}.\vec{r}-\mathcal{E}/\hbar t)} \tag{1.8}$$

where ϕ is the propagation angle of electron with respect to the $x-$axis. From the wave functions of Eq. 1.8, one can deduce the massless fermionic nature of carriers in graphene since the propagation of carriers resemble the plain wave solutions of the Maxwell's equations. Although the Taylor's expansion of the graphene's Hamiltonian (the Dirac equation) might not provide a complete description of the carrier transport, the Dirac equation is sufficient for describing different set of exceptional quantum effects such as chiral tunneling, surface states, biasing magnetic field effect, anomalous integer quantum Hall effect, and spin-orbit coupling in graphene. The electron wave propagation in graphene nanoribbons, zigzag or armchair, can also be studied using the Dirac equation.

To complete our introduction to the Dirac equation, the probability density and the current probability density should be presented. It is straightforward to confirm that the Dirac equation supports the following continuity equation [10]:

$$\frac{\partial}{\partial t}\left[e\boldsymbol{\Psi}^\dagger\boldsymbol{\Psi}\right] + e\nabla.\left(\nu_F\boldsymbol{\Psi}^\dagger\sigma_\mu\boldsymbol{\Psi}\hat{x}^\mu\right) = 0 \tag{1.9}$$

where

$$\rho = \boldsymbol{\Psi}^\dagger\boldsymbol{\Psi} \tag{1.10}$$

is the electron probability density and

$$j_\mu = e\nu_F\boldsymbol{\Psi}^\dagger\sigma_\mu\boldsymbol{\Psi} \tag{1.11}$$

shows the current probability density. Defined $\hat{x}^\mu$ vector can be wither $\hat{x}$ or $\hat{y}$. The expectation value of the current density $\langle j_\mu \rangle$ is important in establishing a macroscopic model. The most common model for graphene is based on the surface conductivity model derived from the relation between $\langle j_\mu \rangle$ and the electric field.

1.2.1 The quantum-physical modeling of the graphene's surface conductivity

To model the interaction of the electromagnetic field with graphene, one can either incorporate the electromagnetic potentials into the Dirac equation or insert the macroscopic

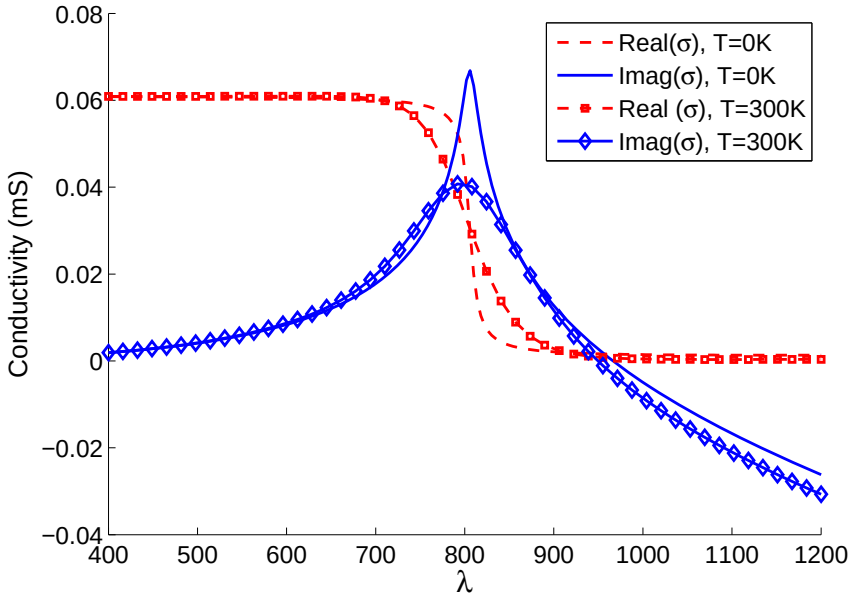

Figure 1.3: The real (dashed lines) and the imaginary (the continuous lines) parts of the graphene's conductivity for $T = 0K$ and $T = 300K$.

constitutive parameters of graphene, e.g. permittivity and permeability, into the Maxwell's equations. The former requires the inclusion of electromagnetic wave and electron wave simultaneously, which is a sophisticated problem to deal with. The latter is a more convenient approach based on the assumption that the electromagnetic field does not change the band structure of the graphene. Through the course of this research, I have always used the second approach.

Considering the zero band-gap of the graphene layer, there is always a conductivity current on its surface. Since the flow of current is confined to the surface of graphene, which is only one atom thick, the current can be modeled as a surface current. Since the effective thickness of graphene $\Delta < 1nm$, such an assumption is valid from the microwaves range of frequencies to the visible light. The effect of this surface current on the electromagnetic field can be considered as a discontinuity in the magnetic field as follows:

$$\hat{n} \times (\vec{\mathscr{H}_1}(\vec{r}, t) - \vec{\mathscr{H}_2}(\vec{r}, t)) = \vec{\mathscr{J}_s}(\vec{r}, t). \tag{1.12}$$

where $\hat{n}$ is a unit vector perpendicular to the surface of graphene, $\vec{\mathscr{H}_1}$ and $\vec{\mathscr{H}_2}$ are the magnetic fields at either sides of the graphene layer, and $\vec{\mathscr{J}_s}$ is the surface current on the

graphene layer. The vector $\vec{\mathscr{J}}_s(\vec{r},t)$ in Eq. 1.12, can be locally approximated as:

$$\vec{J}_s(\vec{r},\omega) = \bar{\bar{\sigma}}(\vec{r},\omega).\vec{E}(\vec{r},\omega) \tag{1.13}$$

where $\bar{\bar{\sigma}}$ is the conductivity tensor of graphene and $\vec{E}(\vec{r},\omega)$ is the electric field on the graphene layer. When there is no external magnetic field, the tensor $\bar{\bar{\sigma}}$ reduces to a scalar given below (Assuming a time harmonic of the from $e^{-i\omega t}$) [11, 12]:

$$\begin{aligned}\sigma(\omega, E_F, \Gamma, T) =& \frac{ie^2(\omega - i\Gamma)}{\pi\hbar^2}\left\{\frac{1}{(\omega - i\Gamma)^2}\int_0^\infty \mathcal{E}\left(\frac{\partial f_d(\mathcal{E})}{\partial\mathcal{E}} - \frac{\partial f_d(-\mathcal{E})}{\partial\mathcal{E}}d\mathcal{E}\right)\right. \\ &\left. - \int_0^\infty \frac{f_d(-\mathcal{E}) - f_d(\mathcal{E})}{(\omega - i\Gamma)^2 - 4(\mathcal{E}/\hbar)^2}\right\}\end{aligned} \tag{1.14}$$

where $\hbar$ is the reduced Planck constant, e is the electron charge, E_F is the Fermi energy level of the graphene layer, Γ is a phenomenological constant of scattering rate at the graphene's surface, and T is the temperature of the graphene layer. Function $f_d(\mathcal{E})$ is the Fermi-Dirac distribution:

$$f_d(\mathcal{E}) = \frac{1}{e^{(\mathcal{E}-E_F)/k_BT} + 1} \tag{1.15}$$

where k_B is the Boltzmann's constant. In Eq. 1.14, the approximate derivative $\frac{\partial f_d(\mathcal{E})}{\partial\mathcal{E}}d\mathcal{E}$ is substituted for the actual probability difference of electrons in the conduction or the valance band $f_d(\mathcal{E}+d\mathcal{E}) - f_d(\mathcal{E})$, which represents the probability of intraband transitions. The first integration in Eq. 1.14 represents the contribution of intraband transitions while the second one is due to the effect of interband transitions. The conductivity at zero temperature can be represented analytically as follows [12, 13]:

$$\sigma(\omega) = -\frac{e^2E_F}{\pi\hbar^2}\frac{i}{\omega - i\tau^{-1}} + \frac{e^2}{4\hbar}\left\{\theta(\hbar\omega - 2E_F) - \frac{i}{\pi}ln\left|\frac{\hbar\omega - 2E_F}{\hbar\omega + 2E_F}\right|\right\} \tag{1.16}$$

where $\tau^{-1} = \Gamma$ and $\theta(t)$ is the Heaviside step function. We always use $\tau = 10^{-13}$ which was extracted from the dc-mobility of the graphene layer at $E_F = 100meV$ [14, 15]. The first term in Eq. 1.16 is the same as the Drude model for metals [16] and comes from the intraband transitions. The second term of Eq. 1.16 shows the effect of interband transitions mostly contributing to the absorption losses. As the photon energy reached $2E_F$, there is a sudden increase in the conductivity loss of the graphene layer due to the contribution of the second term (the step function $\theta((\hbar\omega - 2E_F))$).

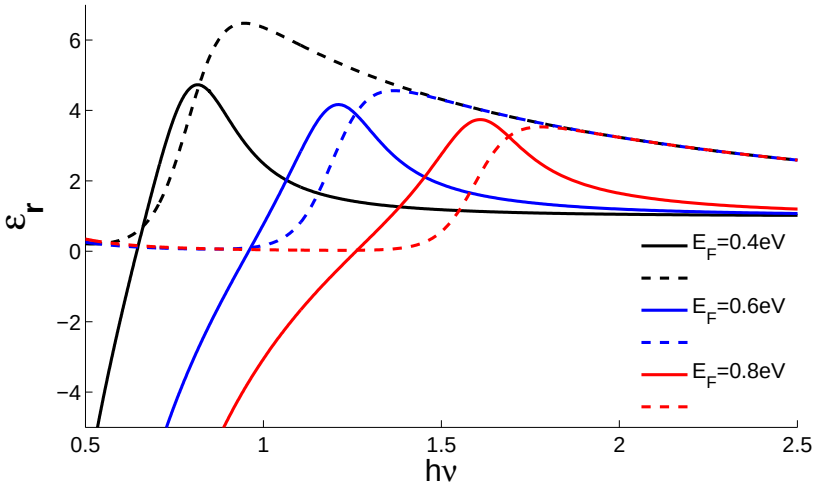

Figure 1.4: The real (solid lines) part and the imaginary (dashed lines) part of the permittivity of the graphene layer for three different values of the Fermi energy level $E_F = 0.4eV$, $E_F = 0.6eV$, and $E_F = 0.8eV$ ($\Delta = 0.7nm$).

Substituting Fermi-Dirac distribution function into Eq. 1.14, one can find the following simple form for the conductivity [13, 17]:

$$\begin{aligned}\sigma(\omega) =& \frac{2e^2 k_B T}{\pi\hbar^2}\frac{i}{\omega - i\tau^{-1}}\ln(2\cosh(E_F/2k_BT)) \\ &+ \frac{e^2}{4\hbar}\left(H(\omega/2) - \frac{4i\omega}{\pi}\int_0^\infty d\Omega \frac{H(\Omega) - H(\omega/2)}{\omega^2 - 4\Omega^2}\right)\end{aligned} \tag{1.17}$$

where $H(\Omega)$ is defined as follows [17]:

$$H(\Omega) = \frac{\sinh(\hbar\Omega/k_BT)}{\cosh(\hbar\Omega/k_BT) + \cosh(E_F/k_BT)} \tag{1.18}$$

Figure 1.3 shows the conductivity of graphene ($\tau = 10^{-13}$ and $E_F = 0.77eV$) [12] at $T = 0K$ compared with the one obtained for the room temperature. As the temperature of the graphene layer increases, the frequency dependency of conductivity becomes more gradual. It is notable that the peak value of imaginary part of conductivity reduces by half for $T = 300K$.

Though the surface conductivity model is well-developed for graphene, the inclusion of this surface conductivity in the commercial softwares based on a volumetric model such

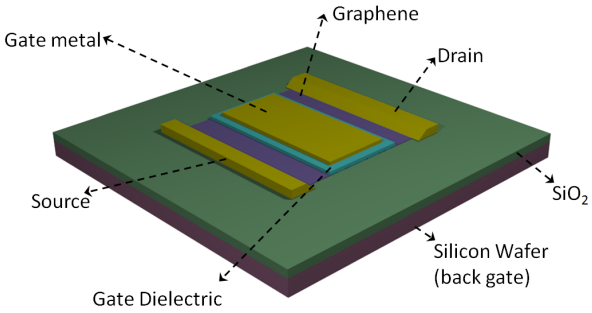

Figure 1.5: The typical structure of a graphene device. The silicon substrate acts as the backgate to control the Fermi energy level of graphene.

as the finite element method (FEM) and the finite difference time domain (FDTD) is not possible. For this reason, a volumetric model for the graphene layer is also proposed [18]. The equivalent volumetric permittivity of the graphene layer can be obtained from:

$$\epsilon_r = 1 + \sigma(\omega)/i\omega\Delta\epsilon_0 \tag{1.19}$$

where Δ is the effective thickness of the graphene layer [19]. In deriving the Eq. 1.19, it is assumed that the thickness of Δ is small enough that the current is uniformly distributed along the thickness. As presented in Chapter 4, the volumetric model introduced here is as accurate as the surface model for $\Delta < 1nm$. Figure 1.4 shows the obtained permittivity ($\Delta = 0.7nm$) for three different Fermi energy levels of the graphene layer, showing that the constitutive parameters of the graphene layer can be controlled by changing the Fermi energy level of graphene. One of the simplest method to change the Fermi level is via backgating of the silicon substrate (Figure 1.5). Considering the controllable conduction loss in graphene, one may think of realizing different type of graphene-based modulators such as the ones proposed in [19–22].

It is important to note that no external magnetic field has been assumed in the previous derivations. The existence of external magnetic field changes the band-diagram of the graphene and also the isotropy of the conductivity tensor. The derivation and the applications of the anisotropic conductivity tensor are detailed in [11, 23].

1.3 Interaction of electromagnetic field with graphene

The interaction of light with patterned graphene structures shows peculiar behaviors which are mainly the result of the two dimensional (2D) structure of graphene [18, 24, 25]. The

periodically patterned graphene structure can completely absorb the optical beam in a specific wavelength, which can be tuned by changing the Fermi energy level of graphene [26]. The patterned graphene structures also show interesting tunable properties in the terahertz (THz) and the infrared spectra, as measured in [27, 28]. In addition, the closely spaced graphene flakes show high field enhancements [13, 29] which can potentially be applied to biosensors, photonic metamaterials [18], and optical nanoantennas.

Most of these effects originate from either the excitation of surface plasmons in graphene, or from the plasmon coupling with metallic nanostructures. Each of these effects opens up new possibilities for graphene-based devices. In the following sections, we review the importance of the plasmon generation/coupling in graphene and how it contributes to the realization of featured components for new applications. This review is also an essential part of our introduction to the graphene-based THz photomixer in which the plasmonic effects are dominant. As the numerical analysis are an essential part of the device characterization, I also briefly review the current trends in numerical methods developed for the analysis of graphene-based components.

1.3.1 Plasmonic properties of graphene

Plasmon is a quantum of plasma oscillations [16]. The generation of this quasi-particle is the result of a coupling between the electromagnetic field with the electron wave. Its main property, from an application point of view, is that the plasmons are squeezing light photons far below their diffraction limit. This property makes them a promising candidate for a broad range of applications in optics such as optical waveguiding [30, 31], biosensing [32], imaging [16], and the realization of nanoantennas [33]. The most prominent materials supporting the plasmon resonances are gold and silver. The inherent plasmons of gold and silver, however, suffers from two deficiencies; their surface plasmon-polariton (SPP) resonances only occur at the visible range of spectrum and the loss of SPP resonances is huge because of the corresponding metal losses.

The negative permittivity of graphene (Figure 1.4) also allows the excitation of long-lived plasmon waves in the midinfrared (Mid-IR) and THz range of frequency [34, 35]. In contrast to the metal plasmons, the graphene's plasmons can be dynamically tuned using the electrostatic backgating [18, 24, 28, 36–39]. By increasing the Fermi level, it is possible to block the interband absoption and consequently increase the plasmon's life-time [20, 37]. Even optical pumping can be used to manipulate the plasmon resonances in graphene layer [40].

The existence of strong plasmons confined to the surface of graphene can be exploited in

the applications where a strong light-matter interaction is required, e. g. Mid-IR sensors [34, 41, 42]. Mid-IR range is well suited for biosensing since the biomolecule vibrations, which uniquely identify the constituents of life, couple to the electromagnetic spectrum in this range of frequency. DNAs, proteins, and lipids are a few examples of the constituents that can be detected using the vibrational spectroscopy. Besides the enhancement in sensing which arises from the plasmon resonances, the chemical bonding between biological materials and either the reduced graphene oxide (RGO), or chemically derived graphene (CDG) can be used for detection purposes [43, 44].

In addition to the sensing applications, the highly confined plasmons of graphene makes it suitable for subwavelength imaging and the realization of hyper lenses [45, 46]. A well designed graphene lens can differentiate between two points separated by $\lambda/10$ [45]. This is an exceptionally high resolution obtained using the near field imaging.

1.3.2 Enhanced wave-matter interaction using the surface plasmon modes of metallic structures

The controllable constitutive parameters of graphene make this material an excellent candidate for a wide range of applications [24, 28, 47]. However, the interaction of graphene with the electromagnetic (EM) field propagating perpendicularly to its surface is low due to its single layer nature. The absorption of the graphene layer in the visible range of frequency is about three percent which originates from the minimum conductivity of graphene in the visible spectrum. The small absorption of graphene is a huge obstacle in realization of structures in which a strong light-matter interaction is needed such as a THz photomixer. In a structure like THz photomixer, the efficiency of the device is directly proportional to the absorption, and the transmitted/reflected parts of the laser power are essentially contributing to the device losses. As we discussed earlier in this chapter, one approach to increase the light-matter interaction is to use graphene plasmons. The graphene plasmons, however, are only dominant and effective in the mid-infrared/THz range of frequency and cannot be extended to the near-infrared range. One effective way to enhance the graphene-wave interaction in the visible spectrum is to use the graphene in a waveguiding structure. In this approach the interaction is enhanced since the traveling wave in the waveguide interacts with the graphene over a finite length [19, 22, 48]. This specific approach leads to the fabrication of waveguiding-based structures that requires design and fabrication of an optical waveguide.

A different while effective approach is to integrate the graphene layer with a plasmonic nanostructure. Plasmonic structures are known to be able to confine light far below the

diffraction limit [16]. Considering the fact that the actual probability of the excitation of an atom can be written as $\sigma/\mathcal{A}$ where σ is the cross section of the atom and $\mathcal{A}$ is the distribution area of the EM field [49], the photon confinement by a plasmonic structure leads to higher light-matter interaction (An interesting application of plasmon structures for single molecule detection can be found in [49, 50]). This intensified interaction is the direct result of an increase in the electric field amplitude [51]. The more confined energy distribution of photons near the graphene layer, the higher the probability of electron-photon interaction.

The plasmon resonaces of nanoparticles integrated with graphene is used for enhancement of photovoltaic effect in graphene [52,53] and enhancement of Raman scattering from graphene [54, 55]. As described in Chapter 5, a nonlinear process such as the difference frequency generation can be enhanced by 4 orders of magnitude in the presence of these nanoplasmonic structures. This unprecedented level of enhancement greatly improves the generated power of THz wave.

1.3.3 Numerical analysis methods

Being just one atomic layer thick, graphene can be modeled as a surface conductivity in the Maxwell's equations. The value of this surface conductivity, obtained using a quantum mechanical approach, is reported in [13, 17, 34]. To study the electromagnetic wave scattering from graphene, two different approaches have been proposed. The first approach considers graphene as a very thin layer [18]. The second approach models the graphene layer as a surface current which causes a discontinuity in the tangential magnetic field [56].

In the first approach, the graphene layer is assumed to have an equivalent thickness of Δ and a volumetric permittivity of $\epsilon_g = 1 + \sigma_s/(j\omega\Delta\epsilon_0)$, where σ_s is the surface conductivity of graphene. This volumetric model can be used used in numerical methods such as the FEM [18] and the finite difference time domain (FDTD) method [57–59]. In addition to the fine meshing required to model the thin graphene layer, another drawback of the volumetric permittivity model is the fact that there is no unique value for Δ. The ambiguity in the value of Δ necessitates verifying the numerical convergence of electromagnetic fields through decreasing the value of Δ. The main difficulty with this test is that since the graphene is actually thinner than the wavelength or finest mesh size, the change in the effective thickness, which modifies the field inside that fictitious effective layer (the graphene model), should not have any effect on the field around the graphene.

Implementation of a numerical method based on the second approach, which uses a surface boundary condition (SBC), on the other hand, requires a modified formulation of

the numerical method. In the case of the FDTD method, a SBC-based algorithm has already been developed [60]. The reported FDTD method reduces the computational cost of numerical simulations; however, the conductivity of graphene must be written as a summation of Drude-like expressions, thereby limiting its applicability to the cases where the interband transitions are not important [61].

To resolve the aforementioned issues, in Chapter 4, I am proposing a general and numerically efficient multipole-based technique combined with a SBC for the analysis of electromagnetic scattering from graphene flakes. The proposed approach also allows us to assess the accuracy of the conventional volumetric FEM.

1.4 Nonlinearity of graphene for THz wave generation

The thriving research field of THz technology has become increasingly attractive for a fast growing number of applications including food quality control, security monitoring, medical science, nondestructive imaging, and communication [62]. One of the most important challenges in implementing the aforementioned applications is the realization of an efficient THz source. While the DFG process is considered as a promising approach for a number of applications, the efficiency of the devices built using this approach is not sufficient. To increase the efficiency of the DFG process, the nonlinearity of the material used in the THz source is a key factor. Different materials such $GaAs$, $ZnSe$, and etc. are studied and tested; however, the search for a materials with a higher nonlinearity still continues.

The monolayer of graphene provides an enhanced nonlinearity compared with some of the studied material, e. g. $GaAs$ [63, 64], and is a new candidate for the realization of an efficient THz source. The nonlinearity of graphene for perpendicularly incident waves is studied using different approaches such as quasi-classical Boltzmann equation [65–67] and optical Bloch equation [68]. The reported nonlinearities, however, are limited to the third order processes because of the centro-symmetric structure of graphene. Considering the fact that the third order processes are significantly weaker than the second order processes [51, 69], it is desirable to break the symmetry of induced nonlinear dipoles in the graphene. The symmetry can be broken by applying a DC current [70, 71]. Using this approach the second order nonlinearity of graphene comes into the picture [70], and a stronger nonlinearity and consequently a more efficient frequency conversion can be obtained.

Recently, the generation of THz signals are reported for unbiased graphene layers when the optical beams are obliquely incident [72, 73]. The momentum of incident photons

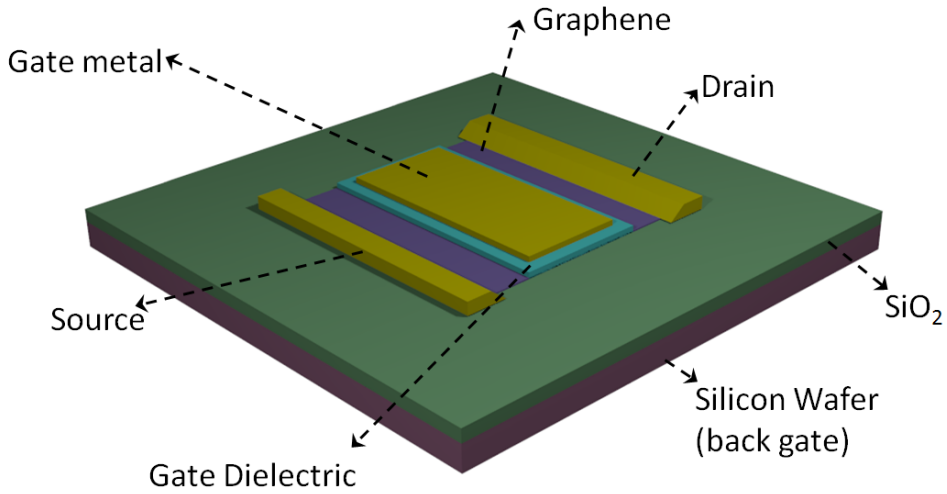

Figure 1.6: The typical structure of a graphene device. The silicon substrate acts as the backgate to control the Fermi energy level of graphene. Drain and source metal contacts define the current of the graphene sheet and gate controls the flow of current.

is responsible for the induction of a second order nonlinear current referred to as "drag current" which contributes to the DFG [74, 75]. Using this approach the symmetry of transitions can be broken and an enhanced DFG can be observed. This approach can also provide a tunable and an effective way of generating THz plasmon on the surface of graphene [28].

1.5 Graphene production and device fabrication

Figure 1.6 displays a typical structure of a graphene-based device. The silicon substrate acts as the back-gate to control the Fermi energy level of graphene. Drain and source metal contacts define the current of the graphene sheet and gate controls the flow of current. The fabrication of graphene, depositing metal contacts, and the fabrication of gate dielectric are three important steps in building the device. In this section, the different fabrication methods are addressed and their effects on the device performance will be described.

1.5.1 Graphene production

Different methods that can be used to produce the single layer (SLG) and multilayer graphene(MLG) are as follows:

- Micromechanical Cleavage
- Liquid-phase exfoliation
- Graphene oxide
- CVD
- Carbon segregation
- Chemical Synthesis

A summary of each method can be found in [25]. Among the mentioned methods, micromechanical cleavage and CVD processes are more often used to obtain the graphene. Here we explain these two methods.

The micromechanical cleavage method, which was first used to demonstrate the existence of SLG [76], is based on peeling off graphite by means of adhesive tapes. Obtained SLGs are less than millimeters in size but the quality of obtained graphene is considerably high. The micromechanical cleavage is the method of choice for research. Fig. 1.7 shows the obtained graphene flakes using adhesive tapes. Adhesive tape is used to peel off the highly pure natural graphite.

The following are steps to fabricate large area graphene layers in a CVD process [77,78]:

- load the fused silica tube with the $25-\mu m$ thick Cu foils.
- evacuate, back fill with hydrogen, and heat to $1000°C$.
- maintain a H_2 pressure of 40 mTor.
- stabilize the Cu film at the desired temperatures, up to $1000°C$.
- introduce $35sccm$ of CH_4 for a desired period of time at a total pressure of $500mTorr$.
- Cooling down the furnace to room temperature.

Fig. 1.8 summarizes different steps of CVD process. The obtained CVD graphene can be transferred to another substrate by coating the graphene layer with PMMA and then dissolving the Cu foils. A more detailed description can be found in [77].

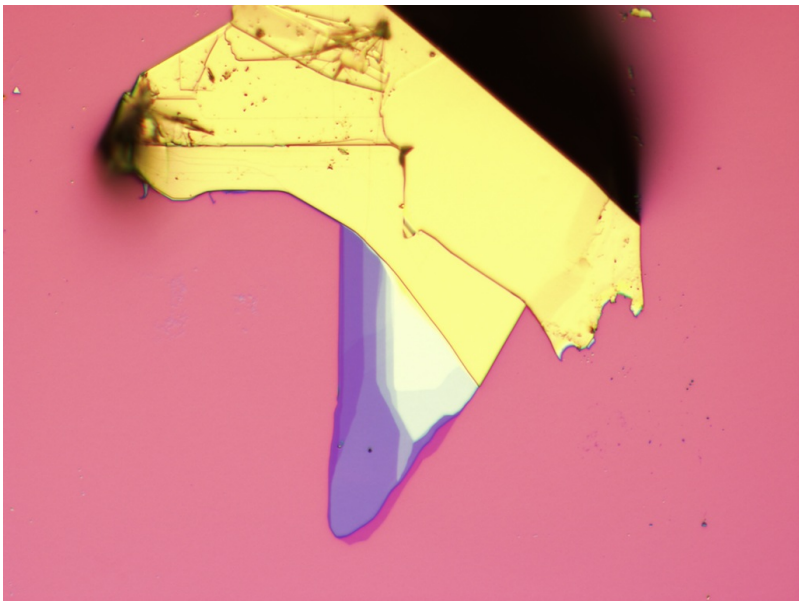

Figure 1.7: The obtained graphite flake using micromechanical cleavage of highly pure graphite. As the number of layers decreases the substrate color can be seen more vividly.

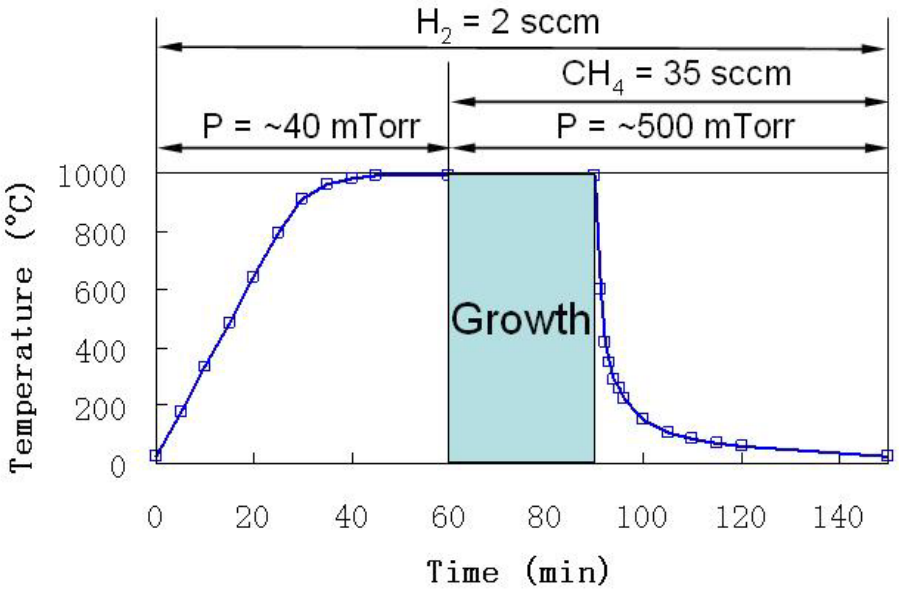

Figure 1.8: Different steps of a CVD process to obtain the SLG [77].

1.5.2 Fabrication of gate dielectric and the drain/source metallic contacts

Since SLGs can be easily doped when exposed to other material, the fabrication of gated graphene structures is a crucial step. Moreover, the quality of gate deposition affects the electronic properties of graphene and it may deteriorate its special properties. For example, evaporated $SiO2$ degrade graphene performance by 85%. Among the different methods, atomic layer deposition is the most successful one [79]. The procedure can be summarized as follows:

- Deposit 2nm Al on top of graphene using electron beam evaporator.
- Exposing the layer to air to form the oxidization of Al layer on top of graphene.
- Using the ALD chamber to deposit Al_2O_3 as gate dielectric.

Using this method, the neutral point (Dirac point) of graphene layer is around $V_D = 0.08V$ which shows very small loading effect. The measured mobility is also $\mu = 8600\frac{cm^2}{V}$ [79]. It is worth pointing out that single layer boron nitride (BN) also can be used to make the gate dielectric (because of 6eV band-gap of BN and having the same structure of graphene layer the loading effects are small) [80].

Another crucial point that should also be addressed is the maximum achievable value of Fermi energy level using the gate dielectric. It is important to notice that the gate voltage cannot be increased arbitrary because of the break down voltage of gate dielectric. For example, for the regular backgate dielectrics such as SiO_2, the value of Fermi energy level can be swept only by $300meV$. However, using very specific dielectric materials such as ion-gel [81] and solid polymer electrolyte [82] and under special treatments such as cooling, it is possible to achieve the Fermi energy levels as high as $1 - 2eV$.

The metallic contacts are necessary either for changing the Fermi energy level of graphene or for controlling the flow of current in graphene. Since this metallic contacts are in direct contact with graphene, it is important to know how they affect the Fermi energy level of graphene and the carrier types. Table 1.1 summarizes the main important properties of Ni, Cr/Au, as Ti/Au contacts (Table reproduced from the obtained results of Ref. [83]).

1.6 Research objectives

The research objectives of this work can be summarized as follows:

Table 1.1: The difference in work-function of Ni, Cr/Au, as Ti/Au contacts as compared to that of graphene ($\Delta\phi$) and their carrier type.

Metal	Ti	Cr	Ni
$\Delta\phi$	-0.2	0.1	0.7
Carrier Type	hole	$-$	hole

- Developing an analysis method for the study of photomixing process in graphene. Moreover, proposing an enhancement mechanism to increase the device efficiency and throughput. Also, study of the enhanced mixing process in the presence of a designed antenna, and evaluating the achievable THz power.
- Proposing a recipe for fabrication of the proposed photomixer. Considering the complex structure of THz mixer, the fabrication recipe should ascertain a repeatable and reliable process.
- Characterizing the fabricated photomixer by measuring the amount of induced photocurrent and the power of radiated THz wave.

Chapter 2

Enhancing the light-matter interaction in graphene using a periodic nanoplasmonics structure

[1] As discussed in Chapter 1, the interaction of mid-infrared electromagnetic wave by graphene can be enhanced with a plasmonic structure. The plasmonic structure, which is composed of a periodic arrangement of metal nano-golds, localizes the photon distribution function, thereby enhancing the wave-matter coupling.

In this chapter, the design procedure for achieving an optimum enhancement is presented and a fabrication recipe specifically developed for the realization of a nano-crescent periodic structure is demonstrated. To experimentally characterize the enhancement, we record the intensity of photons generated in a nonlinear process such as the one in the Raman Spectroscopy. The Raman output of a graphene layer, located on top of the proposed nanostructure, supports the idea that metallic plasmons enhances the wave-graphene interaction by several orders of magnitude. The Raman measurements are done for the wavelength of $\lambda = 532nm$. We also designed and fabricated other structures for the wavelength of $\lambda = 800nm$ which is the wavelength of available laser source for THz photomixing.

[1] The structure used in this chapter was proposed by Dr. Mohammadreza Khorasaninejad and Prof. S. Saini for use in surface plasmonic sensing applications. In this chapter, the structure is optimized for enhanced Raman scattering from a graphene layer suspended on top of the structure.

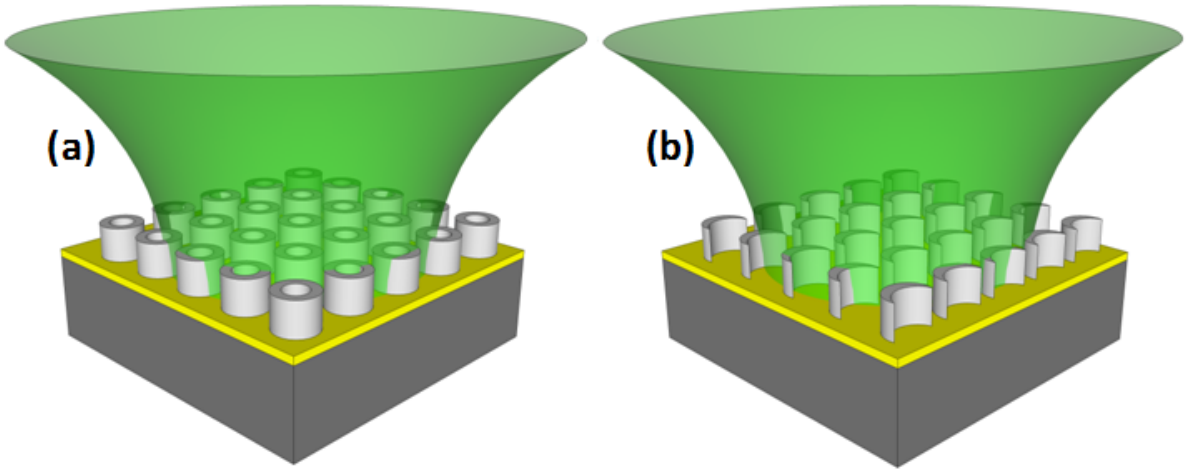

Figure 2.1: Schematic of ring (a) and crescent (b) nanoparticles on a gold-coated glass substrate. The thickness of gold is 30 nm and the height of silver nanoparticles is 75 nm.

2.1 Proposed plasmon nanostructure

Gold nanoparticles are known for their plasmon resonances in the near-infrared range of frequency including the wavelength of $\lambda = 800nm$. Our characterization method (Raman Spectroscopy at $\lambda = 532nm$), however, would require enhanced wave-graphene interaction at $\lambda = 532nm$ where the plasmon resonances of silver nanoparticles are more prominent. Consequently, we are using silver nanoparticles in our designs for Raman measurements.

The shape and the periodicity of nanoparticles determines the resonance wavelength and the achievable enhancement, e. g. nanoparticles with sharp edges have the most confined field. Considering the fabrication tolerances and the type of process (lift-off), the realization of nanoparticles with sharp edges is challenging. So, we focus our study to simple structures that can be easily fabricated such as cubes, cylinders, rings, and crescents.

To represent the periodic structure in our simulations, we consider a unit cell of the periodic structure with appropriate periodic boundary conditions. The dielectric constant of silver as reported in [84] has been used in our FEM simulations. The incident wave is a plane wave propagating perpendicular to the surface of graphene. To compare the en-

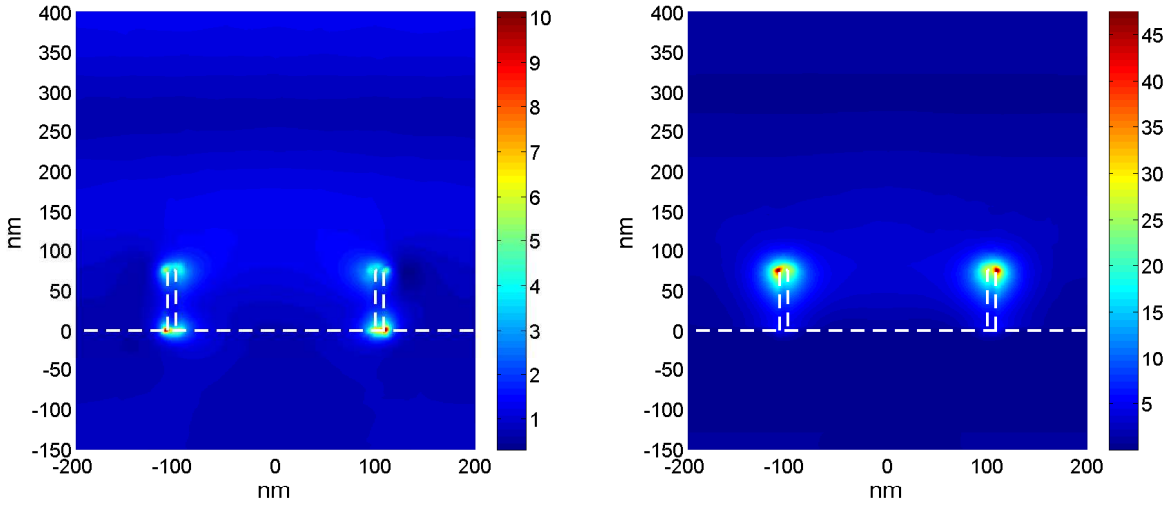

(a) (b)

Figure 2.2: The amplitude of electric field on the cross section of a crescent nanoparticle with (a) and without (b) the gold reflecting mirror.

hancements obtained for different nanoparticles, we use the parameter g defined as follows:

$$g = \frac{\int_S \left|\vec{E}\right|^2 dS}{\int_S \left|\vec{E_0}\right|^2 dS} \tag{2.1}$$

where $\vec{E}$ is the electric the field on the graphene layer, $\vec{E_0}$ is the incident wave's electric field, and S is the surface of the graphene layer (The surface S is a rectangle with the same dimensions of the unit cell at the distance of $10nm$ from the top of nanoparticles). The proposed enhancement factor g represents the enhancement in the energy of total field over the graphene layer.

Different periodic structures made of cubes, cylinders, rings, and crescents are investigated using the proposed criterion of Eq. 2.1. The best results are obtained for the case of nano-rings and nano-crescents.

Figure 2.1 shows the periodic array of nanocylinders or nanocrescents studied for the field enhancement. Figure 2.2a shows the cross section of electric field distribution for crescent nanoparticles over a glass substrate. There are two hot spots at the top, where

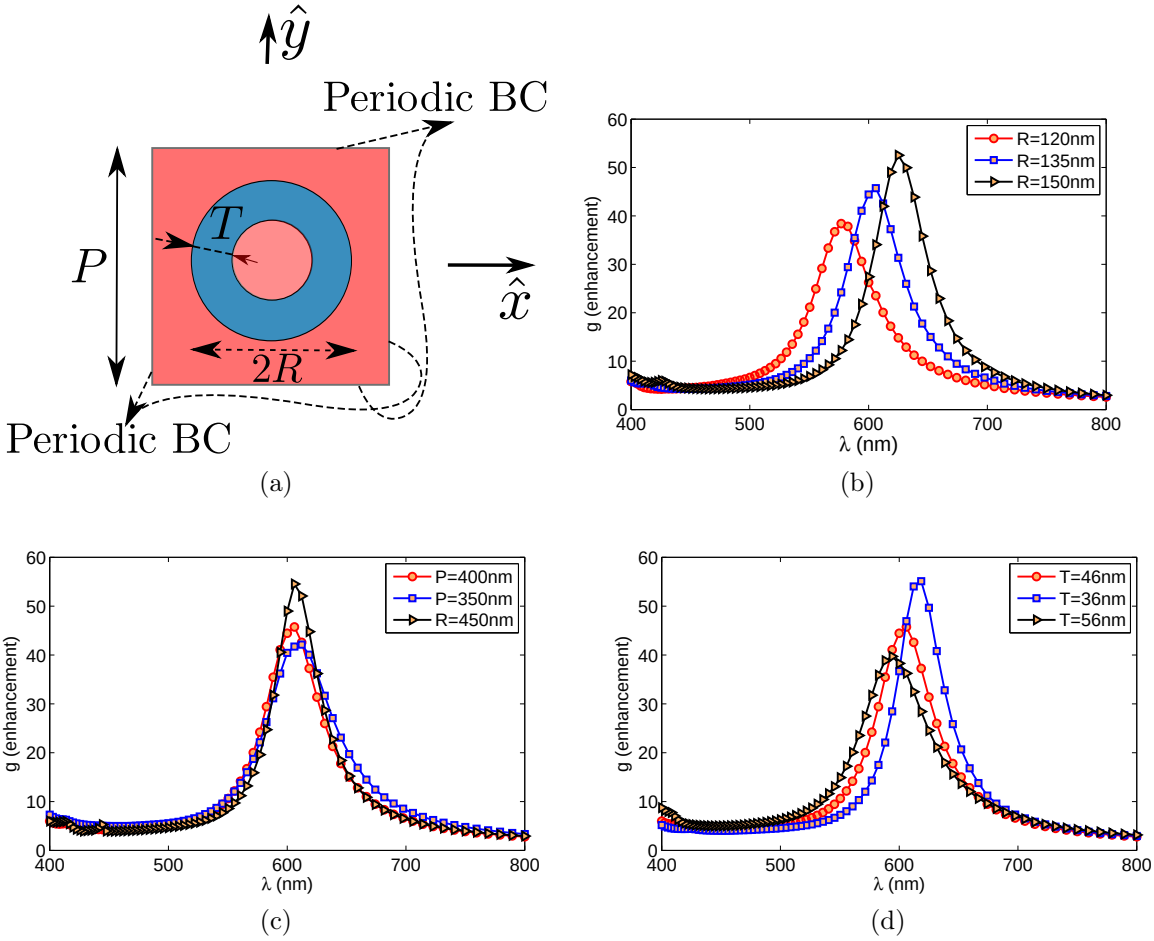

Figure 2.3: The schematic of a unit cell of ring nanoparticles (a). The effect of radius of nanorings (b), period of structure (c), and the thickness of nanorings (d) on the defined surface enhancement.

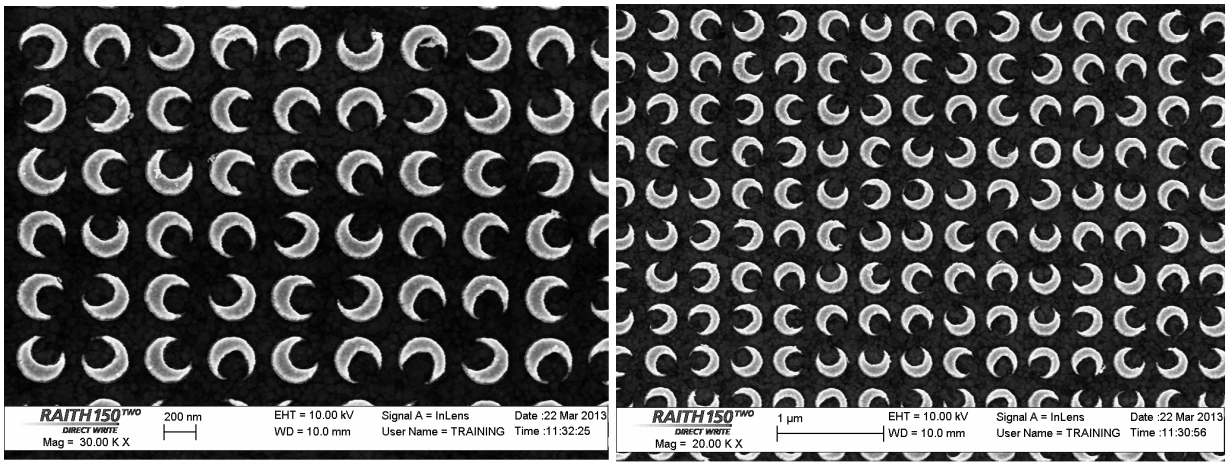

(a) (b)

Figure 2.4: The SEM image of fabricated gold nanocrescents for the scale bar of $200nm$ (a) and the scale bar of $1\mu m$ (b) [55].

graphene is located, and at the bottom of the structure. To gain more enhancement from the nanostructure, a gold reflector is deposited below the structure which helps enhancing the field's amplitude in upper hot spots by reflecting the field at the nanoparticles-glass interface (Fig. 2.2b). The required thickness of gold substrate is $30nm$.

The dimensions of the nanoparticles can be adjusted to acquire the maximum enhancement in the desired wavelength. Figure 2.3 displays the effect of the periodicity, the thickness, and the radius of nanorings in the resonance frequency of surface plasmon. Radius of nanorings greatly changes the SPP resonance wavelength, while the period only changes the amplitude of enhancement (Higher values of P leads to higher Q-factors). Increasing the thickness mainly increases the absorption and reduces the peak value of enhancement.

2.2 Fabrication and measurement

[2] The substrate has been cleaned in an ultrasonic bath of acetone and propanol for 30 minutes. A thick layer of Al followed by $5nm$ of titanium followed by $30nm$ of gold was then deposited on the glass substrate using electron beam deposition. The sample was spun

[2]The fabrications reported in this chapter have been done by Dr. Reza Khorasani from prof. Simarjeet Saini's group.

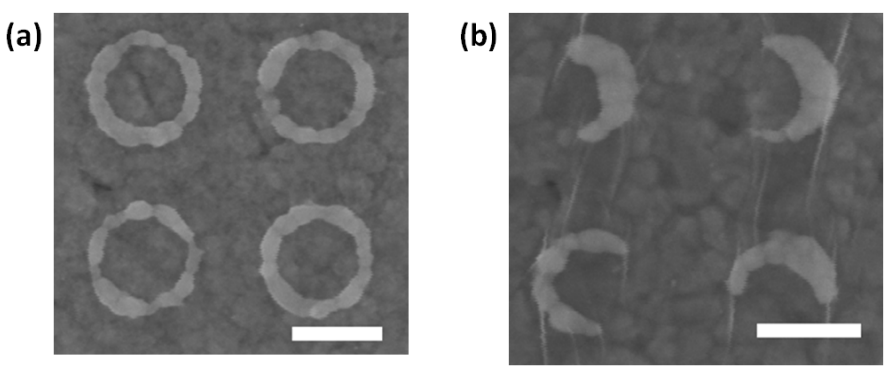

Figure 2.5: The shape of nanostructures after transferring the graphene layer [55].

coated with PMMA $A4$ at the speed of 3000 rpm resulting in a $190nm$ thick layer of PMMA. After baking the sample for 20 minutes at the temperature of 180^oC, the electron beam lithography was carried out using a Raith TWO-150 at 25 KV. The pattern was developed in MIBK:IPA $1:3$ bath for 40s followed by 30s rinsing with IPA. After developing the EBL patterns, a $75nm$ thick layer of silver was deposited. The sample was soaked in the PG remover over night to accomplish the lift-off process. To fabricate the nanocrescents, the idea of over exposing the resist with electron beam is proposed by Dr. Reza Khorasani. Figure 2.4a show the effectiveness of the over exposure for fabrication of gold nanorings and nanocrescents, respectively. The period of structure is $P = 400nm$ and the thickness of nanorings is $T = 45nm$. Figure 2.4b shows a larger number of nanocrescents in a view.

A $1cm \times 1cm$ PMMA-coated graphene from ACS Material was used in this experiment. The graphene sheet was transferred to our substrate with the fabricated nanoparticles. After transferring the graphene, there are water droplets trapped below it. Removing these water droplets are necessary since they do not let the graphene layer to be attached to the surface of nanostructure. We used nitrogen gas and heating to dehydrate the sample. The PMMA layer can then be dissolved in acetone. The existence of wrinkles in the transferred graphene layer is obvious in the SEM pictures (Fig. 2.5).

The Raman spectrum of graphene has two major peaks, the $G-$peak at $1580cm^{-1}$and the $2D-$peak at $2700cm^{-1}$ [85]. For a single layer graphene, the amplitude of the $G-$peak is smaller than the $2D-$peak and the $2D-$peak is a single sharp one. As the number of layers increases, other peaks contribute to the $2D-$peak broadened by the coupling between layers. The amplitude of the $G-$peak in comparison to the $2D-$peak and also the shape of the $2D-$peak can be used to differentiate between the single layer graphene and a few layer graphene. Figure 2.6 shows the measured Raman spectrum of graphene layer on

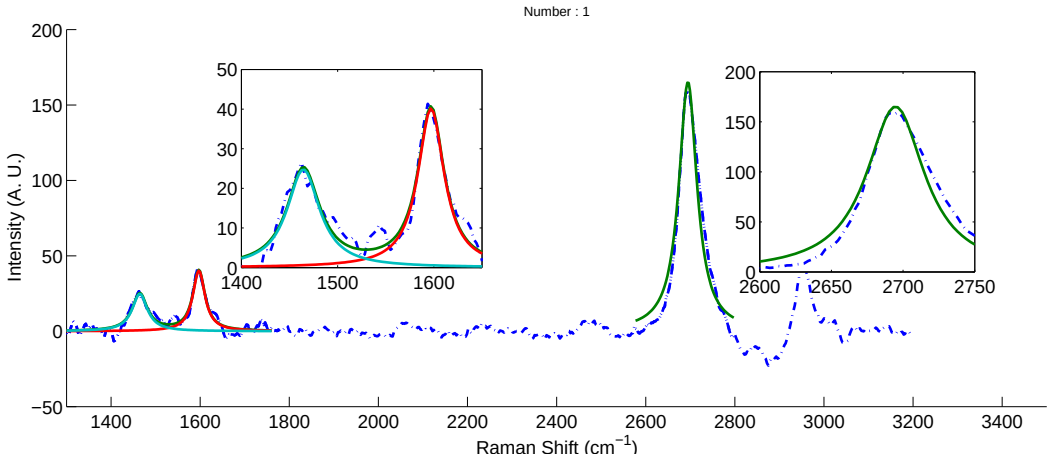

Figure 2.6: Raman Spectrum of graphene over the SiO_2 wafer. The dashed line is the measured Raman spectrum and the continuous lines show the fitted Lorentzian curves. The insets show the fitted Lorentzian curves to the actual peaks [55].

top of a silicon dioxide wafer. As can be seen, the measured Raman spectrum has all the aforementioned features of a single layer graphene. The insets show the fitted Lorentzian curves to the actual peaks.

Figure 2.5 shows the SEM image of nanoparticles after transferring the graphene layer. After transferring graphene layer, the shape of nanoparticles has been deformed. The maximum achieved enhancement for the ring structure is when $R = 135nm$ and $T = 46nm$ and for the crescent one is when $R = 110nm$ and $T = 46nm$ (Fig. 2.7). The graphene folding around the crescent structures can be observed in SEM image. The Raman spectrum for graphene on top of the plasmonic structure can be seen in Fig. 2.8. Table 2.1 summarizes the position and the amplitude of measured peaks for the graphene layer. To obtain the enhanced factors reported in Table 2.1, Lorenzian curves are fitted to the measured Raman spectrum of graphene over crescent or ring structures and then the peak amplitudes are compared with those of graphene over silicon. Using this method, the Raman shifts can be reported more accurately. The total obtained enhancement for the ring structure is lower than that of the crescent structure. For the crescent structure a much higher enhancement obtained for the $G-$peak comparing with the $2D-$peak. However, for the case of ring structures a higher enhancement was obtained for the $2D-$peak. Besides, there is a blue shift in the Raman peaks for both ring and crescent structures.

As previously outlined, there are two different enhancements obtained for nanocrescents. The large difference between the obtained results is addressed by investigating the

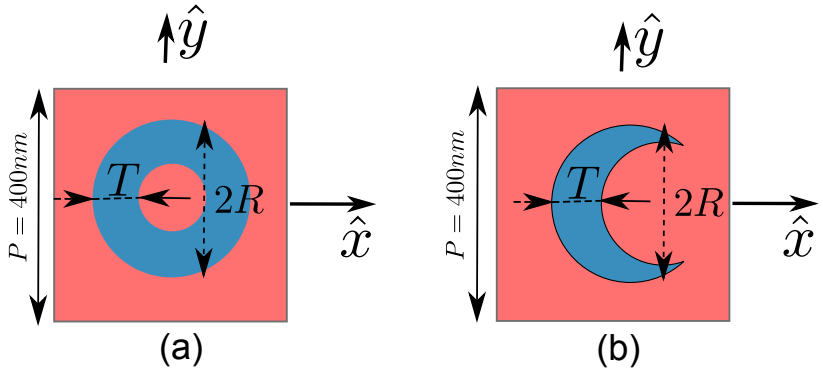

Figure 2.7: The schematic of nanorings (a) and nanocrescents (b) with the associated dimensions.

Table 2.1: Summary of enhancement and position of G- and 2D-peaks for different structures [55].

Peak	Structure	Enhancement	Centre Wavelength (cm^{-1})
G-Peak	SiO_2	1	1597.1
	Ring	148	1595.4
	Crescent 1	904	1594
	Crescent 2	161	1596.4
2D-Peak	SiO_2	1	2694.7
	Ring	73	2693.8
	Crescent 1	38	2682.6
	Crescent 2	31	2688.6

actual distance of the graphene layer from the nanoparticles at these two spots. The AFM images of the two spots are shown in Fig. 2.9. Fig. 2.9a shows a place where the graphene is attached to the crescents ("Crescent 1" spot) and individual element profiles within the periodic structure can be observed. Using the AFM results, the average spacing between graphene and the silver nanoparticles is $5nm$. Figure 2.9b shows the place where the graphene is not attached to the surface of nanoparticles ("Crescent 2" spot) and is sitting like a tent on top of the nanostructure. Individual crescent's surface features are not visible in the AFM measurement. Nevertheless, the distance between the graphene and the silver

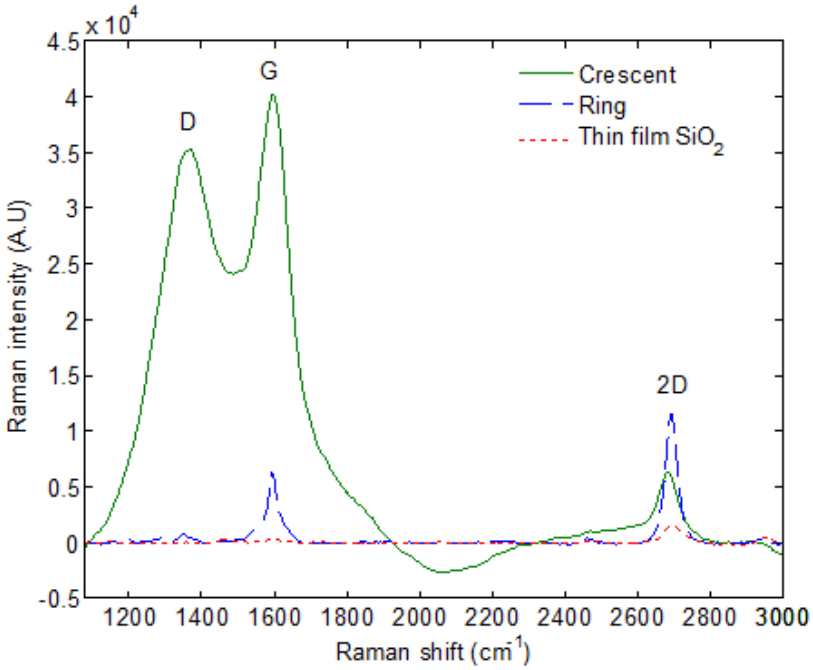

Figure 2.8: Raman spectra of graphene on a thin film of silicon dioxide (red dashed line), rings (blue dashed line), and crescents (continuous line) [55].

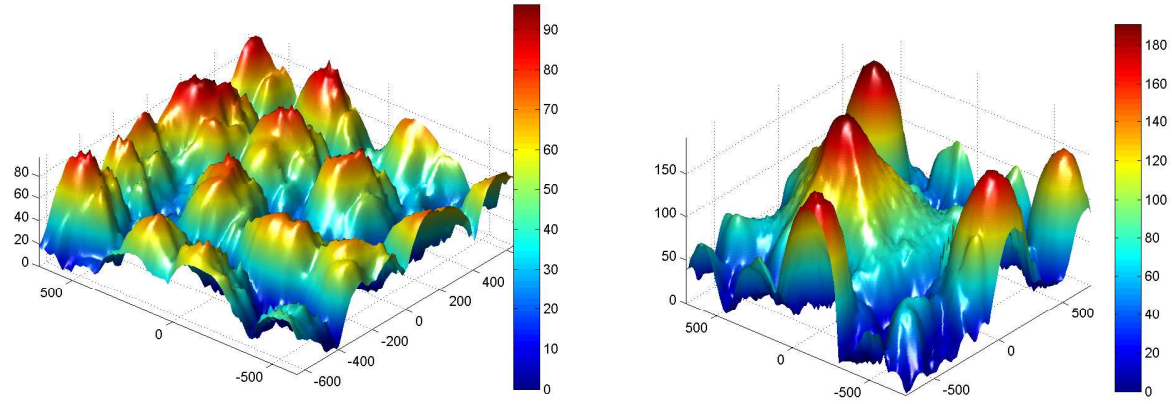

(a) (b)

Figure 2.9: The AFM image of graphene over the nanocrescents at two different locations. The distance of graphene from the nanocrescents at location (a) is smaller than that of location (b) [55].

nanostructure is obviously larger than the previous spot. The difference in the recorded average distance is the main cause of observing different enhancements.

To analytically verify our obtained results, we are using a previously developed method [86] based on the power distribution of the incident and Raman scattered fields. The Raman enhancement can be predicted using the factor g_R defined as follows:

$$g_R = \frac{\int_S |E_{\lambda 0}|^2 \, |E_{\lambda_s}|^2 \, dS}{\int_S |E^{inc}_{\lambda 0}|^2 \, \left|E^{s0}_{\lambda_s}\right|^2 \, dS} \tag{2.2}$$

where $|E_{\lambda 0}|$ is the amplitude of the electric field at $\lambda = 532nm$ and λ_s is the wavelength of scattered wave (the value of λ_s for the $G-$peak is $\lambda_G = 582nm$ and for the $2D-$peak is $\lambda_{2D} = 622nm$). The field amplitudes $|E^{inc}|$ and $|E^{s0}|$ are the incident and the scattered fields in the case that there is no plasmonic structure. The surface S is the surface of graphene layer located on top of the nanostructure. It is important to note that the gain g_R is a function of the graphene's distance from the nanoparticles. Figure 2.10 shows the field distribution for the incident and the shifted Raman wavelengths. The field distribution over the crescent nanostructure is mostly confined around the sharp edges for all wavelengths. However, the electric field distributions of nano-rings for $\lambda = 532nm$ and $\lambda = 622nm$ are concentrated around the inner and outer cylinders, respectively. Since the spatial

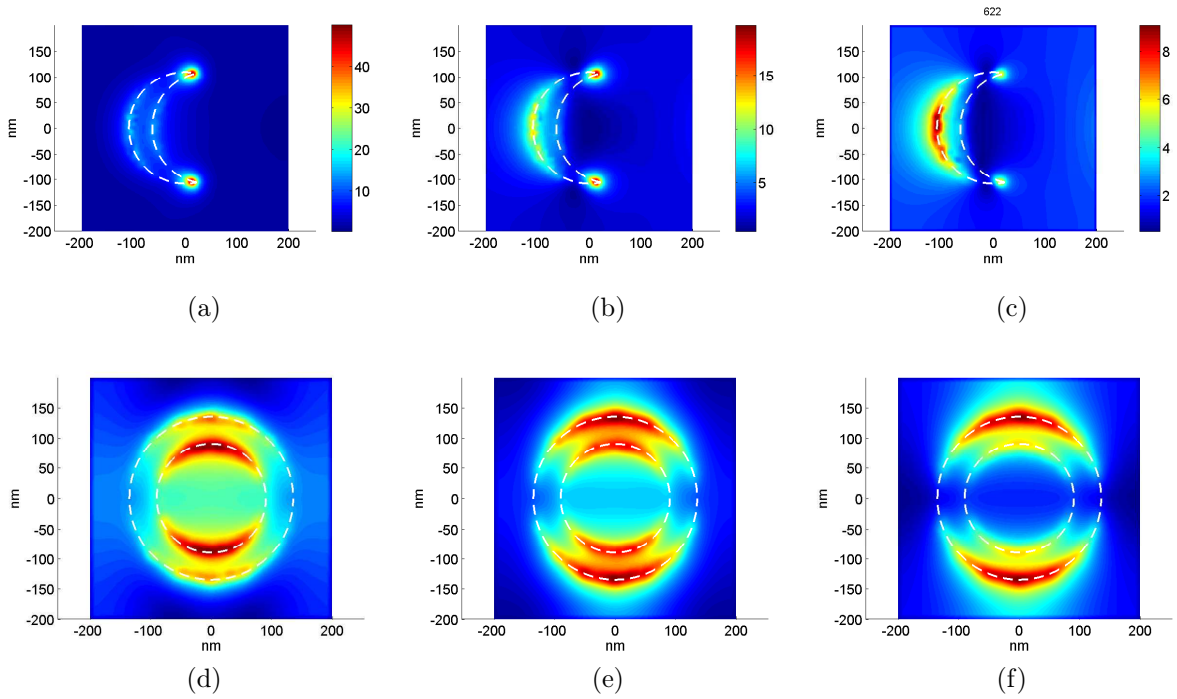

Figure 2.10: Electric filed distribution for a crescent ($R = 110nm$ and $T = 46nm$) at the wavelengths of 532 nm, 582 nm and 622 nm (a)-(c); and the ring ($R = 135nm$ and $T = 46nm$) at the wavelengths of 532 nm, 582 nm and 622 nm [55].

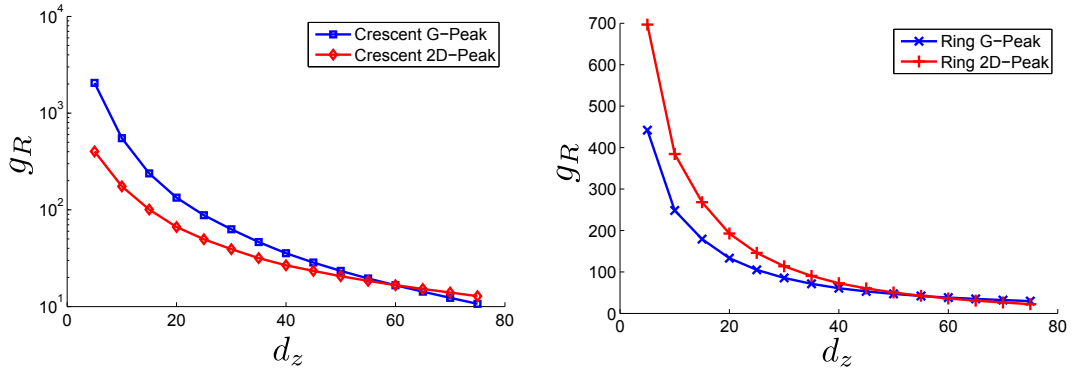

(a) (b)

Figure 2.11: The predicted Raman enhancement for $G-$peak and $2D-$peak of a graphene layer located at the distance d_z from nanocrescents (a) and nanorings (b) [55].

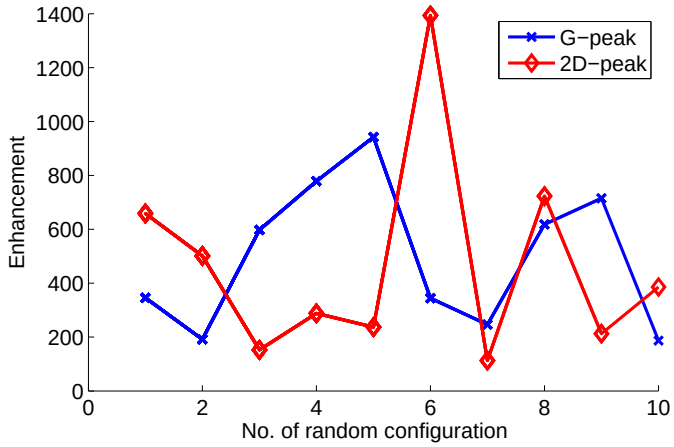

Figure 2.12: The obtained enhancement for ten random configuration of nanocrescents in a unit cell of 2×2 nanocrescents.

distribution of electric field for the nanocrescents remains the same for all wavelengths as opposed to the one for the nanorings, it is expected that the overlap integral of Eq. 2.2 for the crescent structure to be larger than that for the ring structure.

Figure 2.11 shows the predicted Raman enhancement for the $G-$peak and the $2D-$peak of the graphene layer on top of the nanostructure. The predicted enhancement because of the crescent structure for the $2D-$peak is smaller than the predicted enhancement for the $G-$peak. The measurement results (Table 2.1) also verify that the obtained enhancement for the first peak ($G-$peak) is lower than the obtained enhancement for the second peak ($2D-$peak). However, the predicted amplitude of enhancement does not match the measured results. The disagreement between the theory and the measurement is because of the random orientation of nanocrescents. Random directions of the nanocrescents contributes to the smaller enhancement measured with the Raman spectroscopy. To model the random directions of nanocrescents, a larger unit cell, including four randomly oriented crescents, is analyzed with the FEM. The simulations are carried out for ten different random direction of crescents. Figure 2.12 shows the obtained enhancement for all ten cases. The average value of enhancement is much lower than the predicted results of Fig. 2.11. Considering the random direction of nanocrescents, a better agreement between the theoretical enhancement and the measurement can be obtained.

Chapter 3

Quantum enhanced second order nonlinearity in graphene: the role of wave momentum and DC biasing

The purpose of this chapter is to study the effects of both the DC current and the photon-drag on the DFG enhancement in graphene. While the DFG is known to be a nonlinear process, there are fundamental differences between the DFG and the harmonic generation reported in the literature [51]. A complete description of the DFG process requires the inclusion of both inter- and intra-band transitions and considering the effect of wave momentum. Our results show that there is an optimum value of the Fermi-energy level where the second order nonlinearity can be enhanced by one order of magnitude, leading to an approximately two orders of magnitude enhancement in the power of the generated THz signal. Using this strong nonlinearity, one can envision the integration of a graphene-based THz source with other graphene-based THz components such as THz modulators [19], THz detectors [73, 87, 88], and plasmonic enhanced THz sensors [13, 28].

3.1 Difference frequency generation in graphene

In the low energy limit, the dynamics of electrons in a free standing graphene layer can be described using the following 2-dimensional Dirac equation ($\xi = 1$ for the Dirac cone K

and $\xi = -1$ for the Dirac cone K') [10]:

$$H_0\psi(\mathbf{r}) = \mathcal{E}\psi(\mathbf{r})$$
$$H_0 = \nu_F(\hat{p}_x\sigma_x + \xi\hat{p}_x\sigma_y) \tag{3.1}$$

where H_0 is the Hamiltonian of free standing graphene layer, ν_F is the Fermi velocity in graphene, and $\boldsymbol{\sigma}$'s are the Pauli matrices. The eigenfunctions of Eq. 3.1, in the momentum space, are as follows:

$$|l, \mathbf{k}\rangle = \frac{1}{\sqrt{2}}\begin{pmatrix} e^{-i\xi\theta_k/2} \\ (-1)^l e^{i\xi\theta_k/2} \end{pmatrix} \tag{3.2}$$

where $\mathbf{k}$ is the electron wave vector, θ_k is the angle of the wave vector k from the x-axis, and l shows the corresponding wave function in the conduction ($l = 0$) or the valance ($l = 1$) band. When an electromagnetic wave is incident on the graphene layer, the momentum defined in (3.1) should be replaced by the generalized momentum $\hat{\mathbf{\Pi}} = \hat{\mathbf{p}} + e\mathbf{A}$, where $\mathbf{p} = \hbar\mathbf{k}$ is the momentum of electrons. Using the aforementioned generalized momentum, the total Hamiltonian in reciprocal space can be written as [68]:

$$\hat{H} = \hat{H}_0(\mathbf{k}) + \hat{H}_{int}(\mathbf{k}) \tag{3.3}$$

where $\hat{H}_{int}(\mathbf{k})$ represents the interaction of electromagnetic wave with graphene. For an incident plane wave with the frequency of ω, the $\hat{H}_{int}(\mathbf{k})$ can be written as follows:

$$\hat{H}_{int}(\mathbf{k}) = e\nu_F\left(\sigma_x A_x + \xi\sigma_y A_y\right) \tag{3.4}$$

where $\mathbf{A}$ is the magnetic vector potential. Eq. 3.4 can be written in a more concise form as:

$$\hat{H}_{int}(\mathbf{k}) = \frac{1}{\omega}\boldsymbol{\mu}.\mathbf{E} \tag{3.5}$$

where $\mathbf{E} = i\omega\mathbf{A}$ is the electric field (see Appendix I) and

$$\boldsymbol{\mu} = \frac{e\nu_F}{i2}\left(\sigma_x\hat{x} + \xi\sigma_y\hat{y}\right) \tag{3.6}$$

is the polarization vector. In our derivations [89], we assume that one of the incident waves is a plane wave propagating perpendicular to the graphene's surface while the second plane wave is obliquely incident. The magnetic vector potential of the incident wave can be written as:

$$\mathbf{A} = \frac{\mathbf{E}(-\omega_q)}{-i2\omega_q}e^{-i(\mathbf{k}_q.\mathbf{r}-\omega_q t)} + \frac{\mathbf{E}(\omega_p)}{i2\omega_p}e^{i(k_p z-\omega_p t)} + c.c. \tag{3.7}$$

where $k_q = \omega_q/c$ and $k_p = \omega_p/c$ defines the wave vectors of incident waves; $\mathbf{E}(-\omega_q)$ and $\mathbf{E}(\omega_p)$ are the amplitude of electric field for the waves with the frequency ω_q and ω_p, respectively (since the electric field is real, we have $\mathbf{E}^*(\omega_q) = \mathbf{E}(-\omega_q)$ and $\mathbf{E}(\omega_p) = \mathbf{E}^*(-\omega_p)$). The plane wave with frequency of ω_p is propagating perpendicular to the surface of graphene while the one with the frequency of ω_q is obliquely incident. In a DFG process, the difference between the frequencies of incident beams determines the frequency of the generated wave $\omega_d = \omega_p - \omega_q$. The time evolution of system can be obtained from the equation of motion of the density matrix (Liouville equation) [90]:

$$\dot{\rho} = -\frac{i}{\hbar}[H, \rho] - \Gamma(\rho - \rho(t = 0)) \tag{3.8}$$

where Γ is the phenomenological damping constant that shows how fast system relaxes to its equilibrium state. The value of $\hbar\Gamma = 0.05eV$ is chosen based on the measured relaxation time ($\tau = 10^{-13}s$, where τ is the relaxation time [13]) using the impurity-limited dc mobility for graphene. The expected value of induced surface current is:

$$\mathbf{j} = 2e \sum_{B.Z.} Tr\left\{\hat{\rho}\frac{\partial \hat{H}}{\partial \mathbf{p}}\right\} \tag{3.9}$$

where the spin degeneracy is included as a factor of two in the calculations and the summation should be carried out in the whole Brillouin zone ($B.Z.$). The second order nonlinear term of induced current obtained in Eq. 3.9 has sum and difference frequency components of incident waves, $\mathbf{j}_e^{(2)}(\omega_p + \omega_q)$ and $\mathbf{j}_e^{(2)}(\omega_p - \omega_q)$. Here we focus on the difference frequency terms. The second order surface conductivity involved in the DFG is defined as follows (considering the positive frequency component):

$$j_s^{(2)}(\omega_d) = \sigma_{sij}^{(2)}(\omega_d, -\omega_q, \omega_p, \mathbf{k}_{q||}) E_i(\omega_p) E_j(-\omega_q) e^{-i(\mathbf{k}_{q||}.\mathbf{r} + \omega_d t)} \tag{3.10}$$

where $\mathbf{k}_{q||}$ is the tangential part of wave vector $\mathbf{k}_q$ on the graphene's plane, $\sigma_{sij}^{(2)}$ defines a tensor of rank 3 and the indices $i, j, s = 1$ ($i, j, s = 2$) shows the $\hat{x}(\hat{y})$ directions. The generated surface current in (3.10) has the frequency of $\omega_d = \omega_p - \omega_q$ and the spatial wave vector of $-\mathbf{k}_{q||}$. Figure 3.1(a) shows the schematic of the DFG process and the generated nonlinear current on the surface of graphene. Using the expression defined in Eq. 3.10,

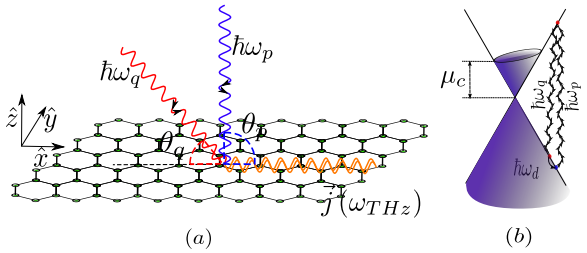

Figure 3.1: (a) Schematic of the DFG process. Two waves with frequencies ω_p and ω_q incident at the angles of $\theta_p = 90$ and θ_q. (b) The schematic of one of the possible transitions involved in the DFG. The photon with the energy $\hbar\omega_p$ excites the electron from the valance band to the conduction band while the photon with the energy of $\hbar\omega_q$ induces the inverse process. As a result of the final intraband transition, a THz photon is generated.

the tensor of $\sigma^{(2)}$ can be obtained from (see Appendix I):

$$\begin{aligned}
&\sigma^{(2)}_{sij}(\omega_d, -\omega_q, \omega_p, \mathbf{k}_{q||}) \\
&= -\frac{e\nu_F}{2\pi^2\hbar^2\omega_p\omega_q}\sum_{n,m=1}^{2}\sum_{l=1}^{2}\int_{K,K'} d^2k \\
&\left\{\left(\rho^{(0)}_{|m,\mathbf{k}\rangle} - \rho^{(0)}_{|l,\mathbf{k}\rangle}\right)\frac{\mu^i_{|l,\mathbf{k}\rangle|m,\mathbf{k}\rangle}\mu^j_{|n,\mathbf{k}'\rangle|l,\mathbf{k}\rangle}}{\left(\omega_{|l,\mathbf{k}\rangle|m,\mathbf{k}\rangle} - \omega_p\right) - i\Gamma} + \left(\rho^{(0)}_{|m,\mathbf{k}\rangle} - \rho^{(0)}_{|l,\mathbf{k}'\rangle}\right)\frac{\mu^j_{|l,\mathbf{k}'\rangle|m,\mathbf{k}\rangle}\mu^i_{|n,\mathbf{k}'\rangle|l,\mathbf{k}'\rangle}}{\left(\omega_{|l,\mathbf{k}'\rangle|m,\mathbf{k}\rangle} + \omega_q\right) - i\Gamma}\right. \\
&\left. - \left(\rho^{(0)}_{|l,\mathbf{k}'\rangle} - \rho^{(0)}_{|n,\mathbf{k}'\rangle}\right)\frac{\mu^i_{|n,\mathbf{k}'\rangle|l,\mathbf{k}'\rangle}\mu^j_{|l,\mathbf{k}'\rangle|m,\mathbf{k}\rangle}}{\left(\omega_{|n,\mathbf{k}'\rangle|l,\mathbf{k}'\rangle} - \omega_p\right) - i\Gamma} - \left(\rho^{(0)}_{|l,\mathbf{k}\rangle} - \rho^{(0)}_{|n,\mathbf{k}'\rangle}\right)\frac{\mu^j_{|n,\mathbf{k}'\rangle|l,\mathbf{k}\rangle}\mu^i_{|l,\mathbf{k}\rangle|m,\mathbf{k}\rangle}}{\left(\omega_{|n,\mathbf{k}'\rangle|l,\mathbf{k}\rangle} + \omega_q\right) - i\Gamma}\right\} \\
&\frac{\eta^s_{|m,\mathbf{k}\rangle|n,\mathbf{k}'\rangle}}{\omega_{|n,\mathbf{k}'\rangle|m,\mathbf{k}\rangle} - \omega_d - i\Gamma}
\end{aligned} \tag{3.11}$$

where $\eta^s_{|m,\mathbf{k}\rangle|n,\mathbf{k}'\rangle} = \langle n,\mathbf{k}'|\frac{1}{\nu_F}\frac{\partial\hat{H}}{\partial p_s}|m,\mathbf{k}\rangle$ (see Appendix I), $\hbar\omega_{|l,\mathbf{k}\rangle|m,\mathbf{k}\rangle}$ is the transition energy from the state $|m,\mathbf{k}\rangle$ to the state $|l,\mathbf{k}\rangle$, and $\mathbf{k}' = \mathbf{k} - \mathbf{k}_{q||}$. It is important to note that in the calculation of $\sigma^{(2)}$ both inter- and intra-band transitions are included, e.g. the term $\mu^i_{|l,\mathbf{k}\rangle|m,\mathbf{k}\rangle}$ when $l = m$ ($l \neq m$) shows an intra-band (inter-band) transition. While the integration should be carried out for the whole Brillouin zone, in the low energy limit, only the electrons near the Dirac points K and K' contribute to the wave-graphene interaction, and we thus calculate the integration only near these points [70]. Fig. 3.1(b) shows the schematic of one of the possible transitions involved in the DFG. The photon with the energy $\hbar\omega_p$ excites the electron from a lower state to a higher state. Another photon with

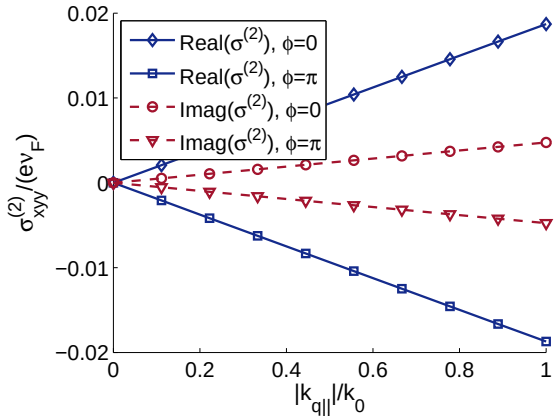

Figure 3.2: The second order nonlinearity of graphene as a function of incident wave momentum for $\mathcal{E}_F = 0.4eV$ and $\mathbf{j}^{dc} = \mathbf{0}$.

the energy of $\hbar\omega_q$ induces the inverse process from the higher state to a lower state. Since the second photon has a transverse momentum of $\mathbf{p}_p = \hbar\mathbf{k}_{q||}$ ($\mathbf{k}_{q||} = \mathbf{k}_q - (\mathbf{k}_q.\hat{z})\hat{z}$), the latter transition is not a straight one. For electron to return to its original position on the band structure, a photon with energy of $\hbar\omega_d$ should be emitted. Direction of the radiated THz photons can be calculated from the conservation of the momentum $\mathbf{k}_{d||} = -\mathbf{k}_{q||}$, where $\mathbf{k}_d$ is the wave vector of the generated THz photon. If $k_{d||} < \omega_d/c$, the induced nonlinear current on the graphene layer couples to the radiating modes in the free space. The angle of radiation from the graphene's plane is

$$\theta_d = \sin^{-1}\left(ck_{d||}/\omega_d\right). \tag{3.12}$$

However, when $k_{d||} > \omega_d/c$, the generated photons at the difference frequency are surface waves decaying in the perpendicular direction to the surface of graphene. In the limit of $k' \to k$, the equation 3.11 reduces to the one obtained in [70].

When the two primary waves propagating perpendicular to the graphene plane, $\boldsymbol{\sigma}^{(2)}$ becomes zero mainly because of the inversion symmetry in the graphene crystal [51]. The symmetry, however, can be broken using either a DC current [70], an obliquely incident beam [28, 73] or a strong magnetic field perpendicular to the surface of graphene. The first mechanism, DC biasing, breaks the symmetry of the band structure while the second approach, the wave momentum, breaks the symmetry of transitions. The magnetic field, on the other hand, leads to the formation of Landau levels [10, 91, 92] and can also break the symmetry by introducing spin splitting in graphene [10, 91]. The spin splitting can be disregarded unless the magnetic field's strength is several tens of Tesla [10]. The landau

level structure, however, becomes important when a magnetic field as strong as a few Tesla is being applied. For the study presented here, we assume that the strength of the magnetic field is small enough that the Landau level formation can be ignored in the calculation.

To differentiate between the different mechanisms that break the symmetry, we are expanding the obtained second order nonlinear tensor as follows (see Appendix I for the derivation of expansion):

$$\begin{aligned}\sigma^{(2)}_{sij}(\omega_d, -\omega_q, \omega_p, \mathbf{k}_{q||}) =& \chi^{(2)}_{sij}(\omega_d, -\omega_q, \omega_p) + \\ & T^{(2)}_{sija}(\omega_d, -\omega_q, \omega_p)\,(k_q)_a\end{aligned} \tag{3.13}$$

where $\chi^{(2)}_{sij}$ is a tensor of rank 3 which does not depend on $\mathbf{k}_q$, T_{sija} is a tensor of rank 4 representing the photon-drag effect in the nonlinearity, and the indices $i,\ j,\ a,\ s$ can have the values of 1 or 2. In our numerical analysis, we are calculating the value of $\sigma^{(2)}_{sij}$ from Eq. 3.11 and we are not directly calculating the tensors $\chi^{(2)}_{sij}$ and $T^{(2)}_{sija}$. To find the contribution of photon-drag in the nonlinearity, one can use the following approach:

$$\begin{aligned}&T^{(2)}_{sija}(\omega_d, -\omega_q, \omega_p)\,(k_q)_a = \\ &\frac{\sigma^{(2)}_{sij}(\omega_d, -\omega_q, \omega_p, \mathbf{k}_{q||}) - \sigma^{(2)}_{sij}(\omega_d, -\omega_q, \omega_p, -\mathbf{k}_{q||})}{2} \\ &\chi^{(2)}_{sij}(\omega_d, -\omega_q, \omega_p) = \\ &\frac{\sigma^{(2)}_{sij}(\omega_d, -\omega_q, \omega_p, \mathbf{k}_{q||}) + \sigma^{(2)}_{sij}(\omega_d, -\omega_q, \omega_p, -\mathbf{k}_{q||})}{2}\end{aligned} \tag{3.14}$$

where the value of $\sigma^{(2)}_{sij}$ should be calculated for the wave vectors $\mathbf{k}_{q||}$ and $-\mathbf{k}_{q||}$.

To incorporate the effect of DC current in our calculation, we note that this current can be written as $\mathbf{j}_{dc} = \sigma_{dc}\mathbf{E}_{dc}$ where $\mathbf{E}_{dc}$ is the in plane DC electric field. This electric field shifts the Fermi surface as shown in Fig. 3.1. The amount of this shift can be obtained from the ballistic transport theory in graphene as follows (see Appendix I for the details of calculation):

$$\mathbf{J}^{dc}(\Delta\mathbf{k}) = 4\sum_{l=1}^{2}\int \mathbf{j}^{e}_{|l,\mathbf{k}\rangle}\rho^{(0)}_{|l,\mathbf{k}-\Delta\mathbf{k}\rangle}D(\mathbf{k})T_{|l,\mathbf{k}\rangle}d^2k \tag{3.15}$$

where $\mathbf{J}^{dc}$ is the total DC current, $\Delta\mathbf{k}$ is the shift in the Fermi surface due to the DC current, $D(\mathbf{k}) = 1/(2\pi)^2$ is the 2D density of states, $T_{|l,\mathbf{k}\rangle}$ is the transmission probability of the electron in the state $|l,\mathbf{k}\rangle$ ($T_{|l,\mathbf{k}\rangle} = 1$ for the ballistic transport), and $\mathbf{j}^{e}_{|l,\mathbf{k}\rangle} =$

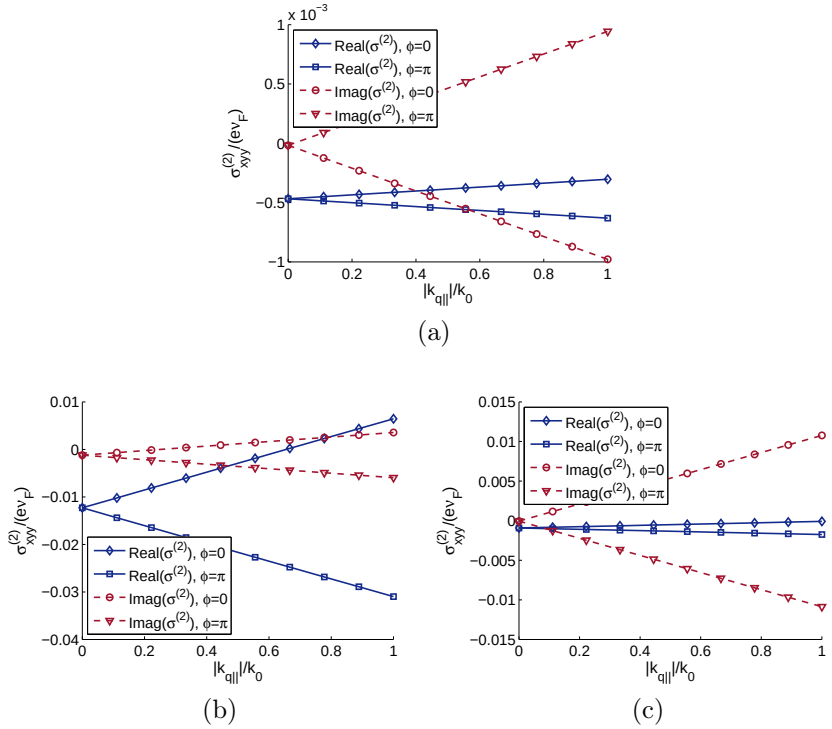

Figure 3.3: The effect of applied current density of $j_x^{dc} = 20\mu A/\mu m$ for different values of the Fermi level, $\mathcal{E}_F = 0.15eV$ (a), $\mathcal{E}_F = 0.4eV$ (b), and $\mathcal{E}_F = 0.55eV$ (c).

$e\nu_F(-1)^l\,[cos\theta_k\hat{x} + sin\theta_k\hat{y}]$ is the DC current due to an electron (or hole) with the momentum $\mathbf{p}_e = \hbar\mathbf{k}$. Because of the symmetry of the band-diagram, it is straightforward to conclude that $\mathbf{J}^{dc} \to \mathbf{0}$ when $\Delta\mathbf{k} \to \mathbf{0}$. Using Eq. 3.15, one can find the relation between $\mathbf{J}^{dc}$ and $\Delta\mathbf{k}$ for different values of the Fermi level. To find the nonlinearity tensor in the presence of the DC current, we replaced $\rho_{|m,\mathbf{k}\rangle}$ by $\rho_{|m,\mathbf{k}-\Delta\mathbf{k}\rangle}$ [70].

3.2 Numerical results for second order conductivity tensor

The value of $\sigma^{(2)}$ is calculated using the integration defined in Eq. 3.11 (for the details of calculation, refer to the supplemental information). Fig. 3.2 shows the nonlinear response of graphene (Eq. 3.11) for $\lambda_p = 2\pi c/\omega_p = 1554nm$ and $\lambda_q = 2\pi c/\omega_q = 1546nm$ ($\hbar\omega_q \approx \hbar\omega_q \approx 0.8eV$) when the DC current is equal to zero. The Fermi level of graphene is set to

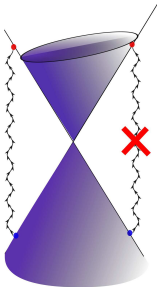

Figure 3.4: The broken symmetry of transitions when the Fermi energy level is approximately equal to the incident photo energy.

$\mathcal{E}_F = 0.4eV$ and the DFG at the frequency of $f_d = (\omega_p - \omega_q)/2/\pi = 1THz$ ($\lambda_d = 300\mu m$) is calculated. The wave with frequency of ω_p is perpendicularly incident to the graphene layer, while the wave with frequency of ω_q is obliquely incident. The propagation wave vector for the obliquely incident beam can be written as follows:

$$\mathbf{k}_q = k_{q||}\cos(\phi)\hat{x} + k_{q||}\sin(\phi)\hat{y} + \sqrt{k_0^2 - k_{q||}^2}\hat{z} \tag{3.16}$$

where $k_{q||} = k_q \sin(\theta)$, $k_0 = 2\pi/\lambda_{p,q}$ is the free space wave vector, ϕ is the angle of wave vector $\mathbf{k}_q$ form the $x-$axis, and $\hbar k_{q||} < \hbar k_0$ is the tangential part of the wave momentum on the graphene plane (θ and ϕ are the angles of the spherical coordinate). For the plane wave that propagates in the $\hat{x}$ direction ($\phi = 0$), the obtained nonlinearity (real and imaginary parts) shows a linear dependency on the tangential momentum of the incident wave. Because of this linear dependency, we can deduce that for the case of $J_{DC} = 0$ only the photo drag effect contributes to the nonlinearity. This becomes more obvious when we are investigating the second order nonlinearity for an incident wave that propagates in the $-\hat{x}$ direction ($\phi = \pi$). In this case ($\phi = \pi$), $\sigma^{(2)}$ change as follows:

$$\sigma^{(2)}(\phi = \pi) = -\sigma^{(2)}(\phi = 0) \tag{3.17}$$

Substituting Eq. 3.17 into Eq. 3.14, it is easy to verify that $\chi^{(2)}_{sij} \equiv 0$ as must be true because of the symmetry. Fig. 3.3(a-c) shows the effect of the applied DC current as the Fermi level changes from $0.15eV$ to $0.55eV$. In practice, the Fermi level of graphene can be controlled via the back gating of the underlying silicon wafer. The applied DC current is assumed to be $j_x^{dc} = 20\mu A/\mu m$. When $\mathcal{E}_F = 150meV$ (Fig. 3.3a) almost the same linear dependency of $\sigma^{(2)}$ on the wave vector can be observed showing that the drag effect is dominant when the Fermi level $\mathcal{E}_F$ is small compared to the incident photon energies. As the Fermi level reaches the incident photon energies ($\hbar\omega_p \approx \hbar\omega_q$), there is a

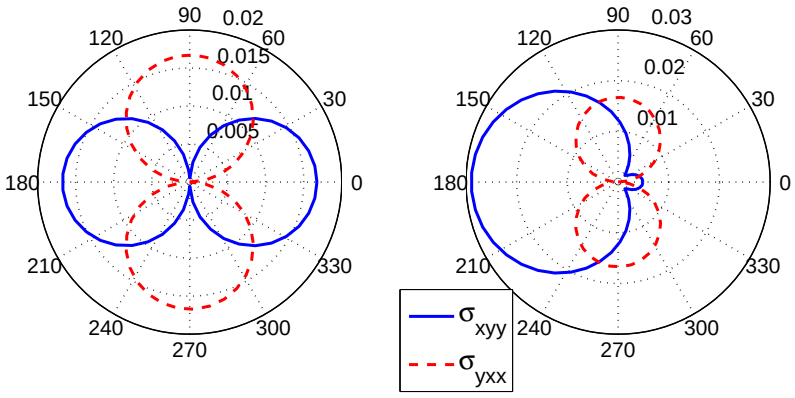

(a) (b)

Figure 3.5: Dependency of the second order nonlinearity to the angle of incident wave ϕ (Eq. 3.16) for (a) zero biased current, (b) $j_x^{dc} = 20\mu A/\mu m$. The wave vector of incident field is $k_{q||} = k_0 \sin(\pi/3)$.

significant shift in the nonlinear conductivity (Fig. 3.3b). Since the amount of shift does not depend on the incident photon momentum, it is easy to confirm that the DC effect only contributes to the tensor χ_{sij}. The importance of the Fermi level in enhancing the nonlinearity can be understood by looking at Fig. 3.4. As the Fermi level reaches the incident photon energy, some of transitions are allowed while the rest are blocked because of Pauli exclusion principle. For this specific value of the Fermi level, the symmetry of transitions are completely broken and the nonlinearity can be enhanced by a factor of 10. For a Fermi level higher than the incident photon energy (Fig. 3.3c), a smaller number of transitions are possible because of the fully occupied states in the conduction band and therefore the absolute value of $\sigma^{(2)}$ becomes smaller.

The polarization and the direction of the incident waves also play an important role in the second order nonlinearity. By changing the direction and the polarization of the incident waves, it is possible to control the amplitude and the phase of different components of the induced nonlinear current. As mentioned before, the direction of the obliquely incident beam directly affects the induced drag current and consequently changes the value of $\sigma^{(2)}$. Figure 3.5a shows the values of $\sigma^{(2)}_{xyy}$ and $\sigma^{(2)}_{yxx}$ ($J_{dc} = 0$) as the polar angle (ϕ) of obliquely incident beam changes. As expected, when the drag effect is dominant, the

angular dependency of $\sigma^{(2)}_{xyy}$ and $\sigma^{(2)}_{yxx}$ can be expressed as follows:

$$\begin{aligned} \sigma^{(2)}_{yxx} &\propto k_{qy} \propto \sin\phi \\ \sigma^{(2)}_{xyy} &\propto k_{qx} \propto \cos\phi. \end{aligned} \tag{3.18}$$

It is very important to note the symmetry of $\sigma^{(2)}$ for positive and negative values of ϕ. This symmetry along with the observed linear response in Fig. 3.2 confirm that the tensor T_{sija} is independent of the wave vector k_q. As the DC current in $\hat{x}$ direction increases to $J_{dc} = 20\mu A/\mu m$ (Fig. 3.5b), the absolute value of $\sigma^{(2)}_{xyy}$ dominates the nonlinear response while the value of $\sigma^{(2)}_{yxx}$ does not change. This fact demonstrates the dependency of the tensor χ_{sij} to the direction and the amplitude of J_{dc}. Because of the symmetry of the graphene layer, one expects to observe a similar variation in $\sigma^{(2)}_{yxx}$ as the DC current in $\hat{y}$ direction increases.

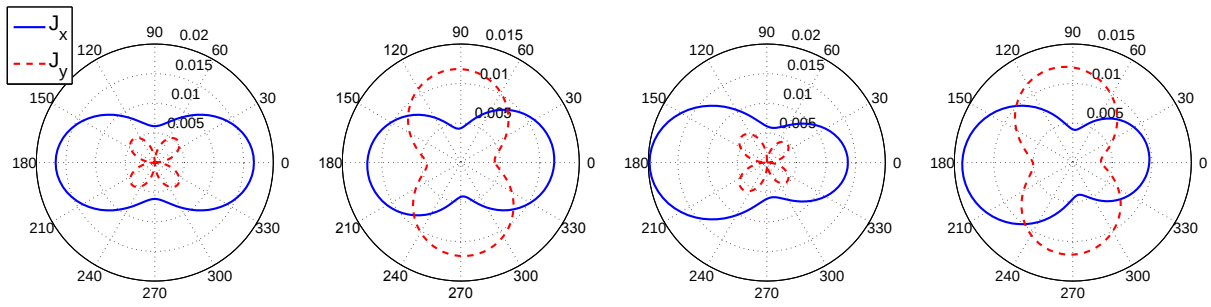

(a) (b) (c) (d)

Figure 3.6: The absolute value of induced nonlinear current as a function of the beam direction (ϕ) for linear (a) and circular (b) polarized waves ($\alpha = 0$ and $\alpha = 1$ in Eq. 3.19, respectively) when $\mathbf{J}^{dc} = \mathbf{0}$ and $k_{q||} = k_0 \sin(\pi/3)$. The figures (c) and (d) are the same as the ones in (a) and (b) for $J^{dc}_x = 5\mu A/\mu m$

The wave polarization is another degree of freedom affecting the DFG process. The polarizations control the DFG by inclusion of different components of $\sigma^{(2)}$ tensor in the induced current. For example, the nonlinear current of two $y-$polarized incident waves is proportional to $\sigma^{(2)}_{xyy}$ and $\sigma^{(2)}_{yyy}$, whereas for two circular polarized waves all the tensor components contribute to the $\mathbf{j}^{(2)}$. To study the effect of polarizations, we calculate $j^{(2)}_x$

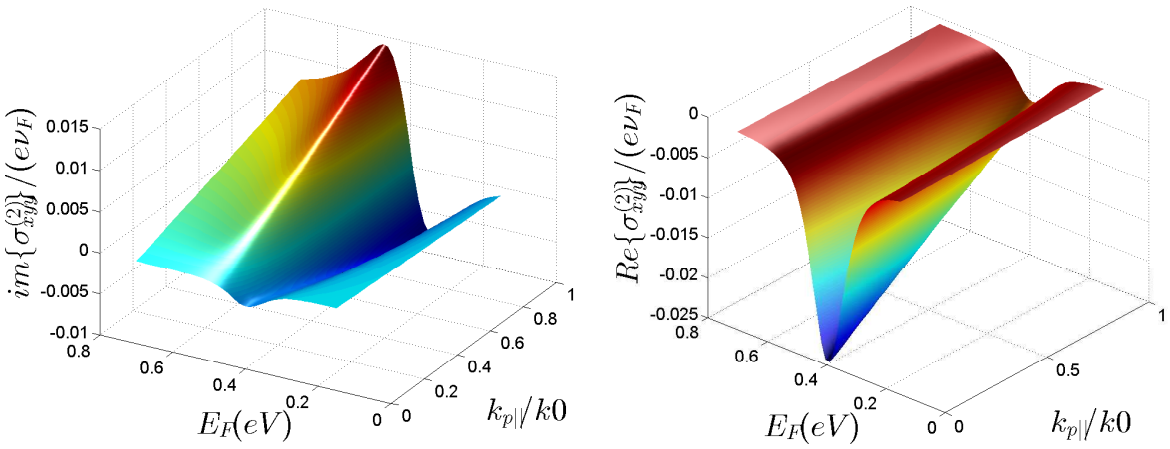

Figure 3.7: The imaginary (a) and the real (b) parts of second order conductivity at the difference frequency of $f_d = 1THz$ as a function of Fermi energy level and incident wave vector. The current density in graphene is $J_x^{dc} = 40\mu A/\mu m$.

and $j_y^{(2)}$ for the following incident plane waves:

$$\mathbf{E}(\omega_p) = \frac{\hat{y} + i\alpha\hat{x}}{\sqrt{1+\alpha^2}} e^{-i\frac{2\pi}{\lambda_p}z}$$
$$\mathbf{E}(\omega_q) = (-\sin\phi\hat{x} + \cos\phi\hat{y})\, e^{i\mathbf{k}_q.\mathbf{r}} \tag{3.19}$$

where $\alpha = 1$ ($\alpha = 0$) results in a circular (linear) polarized beam, ϕ is the angle of the incident wave with frequency ω_q, and $\mathbf{k}_d = \mathbf{k}_{d||} + k_{dz}\hat{z}$ ($k_{dz}^2 = (2\pi/\lambda_d)^2 - k_{d||}^2$). Figure 3.6a shows the induced nonlinear current $\mathbf{j}^{(2)}$, calculated using Eq. 3.10, as a function of ϕ for $\mathbf{J}_{dc} = \mathbf{0}$ and $\alpha = 0$. $j_x^{(2)}$ has 2-fold symmetry while $j_y^{(2)}$ has a 4-fold symmetry with a lower amplitude compared to that of $j_x^{(2)}$. On the contrary, when one of the beams is circular polarized ($\alpha = 1$), $j_x^{(2)}$ and $j_y^{(2)}$ both have 2-fold symmetry and the same maximum amplitude. Increasing J_x^{dc} breaks the angular symmetries and increases the amplitude of $\mathbf{j}^{(2)}$ at $\phi = \pi$.

Finally, we explore the second order nonlinearity as both the Fermi level $\mathcal{E}_F$ and the tangential wave momentum $\hbar k_{qx}$ changes. Figure 3.7 shows the real and the imaginary parts of $\sigma_{xyy}^{(2)}$ for $\hbar\omega_d = 4meV$ ($f_d = 1THz$) and $j_x^{dc} = 40\mu A/\mu m$. As can be seen in fig. 3.7, both tensors $\chi^{(2)}$ and $T^{(2)}$ are important in the nonlinearity. The drag effect mostly

contributes to the $Im\left\{\sigma^{(2)}_{xyy}\right\}$ and to the $Re\left\{\sigma^{(2)}_{xyy}\right\}$ at low Fermi energy levels. On the other hand, the DC current mostly contributes to the $Re\left\{\sigma^{(2)}_{xyy}\right\}$ when $\mathcal{E}_F \approx \hbar\omega_{p,q}$.

Chapter 4

Verification of the volumetric model of permittivity for graphene using a multipole-based numerical method

An essential part of the THz photomixer analysis is the simulation of graphene-nanparticle coupling using a commercially available FEM-based software (HFSS). The simulation of graphene in HFSS requires the use of a volumetric model for graphene. As explained earlier, the volumetric model of permittivity proposed for the graphene layer is an approximate model. To assess the accuracy of the conventional volumetric model, I develop a new numerical technique and propose a surface model to analyze the scattering from the flakes of graphene. The new approach, which is based on the multiple multipole method, expands electromagnetic field in terms of certain eigenmode solutions [93–99]. The solution of the scattering problem can be obtained by expanding the solution in different regions and enforcing suitable boundary conditions [30, 31, 100–102]. An important advantage of this formulation is the fact that the unknowns are the boundary fields as compared to the field over the entire volume, which form the unknown in the conventional FEM and FDTD.

The organization of this chapter is as follows. In Section 4.1, the formulation of the new approach and its application to an isolated graphene flake are described. Section 4.2 is devoted to the numerical study of various configurations of graphene flakes including isolated graphene flakes, closely spaced graphene flakes, and two-dimensional periodically patterned graphene flakes. In each section, a comparison between the numerical results of HFSS with those of the GMT is presented to assess the accuracy of volumetric model.

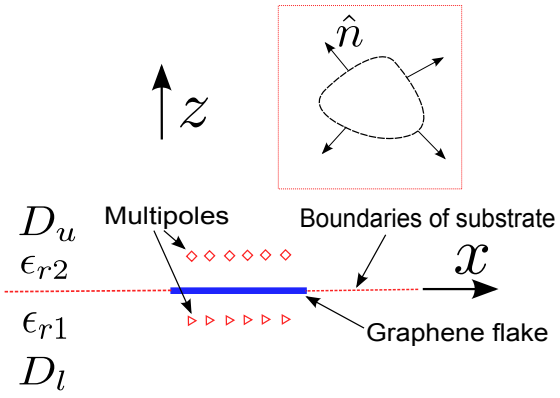

Figure 4.1: The schematic of a graphene flake on the interface of two dielectric half-spaces. Inset shows the top view of the graphene flake.

4.1 The formulation of multiple multipole method for the analysis of a patterned graphene structure

Spherical multipoles of the Maxwell's equations are used as the three dimensional (3D) expansion wave functions in each region. The radial components of TE_r and TM_r multipoles can be written as (time-harmonic variation of the form $exp(j\omega t)$ is chosen) [103]:

$$E_r^{nm} = \frac{n(n+1)}{j\omega\epsilon r^2} P_n^m(cos(\theta))\hat{H}_n^{(2)}(kr)e^{jm\phi} \qquad (4.1a)$$

$$-n \leq m \leq n$$

$$H_r^{nm} = \frac{n(n+1)}{j\omega\mu r^2} P_n^m(cos(\theta))\hat{H}_n^{(2)}(kr)e^{jm\phi} \qquad (4.1b)$$

$$-n \leq m \leq n$$

where P_n^m are the associated Legendre polynomials and $\hat{H}_n^{(2)}$ are the Schelkunoff-Hankel functions of the second kind. Considering the discontinuity of the problem in the $\hat{z}$ direction (we assume that graphene flakes lie on the $x-y$ plane), other types of multipoles such as TE_z and TM_z can also be used.

To solve the scattering problem, the solution space should be divided into a number of subregions and the multipoles expanding the electromagnetic wave in every subregion should be located outside that specific subregion [31]. Fig. 4.1 shows the graphene flake on the interface of two dielectric half-spaces. The multipoles located in the upper half-space

(D_u) produce the field in the lower half-space (D_l) and vice versa. The specific boundary condition that should be satisfied on the interface between two dielectric regions outside the part covered by the graphene flake is the continuity of tangential components of fields. On the graphene layer, the following set of boundary conditions should be satisfied:

$$\hat{z} \times (\mathbf{H}_u - \mathbf{H}_l) = \mathbf{J}_s, \quad \mathbf{J}_s = \sigma \mathbf{E} \tag{4.2a}$$

$$\mathbf{J}_s . \hat{n} = 0 \tag{4.2b}$$

$$\hat{z} \times (\mathbf{E}_u) = \hat{z} \times (\mathbf{E}_l) \tag{4.2c}$$

where $\vec{J}_s$ is the surface current; $\vec{H}_u$ and $\vec{H}_l$ are the magnetic fields in the upper and the lower sides of the interface, respectively; $\vec{E}$ is the electric field; $\hat{n}$ (inset of Fig. 4.1) is the unit vector perpendicular to the edge of the flake in the $x-y$ plane. It is worth mentioning that the boundary condition (4.2b) can be derived from (4.2a) provided that $\mathbf{H}$ can be evaluated at a point arbitrarily close to the flake boundary. Since the scattered fields are singular at the edge of the flake [104], imposing the boundary condition (4.2b) will exempt us from computing the fields close to their singular regions.

The multipoles located in the region D_u expand the field in the region D_l and vice versa. In addition to the multipoles in the regions D_u and D_l and in order to satisfy the edge conditions, extra multipoles should be placed close to the edge of the graphene layer. However, smoothening the field variation along the boundary needs a large number of multipoles which increases the run-time of numerical simulations. To alleviate this difficulty, an approach similar to the method of moment (MoM) is used. For this purpose, we add a number of new multipoles between each successive pair. The coefficients of these new multipoles are obtained from those of the aforementioned pair through an interpolation scheme. Fig. 4.2 shows this scheme. This approach is similar to the sampling of the roof-top function between C_l^{nm} and C_{l+1}^{nm}. The total electric field of such a set of multipoles can be written as:

$$\mathbf{E}_B^{nm}(\mathbf{r}) = \sum_{q=1-P}^{P-1} \mathbf{E}^{nm}\left(\mathbf{r} - \mathbf{r_q}\right) \frac{P - |q|}{P} \tag{4.3}$$

where $\mathbf{r_q}$ is the location of multipole number q (Fig. 4.2) and $(2P-1)$ is the total number of multipoles. Similar approach has been reported in [105, 106].

Fig. 4.3 shows an example of the multipole setting that is used for the analysis of a circular graphene flake. A carefully chosen multipole setting is needed to achieve the fast convergence [107]. Mutipoles near the edge of the graphene flake model the edge effects; the other multipoles produce the field distribution on the graphene flake. As shown in

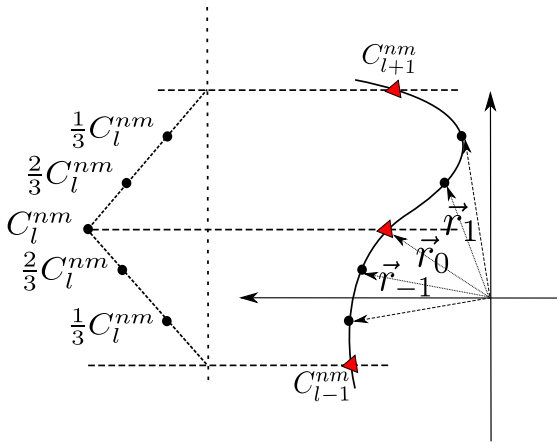

Figure 4.2: Locations and coefficients of a cluster of four multipoles located around the centered multipole C_l^{nm}.

Fig. 4.3b, the distance of all multipoles from the center of the graphene flake should be approximately equal. This criterion ensures that the contributions of all multipoles in producing the scattered field are the same. For the circular disk shown in Fig. 4.3, the multipoles, denoted by $\times$, are located on two circles with the radii of approximately $0.3a$ and $0.7a$ (a is the radius of the graphene disk) at the height of a and $0.4a$, respectively.

The inset of Fig. 4.3a shows how the boundary is discretized near the graphene flake. The boundary conditions (4.2a) and (4.2c) are applied on the points shown by diamond markers; the boundary condition (4.2b) is applied on the points shown by $*$ markers. Since the amplitude of field near the edges varies rapidly and in a singular manner, two boundary lines close to the actual physical boundary of the flake define the location of the nearest discretized points to the edge (Fig. 4.3a). The locations of these boundary lines are determined by the required accuracy with which the singular behavior of the field at the edge is to be modeled. As for our simulations, the proper value for the Δ_g is found to be $\Delta_g = D/20$ (D and Δ_g are defined in Fig. 4.3a). Smaller values of Δ_g will not have any substantial effect on the field distribution except in the region very close to the edge. Using the proposed multipole setting, the scattered fields in the regions D_u and D_l can be

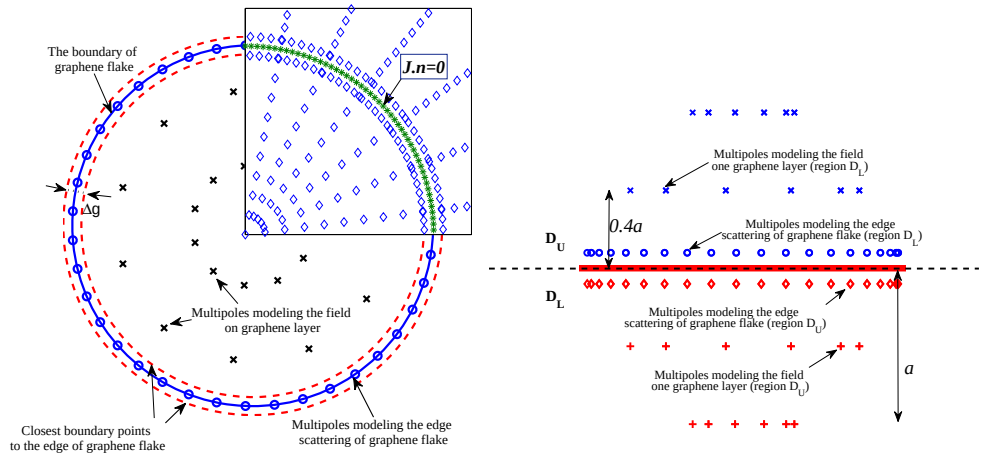

(a) (b)

Figure 4.3: The top view (a) and the side view (b) of the multipole setting for a graphene disk at the interface of two half-space dielectrics. The inset of (a) shows the discretization points near the graphene flake. The diameter of the flake is $D = 2a$.

written as follows:

$$\mathbf{E}_l^s(\mathbf{r}) = \sum_{i=1}^{M_u} \sum_{nm} C_i^{nm} \mathbf{E}^{nm}(\mathbf{r} - \mathbf{r}_i) + \sum_{i=1}^{M_u^B} \sum_{nm} C_i'^{nm} \mathbf{E}_B^{nm}(\mathbf{r} - \mathbf{r}_i^B) \tag{4.4a}$$

$$\mathbf{E}_u^s(\mathbf{r}) = \sum_{i=1}^{M_d} \sum_{nm} G_i^{nm} \mathbf{E}^{nm}(\mathbf{r} - \mathbf{r}_i') + \sum_{i=1}^{M_d^B} \sum_{nm} G_i'^{nm} \mathbf{E}_B^{nm}(\mathbf{r} - \mathbf{r}_i^{B\prime}) \tag{4.4b}$$

where C's are the unknown coefficients of the upper half-space (D_u) multipoles, G's are the unknown coefficients of the lower half-space (D_l) multipoles, $\mathbf{E}^{nm}$ is the electric field of TE_r or TM_r spherical multipoles defined in (4.1), and $\mathbf{E}_B^{nm}$ is given in (4.3). The value of M_u^B shows the number of multipoles close to the edge of the flake and M_u is the number of other mutlipoles in D_u. The same expressions exist for the magnetic fields. Primed coefficients, C' and G', are the coefficients of multipoles near the edge of the flake in D_u

and D_l, respectively. The boundary conditions are:

$$\hat{z} \times (\mathbf{H}_u^s + \mathbf{H}_u^{inc} - \mathbf{H}_l^s - \mathbf{H}_l^{inc}) = \mathbf{J}_s \tag{4.5a}$$

$$\mathbf{J}_s = \sigma \left(\mathbf{E}_t^s + \mathbf{E}_t^{inc}\right), \quad \mathbf{J}_s.\hat{n} = 0 \tag{4.5b}$$

$$\hat{z} \times \left(\mathbf{E}_u^s + \mathbf{E}_u^{inc}\right) = \hat{z} \times \left(\mathbf{E}_l^s + \mathbf{E}_l^{inc}\right). \tag{4.5c}$$

where $\mathbf{E}_t$ is the tangential component of the electric field on the $x-y$ plane and $\mathbf{E}^{inc}$ ($\mathbf{H}^{inc}$) is the electric field (magnetic field) of the incident wave. Considering the continuity of tangential components of the incident field over all boundaries, we have:

$$\hat{z} \times (\mathbf{H}_u^s - \mathbf{H}_l^s) = \mathbf{J}_s, \quad \mathbf{J}_s = \sigma \left(\mathbf{E}_t^s + \mathbf{E}_t^{inc}\right) \tag{4.6a}$$

$$\mathbf{J}_s.\hat{n} = 0 \quad \hat{z} \times \mathbf{E}_u^s = \hat{z} \times \mathbf{E}_l^s. \tag{4.6b}$$

To find the unknown coefficients, the boundary surfaces should be subdivided into a number of elements (more than the number of unknowns). It means that an over-determined problem should be solved. Truncating the summation in (4.4), the following matrix equation can be written for the upper and the lower half-spaces.

$$[\mathbf{E}^s]_l = [\boldsymbol{\mathcal{E}}]_l[C], \quad [\mathbf{H}^s]_l = [\boldsymbol{\mathcal{H}}]_l[C] \tag{4.7a}$$

$$[\mathbf{E}^s]_u = [\boldsymbol{\mathcal{E}}]_u[G], \quad [\mathbf{H}^s]_u = [\boldsymbol{\mathcal{H}}]_u[G] \tag{4.7b}$$

where $[C]$ ($[G]$) is the vector of unknown multipole coefficients in the upper (lower) half-space and $[\boldsymbol{\mathcal{E}}]_l$ is a vector of matrices that relates the vector $[C]$ to the the vector of electric field on discretized boundary points in the lower half-space. This vector of matrices can be written as $[\boldsymbol{\mathcal{E}}]_l = [\mathcal{E}_x]_l\hat{x} + [\mathcal{E}_y]_l\hat{y} + [\mathcal{E}_z]_l\hat{z}$. The other matrices $[\boldsymbol{\mathcal{H}}]_l$, $[\boldsymbol{\mathcal{E}}]_u$, and $[\boldsymbol{\mathcal{H}}]_u$ have similar definitions. To satisfy the boundary conditions, the following matrix equations should be solved:

$$\hat{z} \times ([\mathbf{H}^s]_u - [\mathbf{H}^s]_l) = [\sigma] \left([\mathbf{E}_t^s]_u + [\mathbf{E}_t^{inc}]_u\right) \tag{4.8a}$$

$$\hat{n}. \left([\mathbf{E}_t^s]_u + [\mathbf{E}_t^{inc}]_u\right) = \hat{n}. \left([\mathbf{E}_t^s]_l + [\mathbf{E}_t^{inc}]_l\right) = 0 \tag{4.8b}$$

$$\hat{z} \times [\mathbf{E}^s]_u = \hat{z} \times [\mathbf{E}^s]_l \tag{4.8c}$$

where $[\sigma]$ is the conductivity matrix on the discretized boundary. The boundary conditions in (4.8) can be put in a single matrix equation as:

$$[A][X] = [B]. \tag{4.9}$$

It is worth mentioning that in this method the value of sigma does not affect the computational complexity of the problem. Accuracy and uniqueness of obtained results are verified not only by checking the convergence of the GMT as the order and the number of multipoles increase but also by a direct comparison with those obtained by the FEM.

4.2 Numerical results

The graphene layer is modeled as a conducting surface whose conductivity can be obtained from the following analytical expression [13, 17] :

$$\sigma(\omega) = \frac{2e^2 k_B T}{\pi\hbar^2}\frac{j}{\omega + j\tau^{-1}}\ln(2\cosh(E_F/2k_BT)) + \frac{e^2}{4\hbar}\left(H(\omega/2) + \frac{4j\omega}{\pi}\int_0^\infty d\Omega \frac{H(\Omega) - H(\omega/2)}{\omega^2 - 4\Omega^2}\right) \tag{4.10}$$

where $\mathcal{E}_F = 0.4eV$ is the Fermi energy level of graphene, $T = 100K$ is the temperature of the graphene layer, $\tau = 10^{-13}s$ represents the effect of impurity [17], k_B is the Boltzmann constant, and $H(\Omega)$ is defined as follows [17]:

$$H(\Omega) = \frac{\sinh(\hbar\Omega/k_BT)}{\cosh(\hbar\Omega/k_BT) + \cosh(E_F/k_BT)} \tag{4.11}$$

Using this expression which is valid under the random phase approximation, we are calculating the conductivity for different values of the Fermi level. To compare results of the approach proposed herein with those of the conventional FEM, the equivalent permittivity of graphene for the FEM analysis is $\epsilon_r = 1 + \sigma(\omega)/j\omega\epsilon_0\Delta$, where $\Delta = 0.5nm$. In all numerical simulations that the graphene layer is assumed to be suspended in free space, the incident wave is as follows:

$$E^{inc}(z) = \hat{y}E_0 e^{-jkz} \tag{4.12}$$

where $E_0 = 1$ is the amplitude of the incident electric field and the plane wave is propagating perpendicular to the surface of the graphene.

4.2.1 Scattering from isolated graphene flakes

The multipole setting shown in Fig. 4.3 is used to calculate the scattering from an isolated disk of graphene in free space. The radius of the disk is $a = 500nm$, the number of multipoles near the edge is 30 and the number of multipoles on each side of graphene layer is 14. To keep the number of unknowns as small as possible, the maximum value of n in (4.1) for all the multipoles is 2. Wherever a multipole with a higher order is needed, closely spaced multipoles of order 2 can be used to mimic the field variations of higher order multipoles. The maximum value of the error, as defined below, is less than 3%.

$$e = \frac{\|[A][X] - [B]\|}{\|[B]\|} \tag{4.13}$$

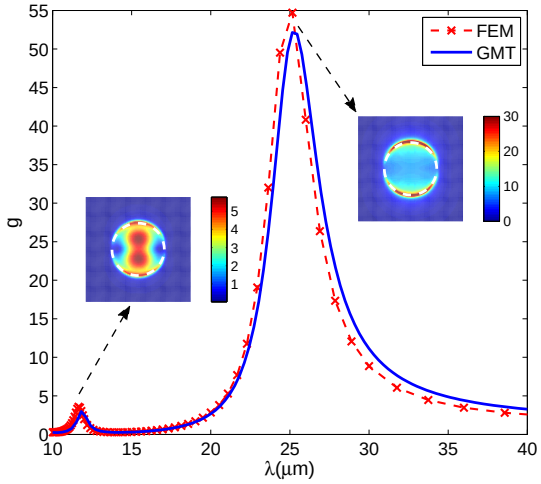

Figure 4.4: The field enhancement factor g (Equation (4.14)) for an isolated circular graphene flake as a function of wavelength. The insets show the electric field distributions at the resonance frequencies. The dotted curve is the FEM result.

To compare the obtained numerical results with those of the FEM method, an enhancement factor g is defined as follows:

$$g = \frac{\int_S \|\mathbf{E^s}\|^2 \, dS}{\int_S \|\mathbf{E^{inc}}\|^2 \, dS} \tag{4.14}$$

where the surface S is a rectangle with dimensions of $4a \times 4a$ located at the center of the graphene disk. Since the FEM solution inside the graphene layer is not a part of the scattering solution, the surface of rectangle S is located outside the disk at the distance of $5nm$ below the graphene layer. The factor g represents the enhancement of the electric field energy near the graphene flake. The incident wave is a plane wave propagating perpendicular to the surface of graphene. Fig. 4.4 shows the enhancement obtained by the GMT as compared to the FEM results. As shown, the results match quite good. The field distributions for the peak values of g are also plotted. These peaks indicate the plasmon resonances of the graphene circular disk. To investigate the significance of the $\mathbf{J}.\hat{n} = 0$ boundary condition around the edges of the graphene flake, a graphene rectangle with the dimensions of $1\mu m \times 1\mu m$ at the frequency of $5THz$ is simulated under two different conditions: 1) using the correct boundary condition at the edge; and 2) ignoring the boundary condition at the edge. Fig. 4.5 shows the field distributions for these two cases. Applying the $\mathbf{J}.\hat{n} = 0$ boundary condition increases the maximum value of electric

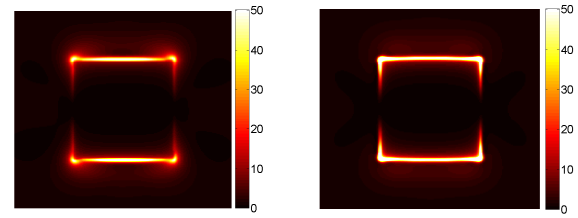

(a) (b)

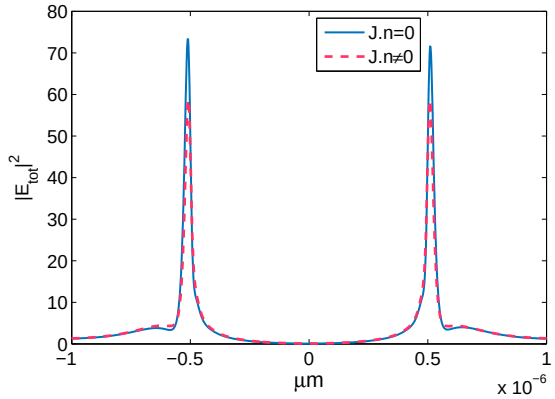

(c)

Figure 4.5: (a) Distribution of $|\mathbf{E}|^2$ on the surface of the graphene flake. (b) The distribution of $|\mathbf{E}|^2$ on the surface of the same graphene flake when the surface current normal to the boundary of flake is not set to be zero. (c) The amplitude of $|\mathbf{E}|^2$ over the vertical line bisecting the rectangle for both cases.

field around the edges. Furthermore, the true field distribution (Fig. 4.5a) shows correct singular behavior close to the edge. The amplitude of the scattered electric field over the vertical line bisecting the rectangle is plotted in Fig. 4.5c. As shown, the field distribution when the boundary condition (4.2*b*) is applied (Fig. 4.5a) is different from that obtained without imposing the correct boundary condition (Fig. 4.5b). This shows the significance of imposing correct boundary conditions over the surface and the edge of the graphene layer. It is important to note that the boundary condition (4.2*b*), exempt us from getting near the edge of the flake. However, if the number of discretization points around the edge of flake increases (This would results in a higher simulation time) the field distributions for both cases (Fig. 4.5c) become identical.

The formulation derived in Section 4.1 can also be used to obtain the scattered field

for a graphene layer on a substrate ($\epsilon_{r1} = \epsilon_s$ and $\epsilon_{r2} = 1$ in Fig. 4.1). The field of upper half-space multipoles should be calculated in a homogeneous medium with $\epsilon = \epsilon_s$, and the incident plane wave should be as follows [103]:

$$E^{inc}(z) = \hat{y} \begin{cases} e^{-jk_0 z} + \frac{\eta_s - \eta_0}{\eta_s + \eta_0} e^{jk_0 z} & z \geq 0 \\ \frac{2\eta_s}{\eta_s + \eta_0} e^{-jk_0 \sqrt{\epsilon_s} z} & z < 0 \end{cases} \tag{4.15}$$

where $\eta = \sqrt{\mu/\epsilon}$ is the intrinsic impedance of the substrate (η_s) or air (η_0). To verify our method, we compare the obtained field distribution for a graphene triangle on the silicon substrate ($\epsilon_s = 12$) with those of the FEM. Figure 4.6 shows the absolute value of the electric field obtained using the GMT method at the frequency of $5THz$. The obtained field distribution matches that of the FEM shown in Fig. 4.6b.

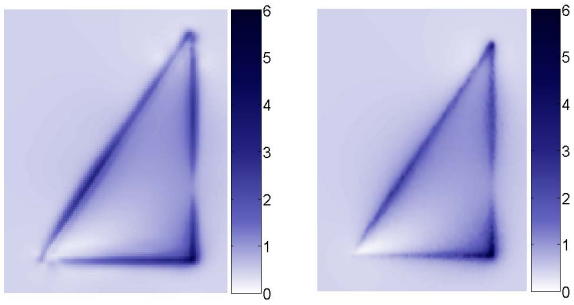

(a) (b)

Figure 4.6: (a) The field distribution of a triangle graphene flake with the dimensions of $1\mu m \times 1.5\mu m$ on top of the silicon substrate. The plot shows the electric field distribution inside the silicon at a distance of $5nm$ below the graphene layer. (b) The same structure is simulated using the FEM.

4.2.2 Plasmon resonances of graphene dimers

Plasmon resonances of coupled metallic nanoparticles generate a high intensity electric field region, which can be used for high resolution sensing and imaging. Dimers of graphene flakes located in proximity to each other also show field enhancements which are much stronger than those of similar dimers made of gold and silver [29]. Here, the proposed

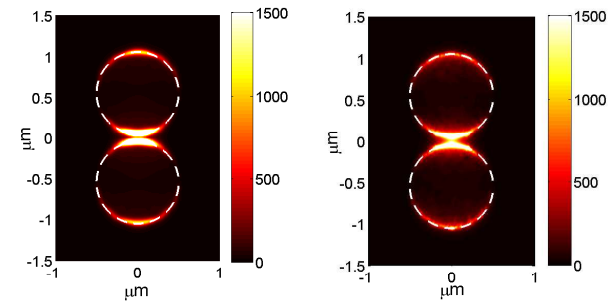

(a) (b)

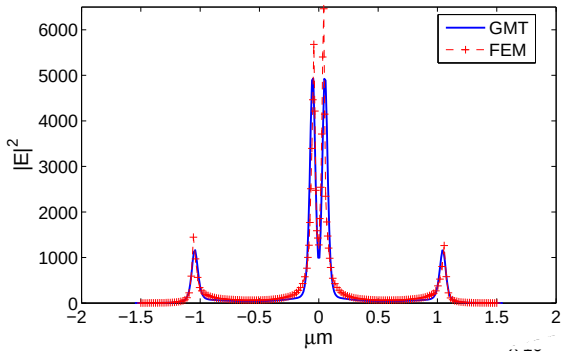

(c)

Figure 4.7: The distribution of $|\mathbf{E}|^2$ for two coupled graphene nanodisks obtained by the proposed method (a) and by the FEM (b). The Distribution of $|\mathbf{E}|^2$ over the vertical line bisecting both disks (c).

method is used to study the enhancement of the electric field between two closely spaced graphene disks.

Figure 4.7a shows the distribution of $|\mathbf{E}|^2$ between two closely spaced graphene nanoparticles as computed by the GMT method at the distance of $5nm$ below the graphene layer. The multipole setting for each disk is similar to those used for isolated flakes. The diameter of flakes is $1\mu m$ and the spacing between them is $100nm$. To show the accuracy of the proposed method, we plotted the electric field distribution at the wavelength where the maximum enhancement can be achieved, $\lambda = 26.5\mu m$. As can be seen, an electric field enhancement as large as 40 times can be achieved in the hot spot (an enhancement of 1600 times in $|\mathbf{E}|^2$). Figure 4.7b shows the results of the analysis of the same structure using the FEM. To compare the results of these two methods, the amplitude of $|\mathbf{E}|^2$ over the

vertical line bisecting both disks is plotted in Fig. 4.7c. As can be seen, the FEM results match the result of the GMT method, meaning that a volumetric model ($\Delta = 0.5nm$) is as accurate as the surface model for this range of frequency.

4.2.3 Periodically patterned graphene structures

Figure 4.8 shows the multipole setting for the analysis of the periodic structure. To analyze a periodically patterned graphene structure, the multipole setting of a single disk (Fig. 4.3) should be changed as follows. A number of multipoles should be placed outside Bloch boundaries. These multipoles generate the field inside the Bloch boundaries. In addition, the field generated by multipoles shown by $\times$ and are connected by a line (Fig. 4.8) should be calculated using the interpolating scheme presented in (4.3). To analyze the periodically

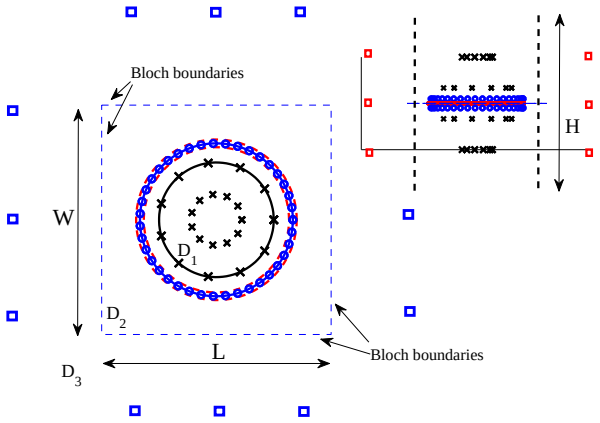

Figure 4.8: The upper view of multipole setting for the analysis of periodic graphene nanodisks. The inset shows the side view of the multipole setting.

patterned structure, in addition to the boundary conditions in (4.6), the following periodic boundary conditions should be satisfied:

$$\mathbf{E}(x = L/2, y, z) = e^{-j\kappa L}\mathbf{E}(x = -L/2, y, z) \tag{4.16a}$$

$$\mathbf{H}(x = L/2, y, z) = e^{-j\kappa L}\mathbf{H}(x = -L/2, y, z) \tag{4.16b}$$

$$\mathbf{E}(x, y = W/2, z) = e^{-j\kappa' W}\mathbf{E}(x, y = -W/2, z) \tag{4.16c}$$

$$\mathbf{H}(x, y = W/2, z) = e^{-j\kappa' W}\mathbf{H}(x, y = -W/2, z) \tag{4.16d}$$

where κ and κ' are the Bloch wave numbers, L and W are the periodicity of the flake in x and y direction, respectively. To satisfy the Bloch boundary conditions, a number of

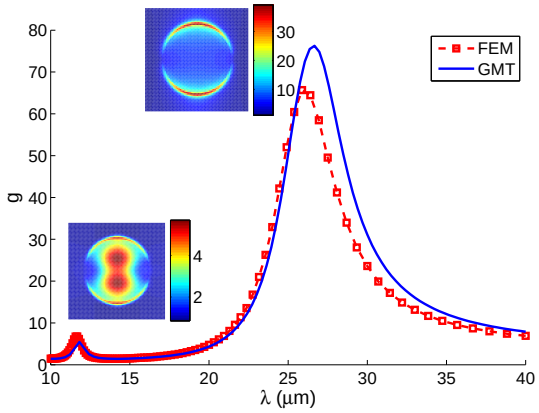

Figure 4.9: The electric field energy enhancement factor g calculated for the 2D periodic nanodisks of graphene structure. The insets show the amplitude of electric field at the peak wavelengths. The results of the proposed method are compared with those of the FEM.

multipoles should be located outside of the Bloch boundaries (Bloch multipoles). To keep the number of Bloch multipoles as small as possible, the height of these multipoles should be the same as that of the inner multipoles. Fig. 4.8 and its inset show the exact locations of these mutlipoles. The Bloch multipoles are located at the distance of $L/2$ (Note that $L = W$) from the Bloch boundaries. For the numerical evaluation, the solution space is truncated to $-15a < H < 15a$ (a is the radius of flake) in the $\hat{z}$ direction. Increasing H beyond this region would not substantially change the results as all the multipoles are located at the maximum distance of a from the flake. Figure 4.9 shows the enhancement factor g (Equation (4.14)) obtained from the electric field distribution inside the Bloch boundaries. The Bloch wave vectors are $\kappa = 0$ and $\kappa' = 0$. The incident wave is a plane wave polarized in $\hat{y}$ direction and propagating in $\hat{z}$ direction. The maximum error as defined in (4.13) is about 4%. The FEM results (Fig. 4.9) matches the obtained results.

Chapter 5

The graphene-based photomixer design

5.1 Introduction

Chapter 2 explained that the plasmon-assisted coupling enhances nonlinear processes such as the Raman scattering in graphene. Extraordinary Raman enhancements as high as 1000 times were achieved for our fabricated nanocrescent structures. The Raman scattering, however, is not a frequency mixing process and the process we are interested in our study involves the difference frequency generation (DFG).

In a DFG process, the wave momentum and the DC current are two decisive while inherently different factors. Pertinent to their inherent differences, these two factors respond differently to the plasmon enhancements. One expects the DFG due to the DC current to be scaled up the same way that absorption increases. In contrast, the drag effect is not only affected by the enhancement in the absolute value of fields but also by the shape of the wave front. The shape of the wave front brings a third factor in the analysis, that is the geometry of the nanoparticles.

Employing the volumetric model of the graphene layer developed in Chapter 4, in this chapter, a comprehensive study of a new graphene-based THz mixer is presented. We start by investigating the role of nanoparticles in the field enhancement and symmetry breaking. We then focus our study on the THz radiation from graphene in the presence of the proposed THz antenna.

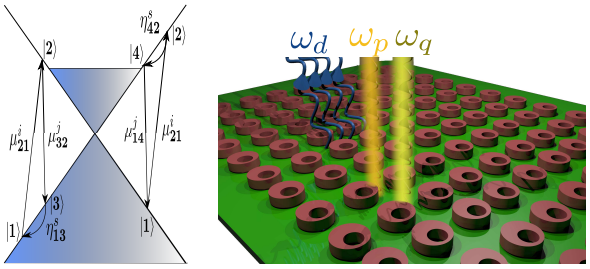

(a) (b)

Figure 5.1: The transitions involved in the DFG process (Eq. A.35) (a) and the schematic of nanostructure on top of the graphene layer (b). Two waves with frequencies of ω_p and ω_q mix in graphene resulting in a photon with frequency of ω_d. The graphene layer is placed on a $Si/SiO_2(300nm)$ layer.

5.2 Nonlinear response of graphene in the presence of nanoparticles

It is theoretically proven [28] and experimentally demonstrated [73,108] that the aforementioned drag effect is an efficient mechanism in the photomixing process, resulting in the generation of THz photons in graphene. Although the nonlinearity caused by the drag effect is strong [28], extreme localization of the electromagnetic field is still essential to make the nonlinear interaction of light and graphene sufficiently strong. Meanwhile, the incoming photons at the fundamental frequencies should be guided into the graphene with a large enough in-plane linear momentum. These conditions can be simultaneously satisfied in a graphene layer integrated with an asymmetric nanostructured supporting plasmonic mode with a very small mode volume. The asymmetry introduced by the nanoparticles causes the induced field to have large enough in-plane linear momentum required for dragging the quasiparticles.

For a free standing graphene layer, the induced nonlinear current at the difference frequency of ω_d for two obliquely incident plane waves at the frequencies ω_p and ω_q ($\omega_d = \omega_p - \omega_q$) is related to the phasors of the incoming plane waves as

$$J_s(\omega_d) = \sum_{j,k} \sigma^{(2)}_{sjk}(\omega_d, \omega_p, -\omega_q, \mathbf{k}_p, \mathbf{k}_q) E_j(\omega_p, \mathbf{k}_p) E^*_k(\omega_q, \mathbf{k}_q) \tag{5.1}$$

where the tensor $\sigma^{(2)}_{sjk}(\omega_d, \omega_p, -\omega_q, \mathbf{k}_p, \mathbf{k}_q)$ is the second order conductivity tensor and $E_i(\omega_p)$

is the i'th cartesian component of the electric field phasor $\mathbf{E}(\omega_p, \mathbf{k}_p) = \mathbf{E}_p \exp(i\mathbf{k}_p.\mathbf{r})$. For a graphene layer that lies on the xy plane the indices s, j and k run over x and y only. The tensor $\overline{\sigma}^{(2)}$ is calculated by a quantum mechanical approach employing the velocity gauge in which the momentum of the incoming photons is included in the formulation. Considering the possible transitions involved in the DFG process (Fig. 5.1a), the elements of the second order conductivity tensor $\overline{\sigma}^{(2)}$ are calculated as (see Appendix I):

$$\sigma^{(2)}_{sij} = -\frac{2e\nu_F}{\hbar^2\omega_p\omega_q}\int_{K,K'}\frac{d^2k_1}{4\pi^2}\Bigg\{\Bigg[\frac{\rho^{(0)}_{\mathbf{k}_1}-\rho^{(0)}_{\mathbf{k}_2}}{(\omega_{\mathbf{21}}-\omega_p)-i\Gamma} - \frac{\rho^{(0)}_{\mathbf{k}_2}-\rho^{(0)}_{\mathbf{k}_3}}{(\omega_{\mathbf{32}}+\omega_q)-i\Gamma}\Bigg]\frac{\mu^i_{\mathbf{21}}\mu^j_{\mathbf{32}}\eta^s_{\mathbf{13}}}{\omega_{\mathbf{13}}-\omega_d-i\Gamma} + \Bigg[\frac{\rho^{(0)}_{\mathbf{k}_4}-\rho^{(0)}_{\mathbf{k}_1}}{(\omega_{\mathbf{14}}+\omega_q)-i\Gamma} - \frac{\rho^{(0)}_{\mathbf{k}_1}-\rho^{(0)}_{\mathbf{k}_2}}{(\omega_{\mathbf{21}}-\omega_p)-i\Gamma}\Bigg]\frac{\mu^j_{\mathbf{14}}\mu^i_{\mathbf{21}}\eta^s_{\mathbf{42}}}{\omega_{\mathbf{42}}-\omega_d-i\Gamma}\Bigg\} \tag{5.2}$$

where $\hbar\omega_{\mathbf{21}}$ is the transition energy from the state $|\mathbf{1}\rangle$ to $|\mathbf{2}\rangle$, $\mu^i_{\mathbf{21}}$ is the induced dipole caused by the transition from the state $|\mathbf{1}\rangle$ to $|\mathbf{2}\rangle$ (Fig. 5.1a), and $\rho^{(0)}_{\mathbf{k}_1}$ is the Fermi-Dirac distribution for the state $|\mathbf{1}\rangle$ with the wave vector $\mathbf{k}_1$. Other parameters in Eq. A.35 are defined similarly. The conservation of momentum enforces the conditions $\mathbf{k}_2 = \mathbf{k}_1 + \mathbf{k}_p$, $\mathbf{k}_3 = \mathbf{k}_1 + \mathbf{k}_p - \mathbf{k}_q$, and $\mathbf{k}_4 = \mathbf{k}_1 + \mathbf{k}_q$. The vector operators $\hat{\boldsymbol{\mu}}$ and η^s are defined as ($\xi = 1$ for the Dirac cone K and $\xi = -1$ for the Dirac cone K'):

$$\hat{\boldsymbol{\mu}} = \frac{-i}{2}e\nu_F\left(\sigma_x\hat{x} + \xi\sigma_y\hat{y}\right), \quad \hat{\boldsymbol{\eta}}^s = \frac{1}{\nu_F}\frac{\partial\hat{H}}{\partial p_s} \tag{5.3}$$

where σ_i's, ν_F and p_s are the Pauli matrices, the Fermi velocity ($\sim 10^6$m/s) and the Bloch momentum respectively.

We now proceed to find the induced current at the frequency of ω_d for the plasmonic structure shown in Fig. 5.1b. As schematically shown in the figure, the periodic array of asymmetric gold nanoparticles is placed on the top of a graphene layer. The graphene sheet is placed over a multilayer structure. The structure is excited by two monochromatic laser fields illuminating the structure in perpendicular direction from the top. The nanoparticles are appropriately shaped to be at resonance around the wavelength of the incoming photons and therefore the induced field is highly non-uniform on each cell . In order to calculate the induced current, the linear analysis is performed to find the induced electric fields at the frequencies of ω_p and ω_q. The induced field is then decomposed in terms of the plane waves to be plugged into Eq. (5.1). Assuming the periodicities of W and L along the x

and y axes respectively, the tangential electric field on the graphene layer is expanded in terms of the Floquet modes as

$$\mathbf{E}_t(\omega_p) = (\hat{x}\hat{x} + \hat{y}\hat{y}) \cdot \mathbf{E} = \sum_{\alpha,\beta} \mathcal{E}^x_{\alpha\beta} e^{i\mathbf{G}_{\alpha\beta}\cdot\mathbf{r}}\hat{x} + \sum_{\alpha,\beta} \mathcal{E}^y_{\alpha\beta} e^{i\mathbf{G}_{\alpha\beta}\cdot\mathbf{r}}\hat{y} \tag{5.4}$$

where $\mathcal{E}^x_{\alpha\beta}$ and $\mathcal{E}^y_{\alpha\beta}$ are the Fourier expansion coefficients (See Appendix I). The vectors $\mathbf{G}_{\alpha\beta} = \frac{2\pi\alpha}{L}\hat{x} + \frac{2\pi\beta}{W}\hat{y}$, where α and β are integers, are spatial harmonics defined in reciprocal space.

Since $\omega_d \ll \omega_p,\ \omega_q$, we can safely assume that the field distributions at ω_p and ω_q are almost identical for a similar excitation. That allows us to use equal Fourier coefficients to expand the field distributions. The induced current at the difference frequency ω_d is then given by

$$\begin{aligned} J_s(\mathbf{r}, \omega_d) &= \sum_{\alpha,\beta,\alpha',\beta'} \sum_{a,b=1}^{2} \sigma^{(2)}_{sab}(\omega_d, \omega_p, \omega_q, \mathbf{G}_{\alpha,\beta}, \mathbf{G}_{\alpha',\beta'}) \\ &\qquad (\mathcal{E}_{\alpha\beta})_a \left(\mathcal{E}^*_{\alpha'\beta'}\right)_b e^{i(\mathbf{G}_{\alpha,\beta} - \mathbf{G}_{\alpha',\beta'})\cdot\mathbf{r}} \\ &= \sum_{mn} \mathcal{J}_{s,mn} e^{i\mathbf{G}_{m,n}\cdot\mathbf{r}} \end{aligned} \tag{5.5}$$

where $(\mathcal{E}_{\alpha\beta})_1 = \mathcal{E}^x_{\alpha\beta}$ and $(\mathcal{E}_{\alpha\beta})_2 = \mathcal{E}^y_{\alpha\beta}$. Since $L, W \ll \lambda_d$ (λ_d is the wavelength of the difference frequency), only the term $\vec{\mathcal{J}}_{00}(\omega_d)$ contributes to radiation. All the higher spatial harmonics are evanescent. The total radiating component of THz current is obtained as

$$J^{rad}_s(\omega_d) = \mathcal{J}_{s,00}(\omega_d) = \sum_{\alpha,\beta} \sum_{a,b=1}^{2} \sigma^{(2)}_{sab}(\omega_d, \omega_p, \omega_q, \mathbf{G}_{\alpha,\beta}, \mathbf{G}_{\alpha,\beta})\, \mathcal{E}^{(a)}_{\alpha\beta} \mathcal{E}^{(b)*}_{\alpha\beta} \tag{5.6}$$

The radiating current obtained in Eq. 5.6 is spatially uniform. It is straightforward to show that the condition $\mathcal{E}_{-nm} \neq \mathcal{E}_{nm}$ or $\mathcal{E}_{n(-m)} \neq \mathcal{E}_{nm}$ guarantees nonzero THz radiating current. These conditions can be interpreted as introducing a phase progress over the graphene layer by asymmetric excitation of the Floquet modes.

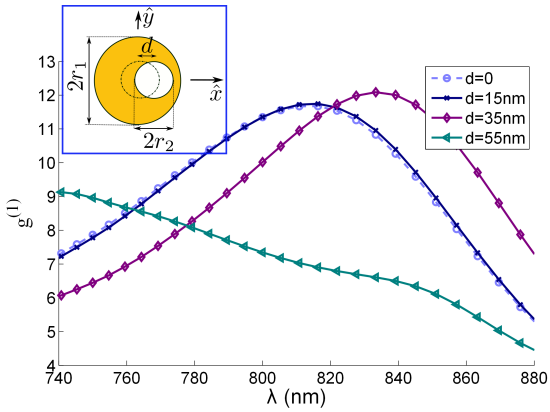

Figure 5.2: The field enhancement factor $g^{(1)}$ calculated on the graphene layer for four different periodic arrays of gold nanoparticles. The inset shows the geometry of nanoparticles.

5.3 Numerical results

5.3.1 Design considerations and figures of merit

The schematic of the proposed structure is depicted in Fig. 5.1b. The graphene layer is integrated with a periodic arrangement of nano-rings with the outer radius of $r_1 = 90$nm and the inner radius of $r_2 = 40$nm . The height of nanoparticles is 65nm and a buffer layer of SiO_2 with thickness of 300nm is placed between the graphene layer and the silicon wafer. The dimensions of the symmetric nanorings and the thickness of SiO_2 layer are optimized to obtain the highest possible enhancement on the graphene layer. The figure of merit characterizing the performance of the plasmonic nanostructure in the linear regimes is the first order enhancement factor defined as

$$g^{(1)} = \frac{1}{WL}\int_{\text{unit cell}} \frac{|\mathbf{E}|^2}{|\mathbf{E}_0|^2}\mathrm{d}x\mathrm{d}y \tag{5.7}$$

where E_0 is the electric field amplitude of the incident wave. Figure 5.2 shows the achieved enhancement $g^{(1)}$ as a function of wavelength for nanorings with reduced symmetry. To reduce the symmetry, the inner cylinder of the nanoring is displaced by the amount of d along the x axis (Inset of Fig. 5.2). The enhancement peaks for $d/r_2 = 0$ and $d/r_2 = 0.17$ are at $\lambda_0 \sim 800$nm; however, as the displacement increases the wavelength of maximum enhancment significantly varies. The electric field distributions for the different values of

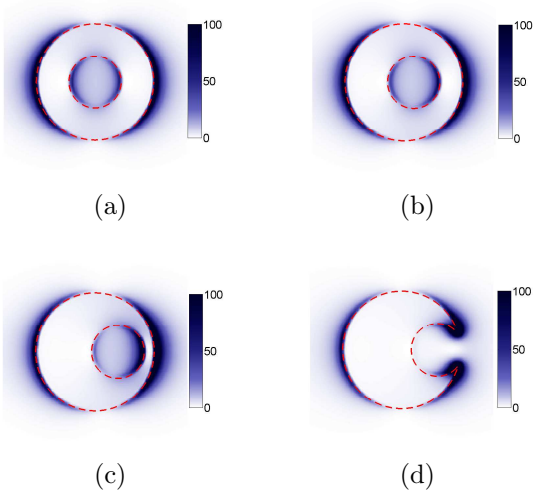

(a) (b)

(c) (d)

Figure 5.3: The distribution of $|\mathbf{E}|^2$ for the symmetric case ($d = 0$) (a) and for the asymmetric cases $d/r_2 = 0.17$ (b), $d/r_2 = 0.4$ (c), $d/r_2 = 0.6$ (d).

the displacement are shown in Fig. 5.3a-5.3d. It is noted that, by increasing the shift d/r_2 from 0 to 0.6, the field distribution becomes more asymmetric.

For the DFG analysis, we assume that the wavelengths of the incident fields are $\lambda_p, \lambda_q \approx$ 800nm ($\lambda_p = 801$nm and $\lambda_q = 799$nm) and the difference frequency is $\omega_d = \omega_p - \omega_q = 2\pi(1\text{THz})$. Having the field distribution on the graphene layer, the radiating part of induced nonlinear current can be calculated using Eq. (5.6). To compare the obtained results when the nanoparticles are present with those of the bare graphene layer, we define the nonlinear enhancement factor, g_2 as:

$$g^{(2)} = \frac{\left|\vec{\mathcal{J}}_{00}^{MNP}\right|^2}{|\mathbf{J}^B|^2} \tag{5.8}$$

where $\vec{\mathcal{J}}_{00}^{MNP}$ is the uniform part of the induced THz current when the metal nanoparticles are present and $\mathbf{J}^B$ is the induced THz current when two waves are incident on a bare graphene layer at a certain incident angle like 45°. The factor $g^{(2)}$ defined in Eq. (5.8), shows the enhancement in the radiated THz power [109].

The amount of the gain achieved for three different value of d (Fig. 5.2) are plotted in Fig. 5.4; the insets show the field enhancement of the real part of E_x and the normalized amplitude of spatial expansion functions for $|\alpha| < 20$ and $\beta = 0$. The non-symmetric distributions of the Floquet modes expansion coefficients becomes more pronounced as the

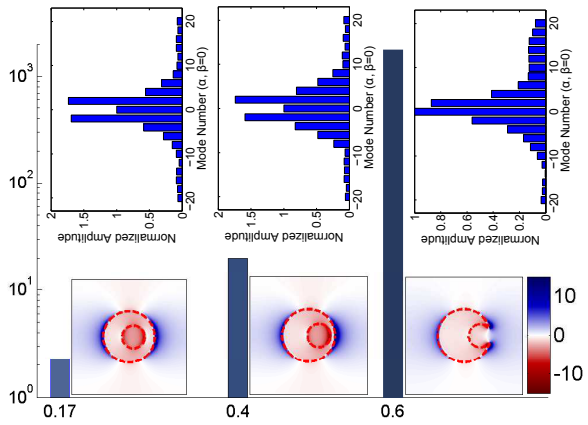

Figure 5.4: The gain in the DFG response of the graphene layer obtained by introducing asymmetric nanoparticles on top of the graphene layer. The insets shows the enhancements in the real part E_x and the normalized amplitude of spatial expansion functions for $|\alpha| = 1, 2, ..., 20$ and $\beta = 0$.

d increases (insets of Fig. 5.4). As a result, the radiated THz power is enhanced by the factors of $g^{(2)} \sim 2$, $g^{(2)} \sim 20$, and $g^{(2)} \sim 10^3$ for $d = 15$nm, $d = 35$nm, and $d = 55$nm, respectively. As to be detailed in the study of the pulse excitation, The amount of the enhancement obtained in the case of crescent nanoparticles (i.e. $d = 55$nm) leads to a substantial conversion efficiency compared to the available integrated THz photomixing technologies. It is worth mentioning that nano-crescents can be fabricated via a simple fabrication method using the electron beam lithography [55, 110]. It should be emphasized that the approach introduced here is not an absorption-enhanced process. The approach presented here relies on engineering the scattering process.

5.3.2 Pulse generation

In the analysis of THz pulse generation, we assume that the optical pulse is a Gaussian pulse with a central wavelength of $\lambda_0 = 800nm$. The electric field of the incident pulse can be written as follows:

$$\mathbf{E}(t, \mathbf{r}) = E(t) \times \mathbf{E}(\mathbf{r}) \tag{5.9}$$

where $\mathbf{E}(\mathbf{r})$ and $E(t)$ show the spatial and time dependency, respectively. The spatial distribution of electric field ($\mathbf{E}(\mathbf{r})$) is obtained from the HFSS simulations. The spatial

variation of electric field is expanded as follows:

$$\mathbf{E}(\mathbf{r}) = \sum_{\alpha,\beta} \sum_{a,b=1}^{2} \sigma_{sab}^{(2)} \left(\omega_d, \mathbf{k}_{\alpha,\beta}, \mathbf{k}_{\alpha,\beta}\right) \left(\mathcal{E}_{nm}\right)_a \left(\mathcal{E}_{nm}^*\right)_b \tag{5.10}$$

Assuming a Gaussian envelope for the laser pulse, The time-evolution of the pulse is as follows:

$$E(t) = E_0 cos(\omega t) e^{\frac{2(t-t_0)^2}{\tau^2}} \tag{5.11}$$

where t_0 is the time reference of the pulse. The Fourier expansion of $E(t)$ provides the frequency components of the incident field.

$$\begin{aligned} E(t) &= \int E(\omega) e^{j\omega t} d\omega \\ E(\omega) &= \frac{1}{2\pi} \int E(t) e^{-j\omega t} dt \end{aligned} \tag{5.12}$$

where $E(\omega)$ is the Fourier transform of $E(t)$. The total energy of a pulse can be written as follows:

$$E_p = \frac{S}{2\pi} \int_{\omega} \frac{1}{2\eta} \left|E(\omega)\right|^2 d\omega \tag{5.13}$$

where S is the surface that light shines on. The total incident power of the pulse chain is:

$$P_{inc} = \frac{S}{2\pi} \int_{\omega} \frac{1}{2\eta} \left|E(\omega)\right|^2 d\omega R_r \tag{5.14}$$

where R_r is the repetition rate of the laser pulse. The frequency components of the incident laser pulse is extended from $760nm$ to $840nm$. Since the field distribution does not significantly vary in this range, the same single frequency spatial expansion in Eq. 5.10 is used for the whole frequency range. Consequently, the following expansion can be written for the different frequency components of incident laser pulse:

$$\mathbf{E}(\omega, \mathbf{r}) = E(\omega) \sum_{m,\ n} \mathbf{E}_{\alpha\beta} e^{i\frac{2\pi}{L}\alpha x} e^{i\frac{2\pi}{W}\beta y} \tag{5.15}$$

where α and β are defined in Eq. 5.4. The total induced nonlinear current in the frequency of f_d is as follows:

$$J(f_d) = \int_{\omega} E(\omega) E^*(\omega - 2\pi f_d) d\omega \sum_{\alpha,\beta} \sum_{a,b=1}^{2} \sigma_{sab}^{(2)} \left(\omega_d, \mathbf{k}_{\alpha,\beta}, \mathbf{k}_{\alpha,\beta}\right) \left(\mathcal{E}_{nm}\right)_a \left(\mathcal{E}_{nm}^*\right)_b \tag{5.16}$$

We used the equation 5.16 to find the frequency components of $J(f_d)$. Using the inverse transform, it is possible to find the current induced in the time domain.

The center wavelength of the laser is $\lambda_0 = 800$nm; the laser generates pulses with the duration of $\tau = 150$fs and the repetition rate of 86MHz. The power lunched to the setup is assumed to be 300mW with the focused spot size of $\sim 15\mu\text{m} \times 15\mu\text{m}$. As shown in Fig. 5.5(a), the generated THz signal is captured in the silicon layer underneath. Fig. 5.5(b) shows the normalized optical pulse and the generated current on the surface of the graphene layer. The amount of THz power captured in the silicon layer has been rigorously calculated using the reciprocity theorem and it is shown that $P_{THz} \sim 1\mu$W.

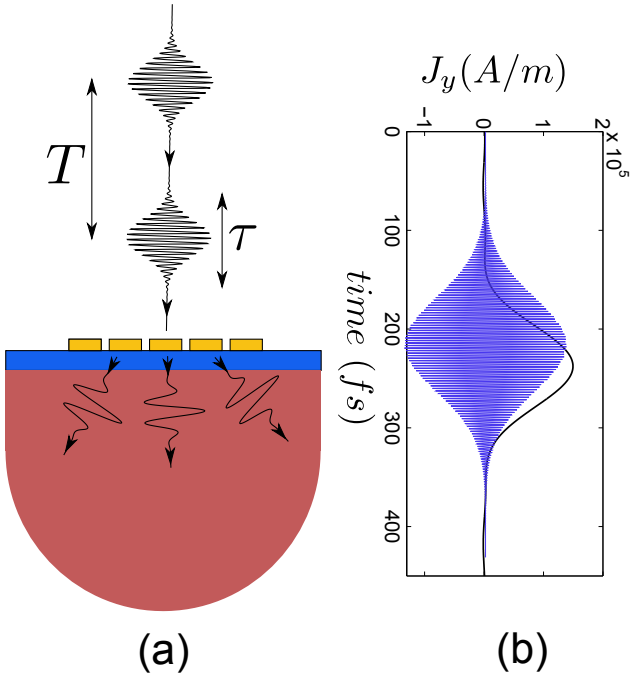

Figure 5.5: The schematic of the analyzed setup for THz pulse generation (a) and the induced nonlinear current (b) (the black Gaussian pulse). The optical excitation pulse is also shown in blue (b).

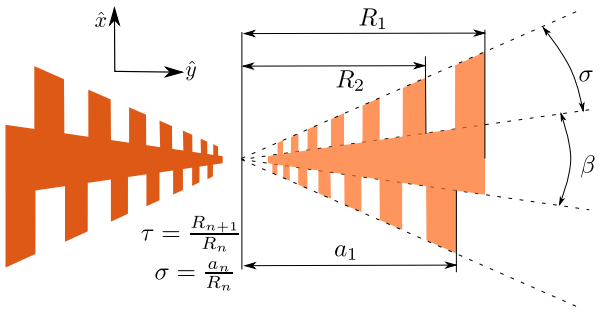

Figure 5.6: The schematic of a log-periodic antenna. The parameters τ, σ, R_1, a_1, δ, and β determines the number and the location of resonances.

5.4 Antenna Design

Antenna plays a significant role in the performance and the efficiency of a THz photomixer [111, 112]. Having a good matching between the antenna and the active region is necessary to achieve the maximum radiation power. Considering the developed model for the graphene's active region (Appendix II), the impedance of active region is directly proportional to the current density of graphene. The higher the applied current, the lower the capacitance/inductance of the active region and consequently a better matching can be achieved. Since the matching can be controlled by changing the gap properties, I focus the study to two most important parameters of antenna, maximum gain and the bandwidth. Two special types of antennas that are frequently used in the THz mixers setup are the dipole antenna and the log-periodic antenna. A dipole antenna has a high gain and low bandwidth whereas a log-periodic antenna has an exceptional bandwidth with a moderate gain. For our early designs we used a dipole antenna; however, because of the uncertainties in the frequency of maximum induced THz current, we switched to the trapezoidal log-periodic antennas. Figure 5.6 shows the schematic of a log-periodic antenna with the main parameters defining the number of resonances and the frequency of resonances. The antenna is composed of a series of dipole antennas connected together. Analytically speaking, the number of resonances is equal to the number of dipoles; the resonance frequencies can also be determined by the length of each dipole.

In the TDS measurements, a large silicon lens will be placed behind the substrate to focus the THz beam. Practically speaking, there is no reflection from the silicon lens-air interface back to the antenna. So, in a realistic modeling, the antenna should be simulated at the interface of two half-spaces of air and silicon. To model a half-space silicon layer in HFSS, a lossy silicon layer attached to the original silicon layer. Figure 5.7a shows the

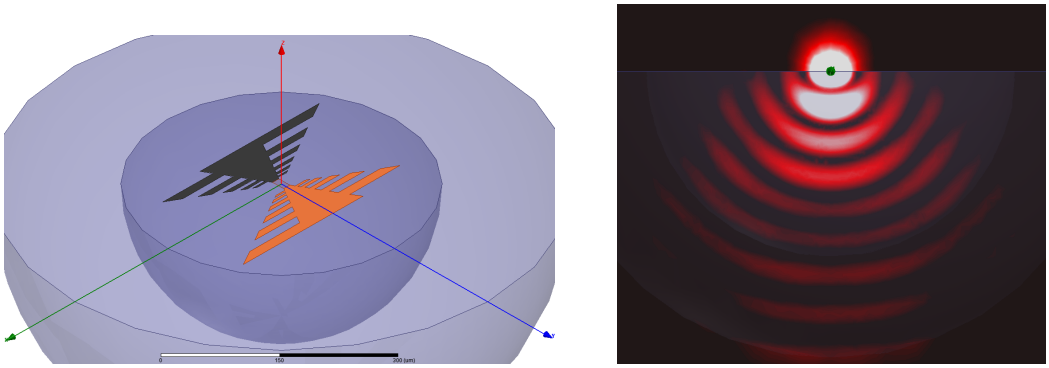

(a) (b)

Figure 5.7: The schematic of antenna plotted in HFSS (a) and the side view of the radiation from the antenna at the resonance frequency of $f = 457GHz$(b).

schematic of design in HFSS. The hemisphere near the antenna is lossless silicon and the hemisphere denoted by a lighter gray color is the lossy silicon. Since the loss is very small, the difference between the permittivity of substrates is negligible and the reflection at the interface of two layers can be ignored. The wave that propagates through the second layer eventually attenuates. The second layer in our design acts as a perfectly matched layer (PML) which mimics the behavior of a half-space substrate. Figure 5.7b shows the wave propagation in substrate. As can be seen, the wave amplitude is dominant in the lossless silicon substrate and eventually vanishes in the lossy silicon.

Two antennas are designed for the purpose of integration with graphene-based THz mixer. One of the antennas is designed to have multiple resonances from $250GHz - 1THz$ ($\beta = 60$, $\delta = 30$, $\tau = 0.7$, $\sigma = 0.84$, $R_1 = 94\mu m$) while the larger antenna has resonances down to $100GHz$ ($\beta = 60$, $\delta = 30$, $\tau = 0.7$, $\sigma = 0.84$, $R_1 = 250\mu m$). The gap size of the smaller antenna is $20\mu m$ while the gap size of the larger one is $50\mu m$. The scattering parameters for both antennas is displayed in Figure 5.8a and 5.8b. The radiation patterns are plotted in Figures 5.9a and 5.9b. In the simulations, the gap is excited by a constant current and the scattering parameters were measured at the gap interfaces. Though being the routine procedure in characterizing the antenna, a constant current model in gap is not accurate enough for modeling of the DFG induced radiation.

Since the current distribution inside the gap of antenna is not constant, a realistic model for our design has to be based on the dipolar excitation in the gap. It means that a small dipole should be located in the gap and the coupling of antenna with that dipole has to be considered. An intuitive, while not accurate, way of solving the problem of a dipole

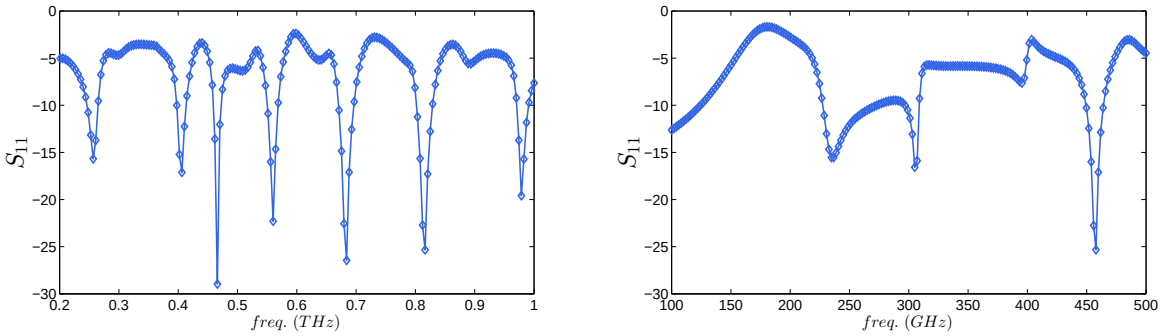

(a) (b)

Figure 5.8: The scattering parameters of two designed log-periodic antennas for the selected parameters of $\beta = 60$, $\delta = 30$, $\tau = 0.7$, $\sigma = 0.84$, $R_1 = 94\mu m$ (a) and $\beta = 60$, $\delta = 30$, $\tau = 0.7$, $\sigma = 0.84$, $R_1 = 250\mu m$ (b).

loaded antenna is to assume that the antenna would only shape the torus-like radiation pattern of the small dipole. However, the effect of antennas scattering parameters in this intuitive solution remains unanswered. Here, a full wave simulation is carried out to find the radiation of dipole in the presence of antenna.

To model the dipole loaded antenna, a small dipole antenna (the length of dipole is $l = 500nm$) with a driving current of $1A$ is located at the gap of the antenna. The size of gap is $20\mu m$ and the dipole is oriented in the direction of the log-periodic antenna (The antenna has no significant effect on the radiation of dipoles oriented perpendicular to its axis). Figure 5.10a shows the gain factor g defined as follows:

$$g_A = \frac{P_{dla}}{P_d} \tag{5.17}$$

where P_{dla} is the radiated power of the dipole loaded antenna into the silicon substrate and P_d is the radiated power of the secluded dipole in the free space. As can be seen, the antenna generally enhances the amount of the radiated power while changing the radiation patterns (Fig. 5.10b and 5.10c). The directivity of antenna as well as the enhancement depend on the dipole location. As the dipole get closer to the gap edge $d = 8\mu m$, a gain as high as 40 times can be achieved. As expected, the antenna pattern becomes asymmetric when the symmetry of excitation breaks (The dipole moves to the edges of the gap). As the number of dipoles in the gap increases, 50^2 dipoles for the designed nanostructure with the periodicity of $400nm$, the average enhancement becomes considerable. To find the effect

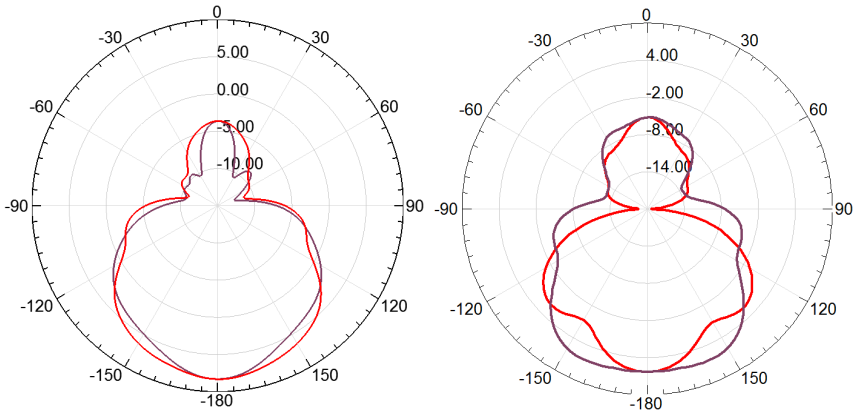

(a) (b)

Figure 5.9: The directivity of the log periodic antennas at the frequencies of $f = 981GHz$ ($R_1 = 94\mu m$) (a) and $f = 457GHz$ ($R_1 = 250\mu m$)

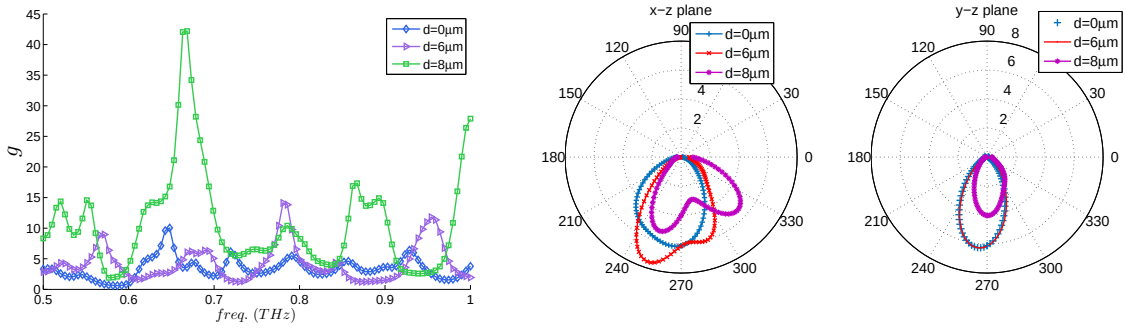

(a) (b) (c)

Figure 5.10: Defined gain factor g (Eq. 5.17)(a), the directivity of radiations in $x-z$ (b) and $y-z$ planes (c) for the small log-periodic antenna.

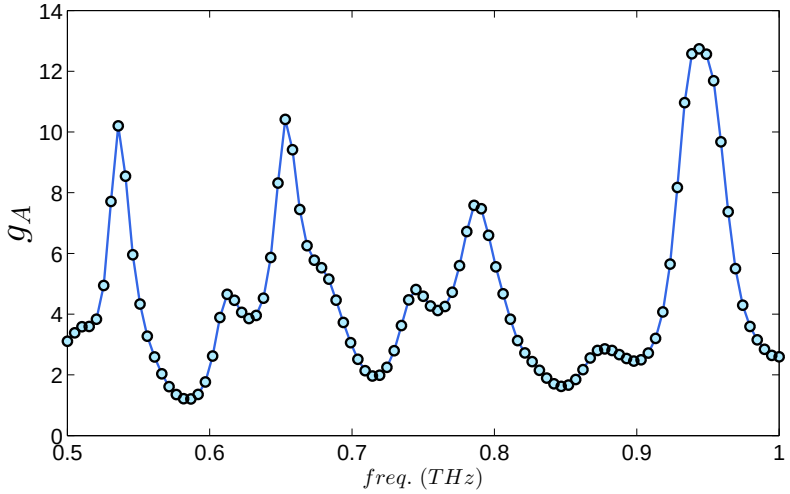

Figure 5.11: The total enhancement of the antenna ($R_1 = 94\mu m$) for a periodic structure of 16 dipole antennas.

of periodic dipole antennas in the gap, we simulated the antenna when loaded with 16 dipoles in the gap. The result (Figure 5.11) shows that the overall enhancement of $g_A = 10$ is obtained. So, the antenna affects the radiation pattern of dipole while enhancing the total radiated power. Our designed antenna shows a maximum enhancement of $g_A = 10$. To find the total radiated power, we multiply the total radiated power of dipoles by the antenna gain reported in Figure 5.11.

5.5 The proposed graphene-based photomixer

To exploit the functionality of the graphene layer in a THz photomixer application, I propose the design shown in Figure 5.12. The proposed structure is composed of a log-periodic antenna (Figure 5.12 (a) and (b)) connected to large pads for the connection of the chip to biasing sources (Figure 5.12(a)), a periodic nanostructure to enhance the light-graphene interaction (Figure 5.12(c)), and a top gate to control the carrier density in graphene (Figure 5.12(d)).

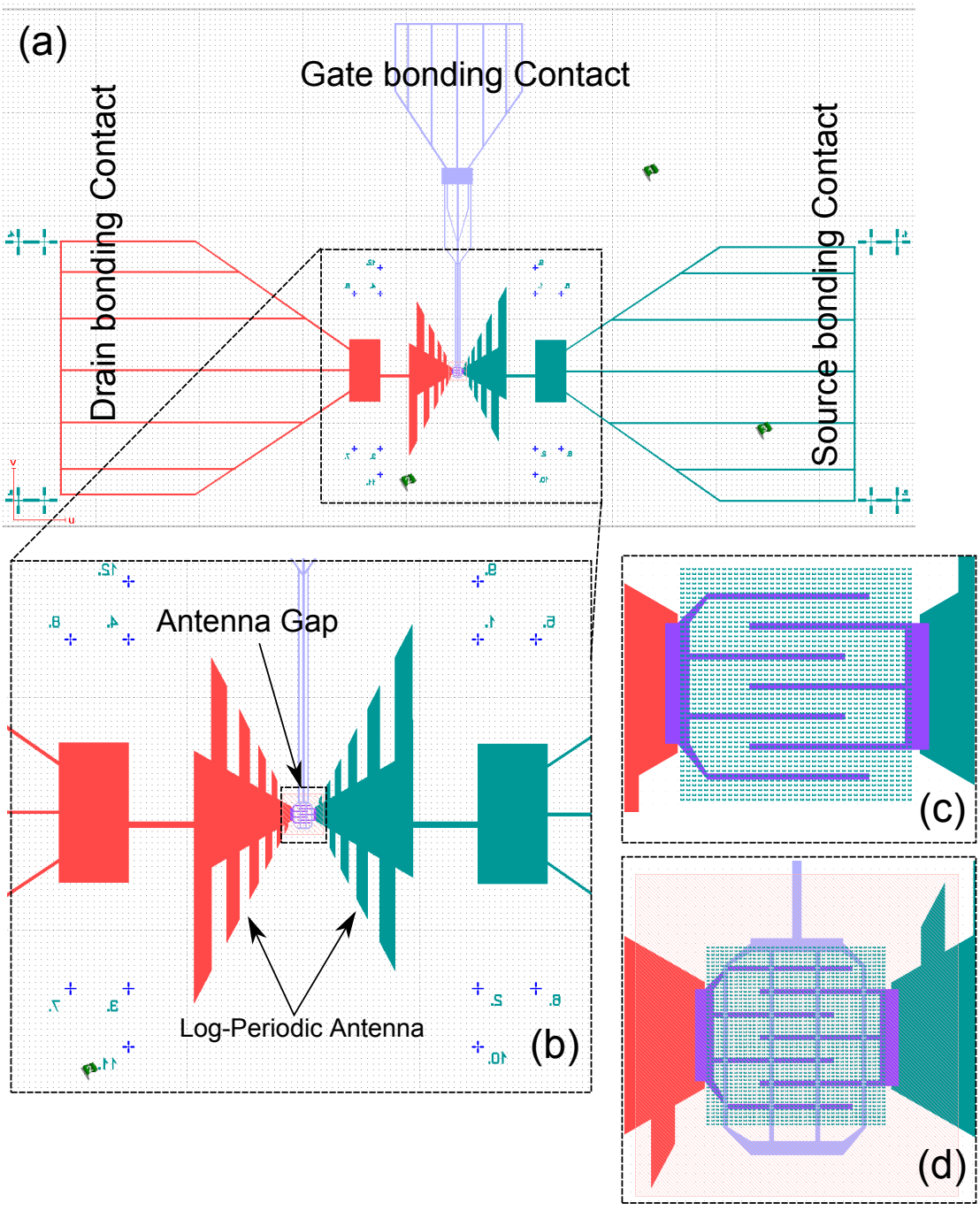

Figure 5.12: (a) The schematic of the proposed photomixer. The bonding contacts facilitate the connection of the chip to a designed PCB board. A magnified picture of designed antenna and the gap size are shown in (b), (c), and (d). The plot in (c) shows the first layer of the design including the drain/source contacts and the nanoparticles in the gap. The plot in (d) demonstrates the gate dielectric and the top gate of the graphene layer.

5.6 Conclusion

In conclusion, we assessed the attainable THz power from the proposed structure. Considering the contribution of the drag effect and taking into account the plasmonic and antenna enhancements, it is possible to obtain more than $10\mu W$ of THz power resulting to the conversion efficiency of $3e-5$.

Chapter 6

Fabrication of graphene-based THz photomixer and the measurement results

The fabrication approach discussed in Chapter 2 is based on the fabrication of nanostructures and then transferring graphene to the wafer. In the proposed approach the existence of a reflective metallic surface below the nano-structure is essential for achieving high local enhancement in the electric field. Although the proposed method offers unprecedented high enhancements, the approach has certain drawbacks that limits its use for our application. The first drawback is the existence of a metallic surface at a close distance to the graphene layer. As known from the image theory, the existence of this layer near the graphene layer suppresses the THz radiations. Another drawback, which simply arises from transferring graphene onto the nano-structure, is the uncontrollable distance between the graphene layer and the nano-structure. As discussed in Chapter 2, this distance plays an important role in the enhancement. Finally, the fabrication process is not optimized in the sense that the fabrication of the whole mixer structure needs at least three steps of electron beam lithography (EBL) including fabrication of the back-gate, nano-antennas, and the THz antenna.

A better approach that was theoretically discussed in chapter 5 is to transfer the graphene layer onto the substrate and then build the nano-antennas and the THz antenna on top of the graphene layer. The SiO_2/Si interface has the role of an optical reflector while it does not affect the THz radiation. Using this approach, the fabrication process can be minimized to a one step EBL process. In addition, the problems that we previously

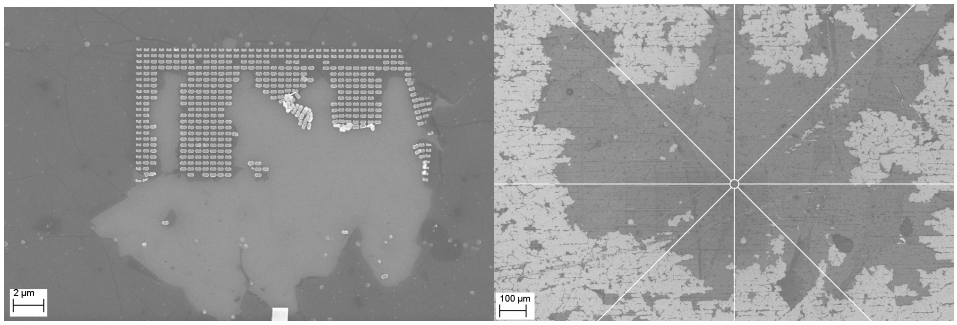

(a) (b)

Figure 6.1: Destruction of nanoparticle as a result of the graphene layer detachment for the surface of substrate (b). The effect of Remover PG on the graphene layer (b).

encountered such as the deterioration of nano-antennas and the indefinite distance between the graphene and the nano-antennas are resolved.

Although the one step nano-EBL process on graphene might seems trivial, there are challenges that requires the development of an elaborate recipe for the large area graphene devices. The main difficulty arises from the fact that the bonding of graphene-substrate is based on the weak Van Der Waals forces. The weak attachment prevents the facilitation of the lift-off process using the ultrasonic or high temperatures. The best that can be done for the lift-off is to use the liquid pressure of a pipette to complete the lift-off process. Surprisingly, the liquid pressure proves to also be a damaging factor. Furthermore, the graphene layer interacts with Remover PG and starts to roll over itself or be detached from the SiO_2 layer. Figure 6.1a shows how the nano-structure is affected as a result of graphene detachment. The metallic structure on the graphene layer only has chemical bonds with the graphene layer meaning that there is no bonding between the metallic layer and the substrate beneath. The effect of Remover PG on graphene is shown on Fig. 6.1b. The graphene layer is removed and only a few islands are remained on the substrate.

After trying different approaches, we developed a reliable and repeatable recipe that can be used for fabrication of a wide variety of graphene-based devices. The fabrication steps are summarized as follows:

- Growing the SiO_2 layer on the silicon substrate.
- Transferring the graphene layer.
- Spin coating PMMA A3 with the speed $2000rpm$ and the acceleration $500rpm/s$.

- Baking the PMMA layer on hot plate at the temperature of 180° for about 17 minutes.
- Drain and source pattern development.
- Oxygen plasma for 20 seconds.
- Defining graphene contacts.
- Depositing Ti/Au layer.
- Gate dielectric fabrication.
- Oxygen plasma for 20 seconds.
- Gate contacts definition.
- Bonding the sample to a PCB board.
- Packaging the sample.

Here, we explain the details of each step.

6.1 Sample preparation: SiO_2 layer growth and graphene transfer

The high resistive silicon wafers were cleaned using the ultrasonic bath of acetone and IPA. We then used the plasma enhanced chemical vapor deposition (PECVD) to deposit $300nm$ of glass on top of the silicon wafers. The Filmetric measurements of the thickness show a uniform deposition ranging from $300nm$ to $320nm$ over the whole sample. We then transfer the prepared CVD graphene layer with the method explained in Chapter 2. To make sure that the graphene layer is attached to the silicon wafer, running the following recipe is necessary:

- Soft baking for 30 minutes at 50° followed by another 30 minutes at 100°.
- Baking sample for another 30 minutes at 200°.
- Cooling the sample and soaking it in acetone over night.

After this stage, the pure graphene layer over the silicon substrate is obtained.

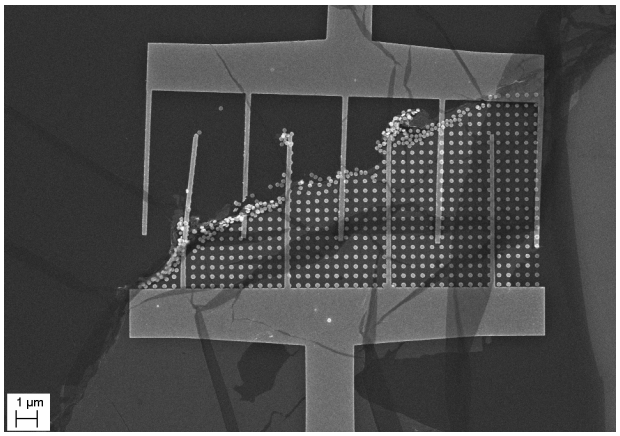

Figure 6.2: The change in the graphene layer after the lift-off process. The graphene layer is moved causing one of the contact to be tilted. The nanostructure is also deteriorated as a result of graphene layer detachment.

6.2 Fabrication of THz antenna and the drain/source metal contacts

One straightforward method of fabrication is to pattern the whole antenna and contacts in one step and then deposit the gold film. This approach, however, is not reliable and repeatable as there are cracks in the transferred graphene layer that would completely deteriorate the structure after one step or two steps of EBL. Figure 6.2 shows the changes in the graphene layer caused by the lift-off process. The best recipe that we developed is as follows:

- Using EBL ($20Kv/20\mu m$) to define the THz antennas and the bonding pads.
- Developing the sample in MIBK:IPA 1:3 for 30s followed by 30s rinsing in IPA.
- Running 20 seconds oxygen plasma to erase the graphene below the antenna and the pads.
- Returning the sample to the Raith TWO for another round of EBL. After proper alignments, defining the graphene contacts and the nano-structure.
- Developing the sample again in MIBK:IPA 1:3 for 30s followed by 30s rinsing in IPA.
- Depositing Ti/Au (3nm/65nm) using the electron beam deposition.

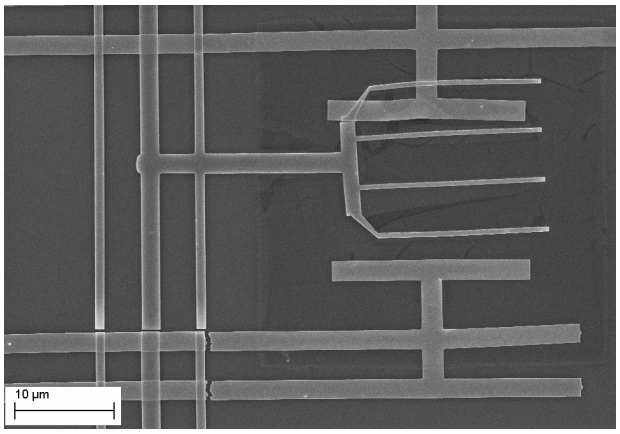

Figure 6.3: The discontinuity in the first and the second layers as a result of the fabrication of the second layer over the loosely substrate-attached first layer.

- Soaking the sample in acetone over night. Then facilitating the lift-off process with a pipette. It is also possible to use ultrasonic bath for a short time to facilitate the lift-off.

As a result of this step, the THz antenna would be attached to the silicon layer and the graphene located in the gap will also be attached to these antennas. Since the bonding between Ti/SiO_2 is much stronger than the $Ti/graphene$, the proposed fabrication step is far more reliable than the simple one-step EBL method.

This approach would also ease the next fabrication steps since one should not be worry of the pressure of higher layers to the lower ones. If all the structures in the first layer are fabricated on graphene, there is a good chance that the tension of the second layer would destroy the connections of the first layer (Fig. 6.3). Figure 6.4a and its zoomed views (Fig. 6.4b and 6.4c) show a large area of periodic digitated structure fabricated using the proposed approach.

6.3 Fabrication of the gate

One of the most important parts of a graphene-based device is the gate. By changing the gate voltage, it is possible to change the Fermi level of graphene. Changing the Fermi level results in a change in the carrier density on the graphene layer and consequently all the electronic properties of graphene including the nonlinearity can be controlled. In most of

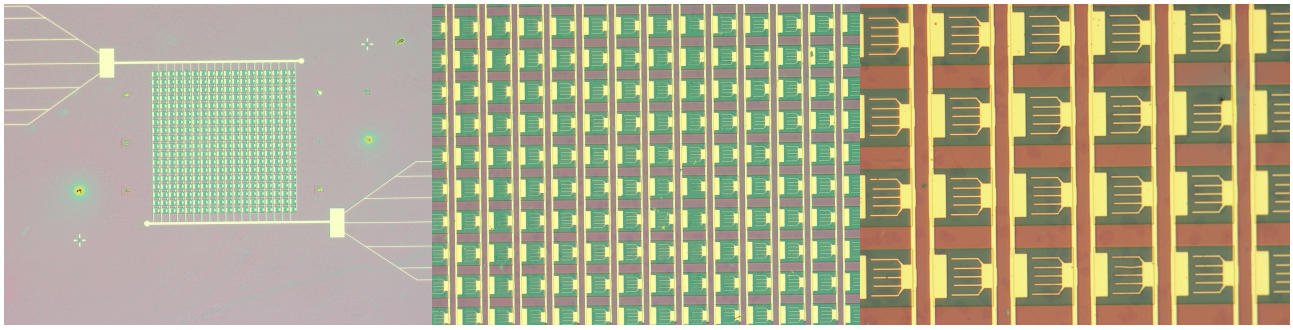

(a) (b) (c)

Figure 6.4: A large area array of digitated structures on top of graphene (a). The figures (b) and (c) show the zoomed view of part (a).

the literature, the concept of backgating (as explained in Chapter 1) is used to control the Fermi level of graphene. This approach, however, would need the deposition of metal on the lower side of Si wafer which blocks the THz radiation. Instead, we are using a top-gate design shown in Fig. 6.5. Figure 6.5a shows the perspective view of the gate structure. The schematic of the designed layered structure in RaithTWO software is also shown in Fig. 6.5b.

The fabrication of gate structure includes two steps EBL processes, deposition of gate dielectric and deposition of the gate metal contact. The process recipe can be summarized as follows:

- Spin-coating PMMA A3 with the speed $2000rpm$ and the acceleration $500rpm/s$.
- Baking the PMMA layer on hot plate at the temperature of 180° for about 17 minutes.
- Patterning the gate dielectric using EBL.
- Deposition of $90nm$ of Al_2O_3 and then lift-off overnight using the Remover PG.
- Running 20 seconds oxygen plasma to erase the graphene except the parts located below the gate dielectrics.
- Spin-coating PMMA A3 ($2000rpm$ and $500rpm/s$) and baking for 5 minutes at 180°.
- Spin-coating another layer of PMMA A3 ($2000rpm$ and $500rpm/s$) and baking for 15 minutes at 180°.

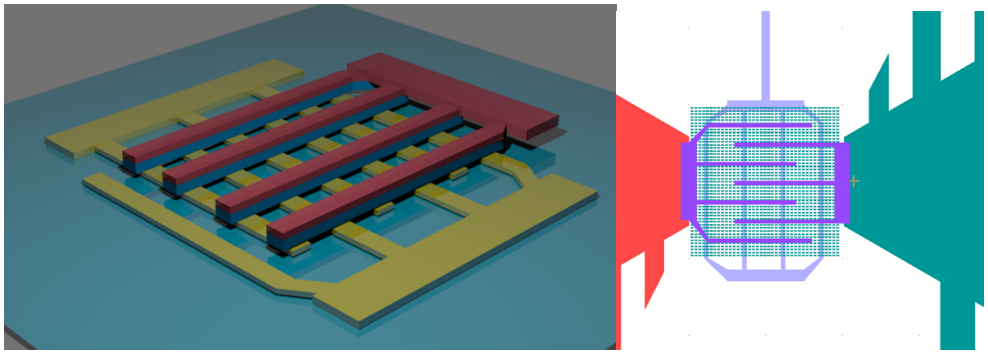

(a) (b)

Figure 6.5: The schematic of a top-gated graphene structure (a). The first layer is the drain and the source contacts, the middle layer is Al_2O_3, and the top layer is the gate metal contact. Plot (b) demonstrates the schematic of different layers including the THz antenna, the drain and the source contacts, and the gate metal contact.

- Patterning the gate metal contact using EBL.
- Deposition of $90nm$ of Ti/Au and then lift-off overnight using the Remover PG.

In is important to note that a part of the gate metal contact is on the gate's dielectric while the rest of the gate metal contact is on the Si wafer. Since the dielectric is at the hight of $90nm$ from the Si wafer, the height of gate metal contact should be at least 90nm. Figures 6.6a shows the SEM picture of the fabricated THz photomixer antenna. Figure 6.6b shows the zoomed picture of the gap highlighting that there is no nanostructure in the gap of antenna and a part of gate metal contact did not lift-up properly. Figure 6.7a shows the SEM image of a sample with the nanoparticles in the gap of the antenna. A fabrication tolerance as good as $5nm$ is achieved using the EBL.

During the course of this work, different recipes have been developed for the fabrication of THz mixing structures. In addition to the devices that are fabricated with the recipe explained in this chapter (Recipe 1), I also fabricated smaples using the simple EBL method without removing the graphene layer below the antennas (Recipe 2). The fabrication steps of Recipe 2 are summarized as follows:

- Transferring graphene using the method explained in this chapter.
- Spin coating sample with PMMA A3. The speed and the acceleration are $2000rpm$ and $500rpm/s$, respectively.

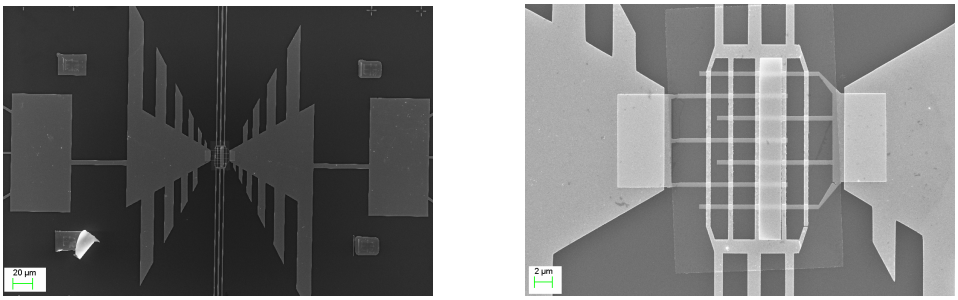

(a) (b)

Figure 6.6: (a) The fabricated THz photoconductive antenna on the graphene layer including the drain/source, gate dielectric, and the gate metal contact. (b) The zoomed view of the antenna gap.

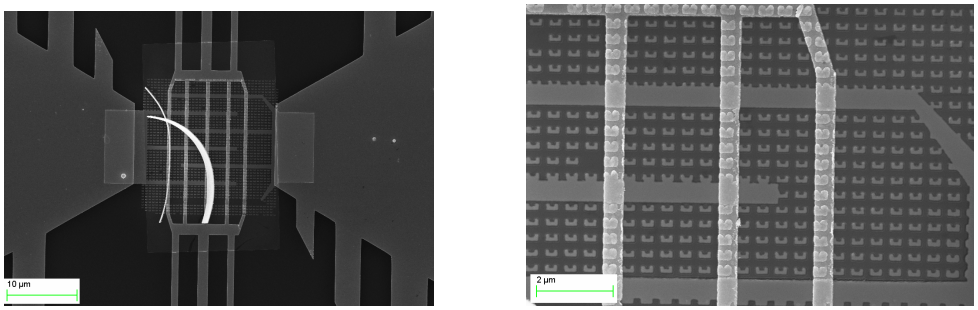

(a) (b)

Figure 6.7: (a) The fabricated THz photoconductive antenna on the graphene layer including the drain/source, nanoparticles, gate dielectric, and the gate metal contact. (b) The zoomed view of the nanoparticles in the antenna gap.

- Patterning the antenna structure using EBL and then depositing Au/Ti layer.
- Soaking the sample in Remover PG or acetone to complete the lift-off process.
- Spin coating the sample using PMMA A3. The process was repeated twice to achieve $400nm$ PMMA A3 on top of the graphene.
- Patterning the gate contact, depositing the $Al_2O_3/Ti/Au$ ($90nm/3nm/45nm$) layer, and then lifting-off the sample.
- Spin coating the negative resist (Ma-N 2400), patterning with the EBL.
- Removing the graphene layer using $20-40$ seconds of oxygen plasma.
- Dissolving the negative resist in acetone over night.

Figure 6.8a and its zoomed view show the dipole antenna with the decoupling THz structure fabricated with one step EBL method (Recipe 2). The graphene layer is then patterned using a negative resist layer. Figures 6.8c and 6.8d are also the gated designs of log periodic antenna fabricated using the Recipe 2.

6.4 Bonding and Packaging

To characterize our designed structure two different DC biasing sources are required. A source to control the DC current on the graphene layer and another source to control the gate voltage of graphene. To connect the designed chip to the external sources, the chip should be bonded to a PCB board. I have designed the PCB boards in ADS. The fabrications of PCB boards are done with the assistance of one of my colleague, Mr. Hussam Alsaedi, using the milling machine. At the start of this project, we were also using the PCB boards provided by TeTechS Inc.

Since the thickness of gold layer in our designs is less than $100nm$, we could not use the bonding machine. Instead, I used the silver epoxy to connect the chip to the PCB board. The process involves gluing the PCB board to the fabricated THz mixer using the UV cure epoxy and then connecting the drain, source, and gate metal contacts on the chip to the PCB conducting layer with silver epoxy. Though the process is completely manual, it is possible to bond the features as small as $100\mu m \times 100\mu m$ to the PCB board. Figure 6.9a shows the designed PCB board and Fig. 6.9b shows the microscope picture of the sample bonded using the silver epoxy. The prepared sample is then placed in the right packaging

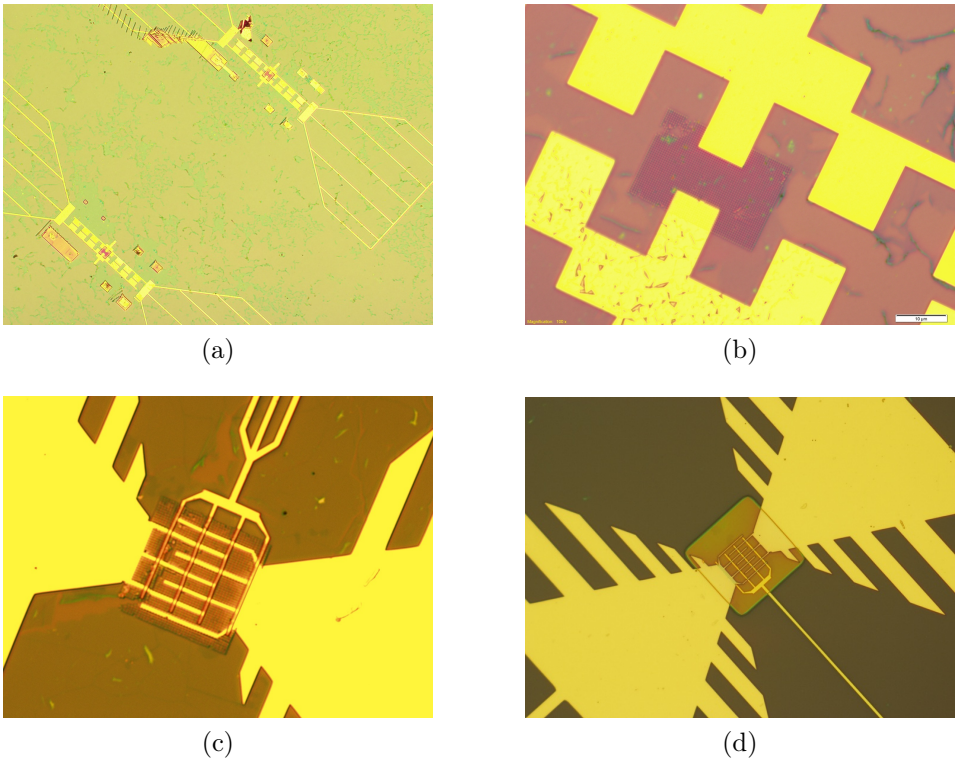

(a) (b)

(c) (d)

Figure 6.8: The structure of dipole antenna with THz decoupling structure (a) and the zoomed view of the gap of the dipole antenna. (c) and (d) are the fabricated log periodic antenna design with and without the nanostructure, respectively.

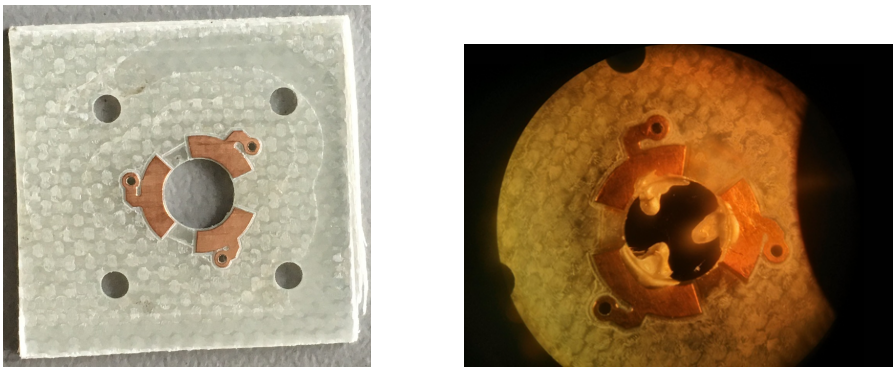

(a) (b)

Figure 6.9: (a) The designed PCB board for the sample bonding and packaging. (b) The microscope image of the bonded THz photomixer chip using the silver epoxy.

for the measurements. The package we used for our sample was provided by TeTechS Inc (Fig. 6.10a). The final product of the packaging and assembly is the chip that is placed on a x-y moving stage (Fig. 6.10b).

6.5 Measurement setups

The first stage of characterizing the fabricated THz mixer is to measure the induced photocurrent in the gap region. The amount of this photocurrent is a direct indicator of the attainable THz signal. Figure 6.11 shows the schematic of the setup. The laser pulse is focused on the gap of photoconductive antenna with an optical lens. The low noise amplifier (LNA) provides the bias voltage and amplifies the amount of the induced photocurrent. The lock-in amplifier measures the induced photocurrent signal that has the frequency of chopper (ω_{chop}) and suppresses the other sources of noise that does not have the frequency of ω_{chop}. Next step of characterization is the measurement of the generated THz signal.

The characterization of fabricated THz mixer is done using the terahertz time domain spectroscopy (TDS) setup. Figure 6.12(a) shows the typical setup of a TDS setup. The main purpose of the setup is to study the THz pulse generator which is driven by a DC bias and is excited by a femto-second pulsed laser. The produced THz pulse is directed and focused on the receiver which is already excited by the laser's pulse. Having both pulses, the laser's pulse and the THz pulse, arriving at the same time in the GaAs receiver, a current with the frequency of ω_{chop} is induced that can be sensed by the detector. The

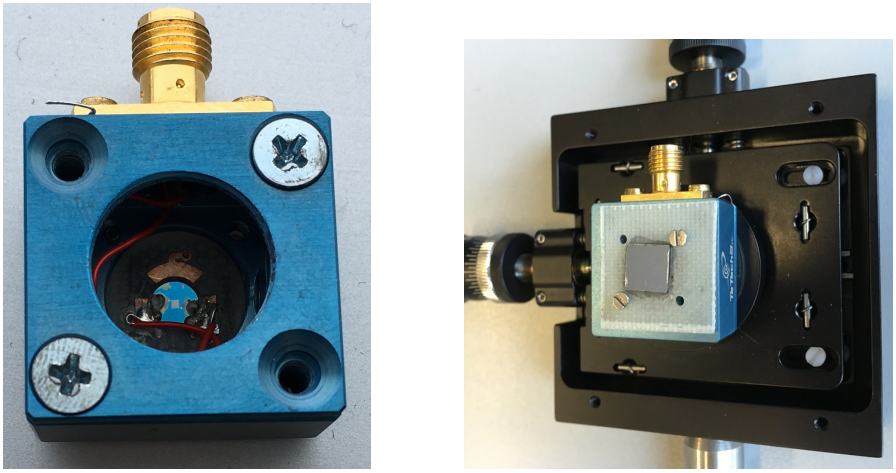

(a) (b)

Figure 6.10: The packaging of the bonded sample (a) and the packaged sample on the x-y moving stage.

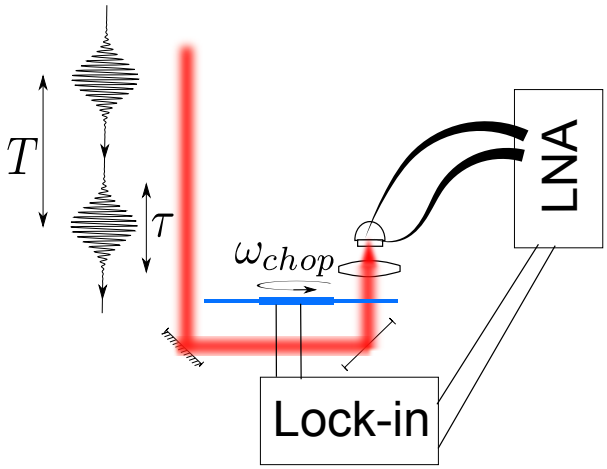

Figure 6.11: The schematic of setup used for measuring the photocurrent.

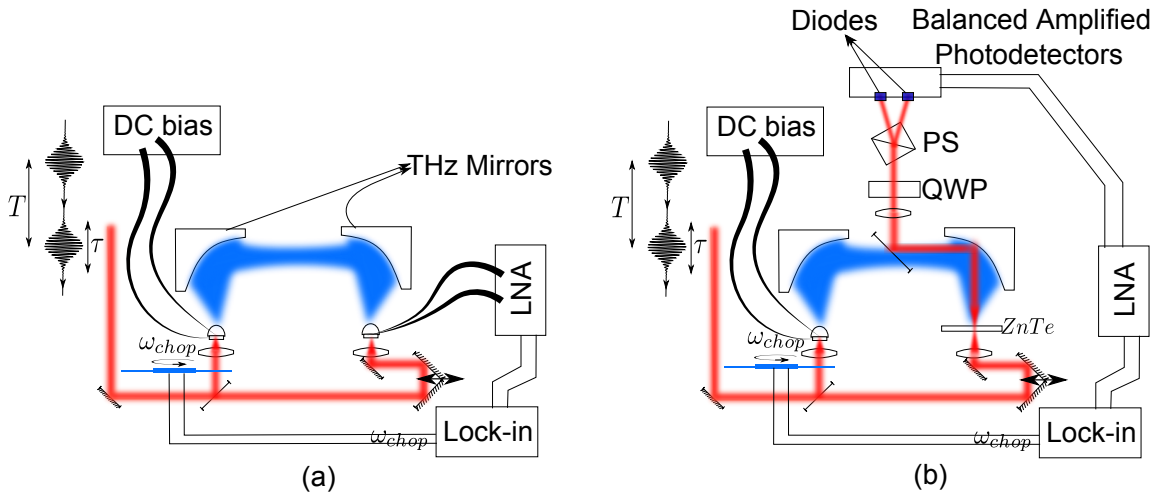

Figure 6.12: (a) The schematic of THz measurement setup using a GaAs photoconductive antenna. (b) The THz measurement setup using an electro-optical crystal (ZnTe).

synchronization of pulses can be done using the moving stage that increases or decreases the path of the incident laser light. Two infrared lenses are used to focus the laser beams on the THz generator and the detector. The existence of lenses can help to enhancing the received signal by at least $10dB$. There are also two silicon lenses attached to the generator and the detector. The existence of these THz lenses are also mandatory since the generated THz beam in the small gap of antenna is very divergent. Depending on the shape of the lens, the THz beam can be collimated (Bullet lenses) or focused (Hypo-hemispherical lenses) or the divergence angle can be decreased (Hyper-hemispherical lenses). For the setup that we are using in our lab, a high resistive hyper-hemispherical lenses with the diameter of $R = 10mm$ and the thickness of $t = 5.84mm$ is used.

Another setup that is frequently used to characterize the generated THz pulse is shown in Fig. 6.12(b). Instead of a THz photo-conductive antenna as the detector, an electro-optic crystal ($ZnTe$ crystal) is used for the detection. Because of the nonlinearity of the crystal, the polarization of the laser beam passing through the crystal rotates when both THz signal and the laser beam is getting mixed inside the crystal. The amount of this rotation is directly proportional to the electro-optic (EO) coefficient of crystal. It can be shown that the change in the polarization angle is as follows [113]:

$$\Delta\phi = \frac{\omega L}{c} n_O^3 r_{41} E_{THz} \tag{6.1}$$

where n_O is the refractive index at the optical frequency and r_{41} is the EO coefficient.

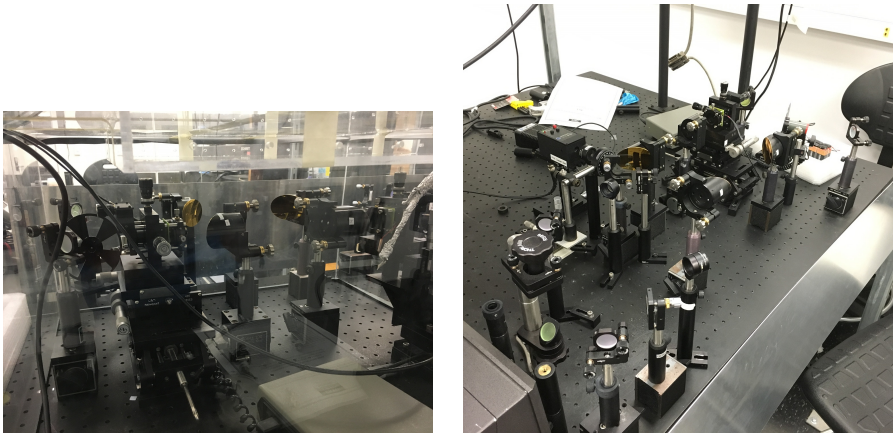

(a) (b)

Figure 6.13: The GaAs (a) and the ZnTe (b) THz characterization setups.

To detect the amount of polarization rotation in the laser beam, we are using the setup shown in Fig. 6.12(b). The detection part is composed of an splitter, a quarter waveplate (QWP), a polarization dependent splitter (PS), and a balanced amplified photodetector. In the absence of THz beam, the beam polarization rotates 45° by the QWP and splits equally in the PS. The balanced detector, in the absence of THz wave, detect zero since both received signals on the photodetectors have the same amplitude. In the presence of THz signal, a small rotation in the polarization unbalances the detector causing a large signal to be observed. To observe a signal higher than the noise floor, the power of incident signal on the ZnTe crystal should be very high.

6.6 Measurement results

To do the final measurements, I and a few of my colleagues, Mr. Chao from prof. Dayan Ban lab (ZnTe setup) and Mr. Zandieh and Dr. Saeedkia from the TeTechs Inc. (GaAs setup), made the characterization setups. A picture of the setups are shown in Fig. 6.13.

The measured photocurrent for two THz photoconductive antennas of Fig. 6.8d, and 6.8a are shown in Figures 6.14 and 6.15. The first antenna (Fig. 6.8d) is a gated antenna fabricated using the Recipe 2. As a result of the fabrication method, there is a thick layer of negative resist on the graphene layer. A large amount of photocurrent near $30\mu A$ is obtained for $V_{DS} = 250mV$ and the gate voltage of nearly $5V$. As can be seen in 6.14(b),

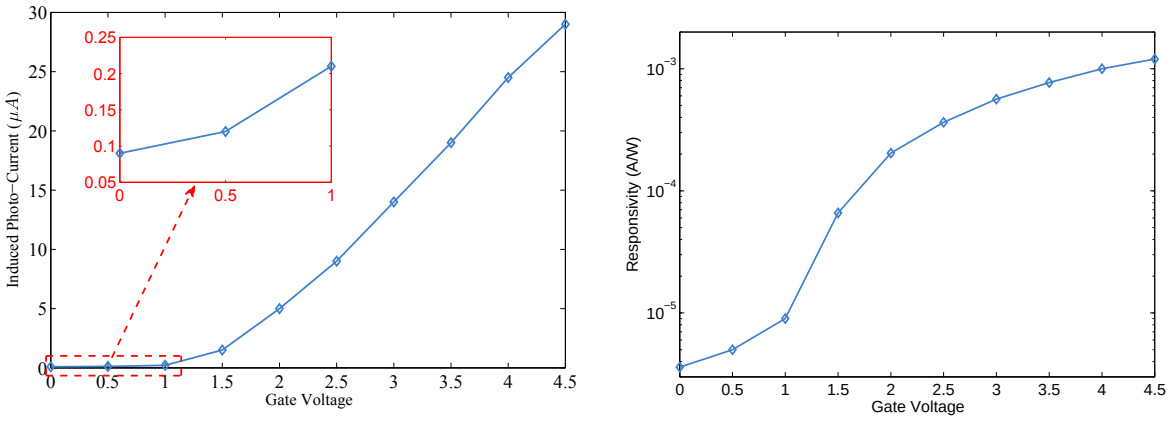

(a) (b)

Figure 6.14: The measured photocurrent (a) and the responsivity (b) of the fabricated antenna of Fig. 6.8d as a function of the gate voltage. The incident power is $25mW$ and $V_{DS} = 250mV$. The inset shows the enlarged plot of the region marked with the red dashed rectangle.

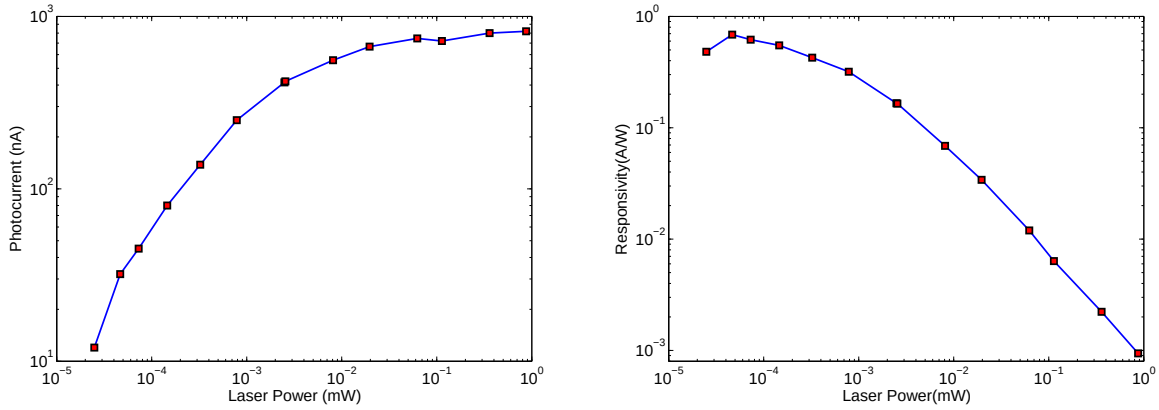

(a) (b)

Figure 6.15: The measured photocurrent (a) and the responsivity (b) of the fabricated antenna of Fig. 6.8a as a function of the incident wave power ($V_{DS} = 200mV$).

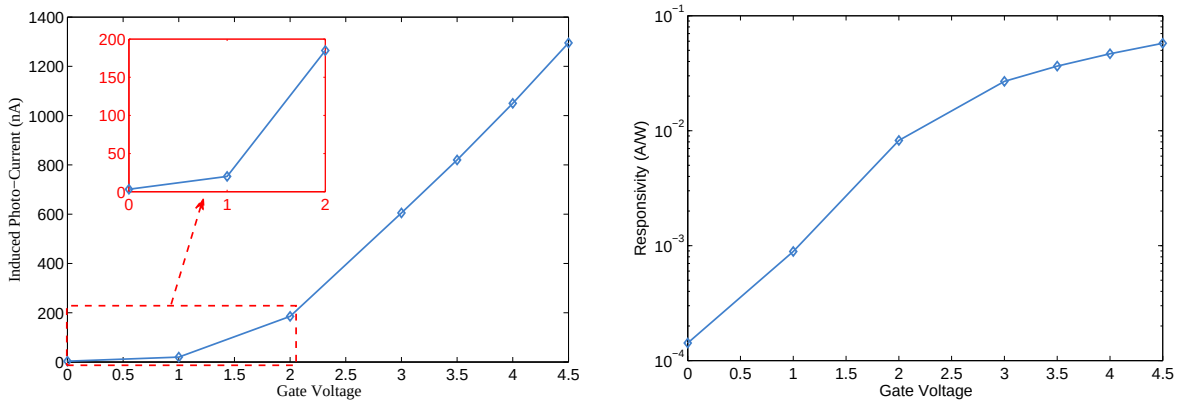

(a) (b)

Figure 6.16: The measured photocurrent (a) and the responsivity (b) of the fabricated antenna of Fig. 6.8d as a function of the gate voltage. The incident power is $22.5\mu W$ and $V_{DS} = 250mV$. The inset shows the enlarged plot of the region marked with the red dashed rectangle.

the responsivity of the fabricated antenna is directly proportional to the gate voltage. It is worth mentioning that the photocurrent is also linearly proportional to the V_{Ds}. As V_{DS} increases, the photocurrent increases; however, because of the limited amount of current supported in graphene this voltage can not exceed a certain value. We chose $V_{DS} = 250mV$ to be on the safe side.

Figure 6.16a shows the photocurrent measurements for the same device and for the incident power of $22.5\mu W$. The maximum photocurrent of $1.4\mu A$ is obtained for the gate voltage of $4.5V$. As the incident power decreases from $25mW$ to $22.5\mu W$, the amount of induced current dramatically decreases; however, the responsivity increases by two orders of magnitude (6.16b).

We also investigated the role of source and drain metal contacts in the photocurrent measurements. For an antenna with two different contacts on each side, Cr/Au for one arm of the antenna and Ti/Au for the other arm (the device is similar to Figure 6.8a without any nanostructure in the gap), a sensitivity as high as $0.5A/W$ is obtained. The device is fabricated without the gate layer. Figure 6.15a and 6.15b show the induced photocurrent and the responsivity as a function of incident power at $\lambda_0 = 800nm$ ($V_{DS} = 200mV$). This device is fabricated using the Recipe 2 where the thickness of negative resist is less than $50nm$. The high amount of recorded photocurrent which requires the quantum efficiency

of one or even more can be associated with the charge trapping in the negative resist or the multiple hot-carrier generation [114]. The exact origin of this high quantum yield needs more theoretical and practical investigations.

The other fabricated devices without nanoparticles in the gap and with an Al_2O_3 gate dielectric produce a maximum photocurrent less than $2\mu A$. The reason for a high amount of photocurrent for the sample of Fig. 6.8d might be because of the thick resist layer that changes the graphene's Fermi level. An elaborate and accurate conclusion about these effects would require the THz measurements.

Chapter 7

Afterword

In summary, a graphene-based THz photomixer is proposed, thoroughly studied and analyzed in theory and successfully fabricated with a developed recipe, and characterized with the photocurrent measurements. Both theoretical results and practical measurements corroborate the fact that the graphene layer can be considered as an outstanding candidate for the photomixing applications.

In Chapter 2, the idea of using a plasmonic nanostructure for the enhancement of light-graphene interaction is introduced and tested through Raman Spectroscopy. The measurements show the significant effect of designed nanoparticles on enhancing a nonlinear process such as the Raman scattering. In Chapter 3, a comprehensive theoretical model for modeling of the difference frequency generation (DFG) in graphene is proposed. The role of DC biasing and the wave momentum as two practical mechanisms in the DFG process are investigated. Chapter 4 presents a computationally efficient numerical electromagnetic method for analysis of scattering from the graphene flakes. A multipole-based approach with a surface boundary condition (SBC) is deployed to analyze the wave interaction with graphene and also to verify the volumetric model of graphene.

In Chapter 5, the obtained nonlinearity in conjunction with the volumetric model is used to design and analyze the proposed photomixing structure in the perturbation limit. The nonlinear analysis shows the achievable THz power of $1\mu W$ from an incident laser pulse with the fluence of $15mW/cm^2$ without applying any DC current. The role of antenna in the bandwidth and the power of THz radiation is also examined. Outcome of the theoretical study asserts that a THz signal as powerful as $10\mu W$ can be generated using a single sheet of graphene.

In Chapter 6, a new recipe for the fabrication of the graphene-based photomixer struc-

ture is proposed. The developed recipe ensures a reliable and a repeatable fabrication process even for large area graphene devices. Lastly, the measurement setup and the measurement results are shown.

7.1 Future Work and Outlook

The main future work that can be envisioned is the THz measurements missing in the presented thesis. The effect of incident laser power, the shape of nanoparticles, and the antenna effect on the bandwidth and the shape of THz pulse will be further studies and explored.

Though it is almost ten years since the discovery of graphene, there are lots of new research directions that can help the implementation of the designed photomixer structure. One of these directions is the production of a stack of graphene layers. At the time of this report, the stack of graphene layers up to 40 layers has been produced. This huge number of graphene layers can be used particularly in the DFG. Based on the amount of power that we obtained in a non-absorptive (plasmon-drag) enhancement, it is believed that powerful THz signals can be generated with the stack of graphene layers.

Another direction that can excite new researches on the graphene-based photomixing structure is the integration of graphene with low-loss silicon waveguides. The graphene layer can be easily transferred onto the silicon where a platform for low-loss THz signal transmission and radiation already exists. This approach would facilitate and help not only nourishing the research on graphene-based photomixers but also the THz technology as a whole.

7.2 Conclusion

In conclusion, the proposed graphene-based THz mixer offers unique characteristics that makes it suitable for a wide range of application in THz range of frequency. The achievable power of $1\mu W$ with the bandwidth of 10THz ensures that device covers the whole THz gap spectrum. The proposed device can be fabricated with a modular and systematic fabrication recipe which strengthen its applicability in different structures such as in a radiating or a waveguiding structure. The measurements strongly support the fact that the proposed device is capable of producing a THz power comparable with those of the commercially available THz mixers.

Bibliography

[1] G. W. Semenoff, "Condensed-matter simulation of a three-dimensional anomaly," *Phys. Rev. Lett.*, vol. 53, pp. 2449–2452, Dec 1984.

[2] e. a. Sheneve Z. Butler, "Progress, challenges, and opportunities in two-dimensional materials beyond graphene," *ACS Nano*, vol. 7, no. 4, pp. 2898–2926, 2013. PMID: 23464873.

[3] B. Radisavljevic, A. Radenovic, J. Brivio, V. Giacometti, and A. Kis, "Single-layer mos2 transistors," *Nature nanotechnology*, vol. 6, no. 3, pp. 147–150, 2011.

[4] E. Bianco, S. Butler, S. Jiang, O. D. Restrepo, W. Windl, and J. E. Goldberger, "Stability and exfoliation of germanane: A germanium graphane analogue," *ACS Nano*, vol. 7, no. 5, pp. 4414–4421, 2013. PMID: 23506286.

[5] F. Schwierz, "Graphene transistors," *Nature nanotechnology*, vol. 5, no. 7, pp. 487–496, 2010.

[6] X. D. Li, S. Q. Wu, and Z. Z. Zhu, "Band gap control and transformation of monolayer-mos2-based hetero-bilayers," *J. Mater. Chem. C*, vol. 3, pp. 9403–9411, 2015.

[7] D. Akinwande, N. Petrone, and J. Hone, "Two-dimensional flexible nanoelectronics," *Nature communications*, vol. 5, 2014.

[8] A. K. Geim and K. S. Novoselov, "The rise of graphene," *Nature materials*, vol. 6, no. 3, pp. 183–191, 2007.

[9] K. S. Novoselov, A. K. Geim, S. V. Morozov, D. Jiang, Y. Zhang, S. V. Dubonos, I. V. Grigorieva, and A. A. Firsov, "Electric field effect in atomically thin carbon films," *Science*, vol. 306, no. 5696, pp. 666–669, 2004.

[10] A. H. Castro Neto, F. Guinea, N. M. R. Peres, K. S. Novoselov, and A. K. Geim, "The electronic properties of graphene," *Rev. Mod. Phys.*, vol. 81, pp. 109–162, Jan 2009.

[11] V. P. Gusynin, S. G. Sharapov, and J. P. Carbotte, "Magneto-optical conductivity in graphene," *Journal of Physics: Condensed Matter*, vol. 19, no. 2, p. 026222, 2007.

[12] G. W. Hanson, "Dyadic greenâĂŹs functions and guided surface waves for a surface conductivity model of graphene," *Journal of Applied Physics*, vol. 103, no. 6, p. 064302, 2008.

[13] F. H. L. Koppens, D. E. Chang, and F. J. G. de Abajo, "Graphene plasmonics: A platform for strong light-matter interactions," *Nano Letters*, vol. 11, no. 8, pp. 3370–3377, 2011. PMID: 21766812.

[14] K. S. Novoselov, A. K. Geim, S. V. Morozov, D. Jiang, Y. Zhang, S. V. Dubonos, I. V. Grigorieva, and A. A. Firsov, "Electric field effect in atomically thin carbon films," *Science*, vol. 306, no. 5696, pp. 666–669, 2004.

[15] K. Novoselov, A. Geim, S. Morozov, D. Jiang, M. K. I. Grigorieva, S. Dubonos, and A. Firsov, "Two-dimensional gas of massless dirac fermions in graphene," *Nature*, vol. 438, no. 7065, pp. 197–200, 2005.

[16] S. Maier, *Plasmonics: Fundamentals and Applications*. Springer US, 2010.

[17] L. A. Falkovsky and A. A. Varlamov, "Space-time dispersion of graphene conductivity," *Eur. Phys. J. B*, vol. 56, pp. 281–284, 2007.

[18] A. Vakil and N. Engheta, "Transformation optics using graphene," *Science*, vol. 332, no. 6035, pp. 1291–1294, 2011.

[19] Z. Lu and W. Zhao, "Nanoscale electro-optic modulators based on graphene-slot waveguides," *J. Opt. Soc. Am. B*, vol. 29, pp. 1490–1496, Jun 2012.

[20] D. R. Andersen, "Graphene-based long-wave infrared tm surface plasmon modulator," *J. Opt. Soc. Am. B*, vol. 27, pp. 818–823, Apr 2010.

[21] B. Sensale-Rodriguez, R. Yan, M. M. Kelly, T. Fang, K. Tahy, W. S. Hwang, D. Jena, L. Liu, and H. G. Xing, "Broadband graphene terahertz modulators enabled by intraband transitions," *Nature communications*, vol. 3, p. 780, 2012.

[22] M. Liu, X. Yin, E. Ulin-Avila, B. Geng, T. Zentgraf, L. Ju, F. Wang, and X. Zhang, "A graphene-based broadband optical modulator," *Nature*, vol. 474, no. 7349, pp. 64–67, 2011.

[23] D. Sounas and C. Caloz, "Gyrotropy and nonreciprocity of graphene for microwave applications," *Microwave Theory and Techniques, IEEE Transactions on*, vol. 60, pp. 901–914, April 2012.

[24] A. Grigorenko, M. Polini, and K. Novoselov, "Graphene plasmonics," *Nature photonics*, vol. 6, no. 11, pp. 749–758, 2012.

[25] F. Bonaccorso, Z. Sun, T. Hasan, and A. Ferrari, "Graphene photonics and optoelectronics," *Nature Photonics*, vol. 4, no. 9, pp. 611–622, 2010.

[26] S. Thongrattanasiri, F. H. L. Koppens, and F. J. García de Abajo, "Complete optical absorption in periodically patterned graphene," *Phys. Rev. Lett.*, vol. 108, p. 047401, Jan 2012.

[27] Z. Fang, S. Thongrattanasiri, A. Schlather, Z. Liu, L. Ma, Y. Wang, P. M. Ajayan, P. Nordlander, N. J. Halas, and F. J. G. de Abajo, "Gated tunability and hybridization of localized plasmons in nanostructured graphene," *ACS Nano*, vol. 7, no. 3, pp. 2388–2395, 2013. PMID: 23390960.

[28] L. Ju, B. Geng, J. Horng, C. Girit, M. Martin, Z. Hao, H. A. Bechtel, X. Liang, A. Zettl, Y. R. Shen, *et al.*, "Graphene plasmonics for tunable terahertz metamaterials," *Nature nanotechnology*, vol. 6, no. 10, pp. 630–634, 2011.

[29] S. Thongrattanasiri and F. J. García de Abajo, "Optical field enhancement by strong plasmon interaction in graphene nanostructures," *Phys. Rev. Lett.*, vol. 110, p. 187401, Apr 2013.

[30] N. Talebi and M. Shahabdi, "Analysis of the propagation of light along an array of nanorods using the generalized multipole techniques," *Journal of Computational and Theoretical Nanoscience*, vol. 5, no. 4, pp. 711–716, 2008.

[31] S. M. R. Z. Bajestani, M. Shahabadi, and N. Talebi, "Analysis of plasmon propagation along a chain of metal nanospheres using the generalized multipole technique," *J. Opt. Soc. Am. B*, vol. 28, pp. 937–943, Apr 2011.

[32] K. Kneipp, Y. Wang, H. Kneipp, L. T. Perelman, I. Itzkan, R. R. Dasari, and M. S. Feld, "Single molecule detection using surface-enhanced raman scattering (sers)," *Phys. Rev. Lett.*, vol. 78, pp. 1667–1670, Mar 1997.

[33] L. Novotny and N. Van Hulst, "Antennas for light," *Nature photonics*, vol. 5, no. 2, pp. 83–90, 2011.

[34] M. Jablan, H. Buljan, and M. Soljačić, "Plasmonics in graphene at infrared frequencies," *Phys. Rev. B*, vol. 80, p. 245435, Dec 2009.

[35] A. Woessner, M. B. Lundeberg, Y. Gao, A. Principi, P. Alonso-González, M. Carrega, K. Watanabe, T. Taniguchi, G. Vignale, M. Polini, *et al.*, "Highly confined low-loss plasmons in graphene–boron nitride heterostructures," *Nature Materials*, vol. 14, no. 4, pp. 421–425, 2015.

[36] A. Y. Nikitin, F. Guinea, F. J. García-Vidal, and L. Martín-Moreno, "Edge and waveguide terahertz surface plasmon modes in graphene microribbons," *Phys. Rev. B*, vol. 84, p. 161407, Oct 2011.

[37] M. Jablan, H. Buljan, and M. Soljačić, "Plasmonics in graphene at infrared frequencies," *Phys. Rev. B*, vol. 80, p. 245435, Dec 2009.

[38] E. H. Hwang and S. Das Sarma, "Dielectric function, screening, and plasmons in two-dimensional graphene," *Phys. Rev. B*, vol. 75, p. 205418, May 2007.

[39] E. G. Mishchenko, A. V. Shytov, and P. G. Silvestrov, "Guided plasmons in graphene *p-n* junctions," *Phys. Rev. Lett.*, vol. 104, p. 156806, Apr 2010.

[40] A. A. Dubinov, V. Y. Aleshkin, V. Mitin, T. Otsuji, and V. Ryzhii, "Terahertz surface plasmons in optically pumped graphene structures," *Journal of Physics: Condensed Matter*, vol. 23, no. 14, p. 145302, 2011.

[41] T. Low and P. Avouris, "Graphene plasmonics for terahertz to mid-infrared applications," *ACS Nano*, vol. 8, no. 2, pp. 1086–1101, 2014. PMID: 24484181.

[42] P. Li, T. Wang, H. Bï£¡ckmann, and T. Taubner, "Graphene-enhanced infrared near-field microscopy," *Nano Letters*, vol. 14, no. 8, pp. 4400–4405, 2014. PMID: 25019504.

[43] S. K. Vashist and A. G. Venkatesh, "Advances in graphene-based sensors and devices," *Nanomedicine and Nanotechnology*.

[44] Y. Liu, X. Dong, and P. Chen, "Biological and chemical sensors based on graphene materials," *Chem. Soc. Rev.*, vol. 41, pp. 2283–2307, 2012.

[45] P. Li and T. Taubner, "Broadband subwavelength imaging using a tunable graphene-lens," *ACS Nano*, vol. 6, no. 11, pp. 10107–10114, 2012. PMID: 23046079.

[46] A. Andryieuski, A. V. Lavrinenko, and D. N. Chigrin, "Graphene hyperlens for terahertz radiation," *Phys. Rev. B*, vol. 86, p. 121108, Sep 2012.

[47] A. Bostwick, T. Ohta, T. Seyller, K. Horn, and E. Rotenberg, "Quasiparticle dynamics in graphene," *Nature Physics*, vol. 3, no. 1, pp. 36–40, 2007.

[48] Q. Bao, H. Zhang, B. Wang, Z. Ni, C. H. Y. X. Lim, Y. Wang, D. Y. Tang, and K. P. Loh, "Broadband graphene polarizer," *Nature Photonics*, vol. 5, no. 7, pp. 411–415, 2011.

[49] G. Zumofen, N. M. Mojarad, V. Sandoghdar, and M. Agio, "Perfect reflection of light by an oscillating dipole," *Phys. Rev. Lett.*, vol. 101, p. 180404, Oct 2008.

[50] M. Pototschnig, Y. Chassagneux, J. Hwang, G. Zumofen, A. Renn, and V. Sandoghdar, "Controlling the phase of a light beam with a single molecule," *Phys. Rev. Lett.*, vol. 107, p. 063001, Aug 2011.

[51] R. W. Boyd, *Nonlinear Optics, Third Edition*. Academic Press, 3rd ed., 2008.

[52] T. Echtermeyer, L. Britnell, P. Jasnos, A. Lombardo, R. Gorbachev, A. Grigorenko, A. Geim, A. Ferrari, and K. Novoselov, "Strong plasmonic enhancement of photovoltage in graphene," *Nature communications*, vol. 2, p. 458, 2011.

[53] Z. Fang, Z. Liu, Y. Wang, P. M. Ajayan, P. Nordlander, and N. J. Halas, "Graphene-antenna sandwich photodetector," *Nano Letters*, vol. 12, no. 7, pp. 3808–3813, 2012. PMID: 22703522.

[54] L. Kang, J. Chu, H. Zhao, P. Xu, and M. Sun, "Recent progress in the applications of graphene in surface-enhanced raman scattering and plasmon-induced catalytic reactions," *J. Mater. Chem. C*, vol. 3, pp. 9024–9037, 2015.

[55] M. Khorasaninejad, S. Raeis-Zadeh, S. Jafarlou, M. Wesolowski, C. Daley, J. Flannery, J. Forrest, S. Safavi-Naeini, and S. Saini, "Highly enhanced raman scattering of graphene using plasmonic nano-structure," *Scientific reports*, vol. 3, 2013.

[56] I. Llatser, C. Kremers, A. Cabellos-Aparicio, J. M. Jornet, E. Alarcï£¡n, and D. N. Chigrin, "Graphene-based nano-patch antenna for terahertz radiation," *Photonics and Nanostructures - Fundamentals and Applications*, vol. 10, no. 4, pp. 353 – 358, 2012. TaCoNa-Photonics 2011.

[57] A. Mock, "Padé approximant spectral fit for fdtd simulation of graphene in the near infrared," *Opt. Mater. Express*, vol. 2, pp. 771–781, Jun 2012.

[58] G. Bouzianas, N. Kantartzis, C. Antonopoulos, and T. Tsiboukis, "Optimal modeling of infinite graphene sheets via a class of generalized fdtd schemes," *Magnetics, IEEE Transactions on*, vol. 48, pp. 379–382, Feb 2012.

[59] X. Yu and C. Sarris, "A perfectly matched layer for subcell fdtd and applications to the modeling of graphene structures," *Antennas and Wireless Propagation Letters, IEEE*, vol. 11, pp. 1080–1083, 2012.

[60] V. Nayyeri, M. Soleimani, and O. Ramahi, "Modeling graphene in the finite-difference time-domain method using a surface boundary condition," *Antennas and Propagation, IEEE Transactions on*, vol. 61, pp. 4176–4182, Aug 2013.

[61] H. Lin, M. F. Pantoja, L. D. Angulo, J. Alvarez, R. G. Martin, and S. G. Garcia, "Fdtd modeling of graphene devices using complex conjugate dispersion material model," *Microwave and Wireless Components Letters, IEEE*, vol. 22, pp. 612–614, Dec 2012.

[62] M. Tonouchi, "Cutting-edge terahertz technology," *Nature photonics*, vol. 1, no. 2, pp. 97–105, 2007.

[63] S. A. Mikhailov, "Theory of the giant plasmon-enhanced second-harmonic generation in graphene and semiconductor two-dimensional electron systems," *Phys. Rev. B*, vol. 84, p. 045432, Jul 2011.

[64] E. Hendry, P. J. Hale, J. Moger, A. K. Savchenko, and S. A. Mikhailov, "Coherent nonlinear optical response of graphene," *Phys. Rev. Lett.*, vol. 105, p. 097401, Aug 2010.

[65] S. Mikhailov, "Electromagnetic response of electrons in graphene: Non-linear effects," *Physica E: Low-dimensional Systems and Nanostructures*, vol. 40, no. 7, pp. 2626 – 2629, 2008. Proceedings of the E-MRS 2007 Symposia L and M: Electron Transport in Low-Dimensional Carbon Structures and Science and Technology of Nanotubes and Nanowires.

[66] S. Mikhailov, "Electromagnetic response of electrons in graphene: Non-linear effects," *Physica E: Low-dimensional Systems and Nanostructures*, vol. 40, no. 7, pp. 2626 – 2629, 2008. Proceedings of the E-MRS 2007 Symposia L and M: Electron Transport in Low-Dimensional Carbon Structures and Science and Technology of Nanotubes and Nanowires.

[67] S. A. Mikhailov and K. Ziegler, "Nonlinear electromagnetic response of graphene: frequency multiplication and the self-consistent-field effects," *Journal of Physics: Condensed Matter*, vol. 20, no. 38, p. 384204, 2008.

[68] K. L. Ishikawa, "Nonlinear optical response of graphene in time domain," *Phys. Rev. B*, vol. 82, p. 201402, Nov 2010.

[69] J. J. Dean and H. M. van Driel, "Graphene and few-layer graphite probed by second-harmonic generation: Theory and experiment," *Phys. Rev. B*, vol. 82, p. 125411, Sep 2010.

[70] S. Wu, L. Mao, A. M. Jones, W. Yao, C. Zhang, and X. Xu, "Quantum-enhanced tunable second-order optical nonlinearity in bilayer graphene," *Nano Letters*, vol. 12, no. 4, pp. 2032–2036, 2012. PMID: 22369519.

[71] Y. Q. An, F. Nelson, J. U. Lee, and A. C. Diebold, "Enhanced optical second-harmonic generation from the current-biased graphene/sio2/si(001) structure," *Nano Letters*, vol. 13, no. 5, pp. 2104–2109, 2013. PMID: 23581964.

[72] J. Maysonnave, S. Huppert, F. Wang, S. Maero, C. Berger, W. de Heer, T. B. Norris, L. A. D. Vaulchier, S. Dhillon, J. Tignon, R. Ferreira, and J. Mangeney, "Terahertz generation by dynamical photon drag effect in graphene excited by femtosecond optical pulses," *Nano Letters*, vol. 14, no. 10, pp. 5797–5802, 2014. PMID: 25226076.

[73] S. V. G. M. K.-G. A. N. O. P. A. Obraztsov, T. Kaplas and Y. P. Svirko, "All-optical control of ultrafast photocurrents in unbiased graphene," *Scientific Reports*, no. 4007, 2014.

[74] M. V. Entin, L. I. Magarill, and D. L. Shepelyansky, "Theory of resonant photon drag in monolayer graphene," *Phys. Rev. B*, vol. 81, p. 165441, Apr 2010.

[75] A. A. Grinberg and S. Luryi, "Theory of the photon-drag effect in a two-dimensional electron gas," *Phys. Rev. B*, vol. 38, pp. 87–96, Jul 1988.

[76] K. S. Novoselov, A. K. Geim, S. V. Morozov, D. Jiang, Y. Zhang, S. V. Dubonos, I. V. Grigorieva, and A. A. Firsov, "Electric field effect in atomically thin carbon films," *Science*, vol. 306, no. 5696, pp. 666–669, 2004.

[77] X. Li, W. Cai, J. An, S. Kim, J. Nah, D. Yang, R. Piner, A. Velamakanni, I. Jung, E. Tutuc, S. K. Banerjee, L. Colombo, and R. S. Ruoff, "Large-area synthesis of high-quality and uniform graphene films on copper foils," *Science*, vol. 324, no. 5932, pp. 1312–1314, 2009.

[78] K. Yoo, Y. Takei, B. Hou, S. Chiashi, S. Maruyama, K. Matsumoto, and I. Shimoyama, "Direct physical exfoliation and transfer of graphene grown via ethanol chemical vapor deposition," in *Micro Electro Mechanical Systems (MEMS), 2011 IEEE 24th International Conference on*, pp. 99–102, Jan 2011.

[79] O. Habibpour, *Fabrication, Characterisation and Modelling of Subharmonic Graphene FET Mixers*. Department of Microtechnology and Nanoscience, Terahertz and Millimetre Wave Laboratory, Chalmers University of Technology,, 2011.

[80] P. Avouris, "Graphene: Electronic and photonic properties and devices," *Nano Letters*, vol. 10, no. 11, pp. 4285–4294, 2010. PMID: 20879723.

[81] C.-F. Chen, C.-H. Park, B. W. Boudouris, J. Horng, B. Geng, C. Girit, A. Zettl, M. F. Crommie, R. A. Segalman, S. G. Louie, *et al.*, "Controlling inelastic light scattering quantum pathways in graphene," *Nature*, vol. 471, no. 7340, pp. 617–620, 2011.

[82] D. K. Efetov and P. Kim, "Controlling electron-phonon interactions in graphene at ultrahigh carrier densities," *Phys. Rev. Lett.*, vol. 105, p. 256805, Dec 2010.

[83] K. Nagashio, T. Nishimura, K. Kita, and A. Toriumi, "Metal/graphene contact as a performance killer of ultra-high mobility graphene analysis of intrinsic mobility and contact resistance," in *Electron Devices Meeting (IEDM), 2009 IEEE International*, pp. 1–4, Dec 2009.

[84] P. B. Johnson and R. W. Christy, "Optical constants of the noble metals," *Phys. Rev. B*, vol. 6, pp. 4370–4379, Dec 1972.

[85] A. C. Ferrari, J. C. Meyer, V. Scardaci, C. Casiraghi, M. Lazzeri, F. Mauri, S. Piscanec, D. Jiang, K. S. Novoselov, S. Roth, and A. K. Geim, "Raman spectrum of graphene and graphene layers," *Phys. Rev. Lett.*, vol. 97, p. 187401, Oct 2006.

[86] M. Khorasaninejad, N. Dhindsa, J. Walia, S. Patchett, and S. S. Saini, "Highly enhanced raman scattering from coupled vertical silicon nanowire arrays," *Applied Physics Letters*, vol. 101, no. 17, 2012.

[87] M. Mittendorff, S. Winnerl, J. Kamann, J. Eroms, D. Weiss, H. Schneider, and M. Helm, "Ultrafast graphene-based broadband thz detector," *Applied Physics Letters*, vol. 103, no. 2, 2013.

[88] X. Cai, A. B. Sushkov, R. J. Suess, M. M. Jadidi, G. S. Jenkins, L. O. Nyakiti, R. L. Myers-Ward, S. Li, J. Yan, D. K. Gaskill, *et al.*, "Sensitive room-temperature terahertz detection via the photothermoelectric effect in graphene," *Nature nanotechnology*, vol. 9, no. 10, pp. 814–819, 2014.

[89] S. M. Raeis-Zadeh, D. Strickland, and S. Safavi-Naeini, "Quantum-enhanced second-order nonlinearity in graphene: The role of wave momentum and dc biasing," *IEEE Journal of Quantum Electronics*, vol. 52, no. 2, pp. 1–7, 2016.

[90] M. Scully and M. Zubairy, *Quantum Optics*. Cambridge University Press, 1997.

[91] X. Yao and A. Belyanin, "Giant optical nonlinearity of graphene in a strong magnetic field," *Phys. Rev. Lett.*, vol. 108, p. 255503, Jun 2012.

[92] S. Das Sarma, S. Adam, E. H. Hwang, and E. Rossi, "Electronic transport in two-dimensional graphene," *Rev. Mod. Phys.*, vol. 83, pp. 407–470, May 2011.

[93] H. Lin, M. F. Pantoja, L. D. Angulo, J. Alvarez, R. G. Martin, and S. G. Garcia, "Fdtd modeling of graphene devices using complex conjugate dispersion material model," *Russ. Math. Surv.*, vol. 22, no. 2, pp. 58–107, 1967.

[94] C. Hafner, "Multiple multipole program computation of periodic structures," *J. Opt. Soc. Am. A*, vol. 12, pp. 1057–1067, May 1995.

[95] A. B. Evlyukhin, C. Reinhardt, E. Evlyukhin, and B. N. Chichkov, "Multipole analysis of light scattering by arbitrary-shaped nanoparticles on a plane surface," *J. Opt. Soc. Am. B*, vol. 30, pp. 2589–2598, Oct 2013.

[96] D. Pissoort, E. Michielssen, D. Vande Ginste, and F. Olyslager, "Fast-multipole analysis of electromagnetic scattering by photonic crystal slabs," *Lightwave Technology, Journal of*, vol. 25, pp. 2847–2863, Sept 2007.

[97] N. Bartoli, F. Collino, F. Dodu, and T. Koleck, "A far-near field transformation using the fast multipole techniques," *Antennas and Propagation, IEEE Transactions on*, vol. 52, pp. 3329–3336, Dec 2004.

[98] J. Xu and X. Zhang, "Second harmonic generation in three-dimensional structures based on homogeneous centrosymmetric metallic spheres," *Opt. Express*, vol. 20, pp. 1668–1684, Jan 2012.

[99] A. Vallecchi, M. Albani, and F. Capolino, "Collective electric and magnetic plasmonic resonances in spherical nanoclusters," *Opt. Express*, vol. 19, pp. 2754–2772, Jan 2011.

[100] M. Ahmadi-Boroujeni and M. Shahabadi, "Application of the generalized multipole technique to the analysis of a ladder parallel-plate waveguide for terahertz guided-wave applications," *J. Opt. Soc. Am. B*, vol. 27, pp. 2061–2067, Oct 2010.

[101] E. Moreno, D. Erni, and C. Hafner, "Band structure computations of metallic photonic crystals with the multiple multipole method," *Phys. Rev. B*, vol. 65, p. 155120, Apr 2002.

[102] C. Hafner, "The generalized multipole technique for computational electromagnetics," *The Generalized Multipole Technique for Computational Electromagnetics*, 1990. cited By 0.

[103] R. F. Harrington, *Time-Harmonic Electromagnetic Fields*. IEEE-Press, 2001.

[104] I. Braver, P. Fridberg, K. Garb, and I. Yakover, "The behavior of the electromagnetic field near the edge of a resistive half-plane," *Antennas and Propagation, IEEE Transactions on*, vol. 36, pp. 1760–1768, Dec 1988.

[105] P. Leuchtmann and F. Bomholt, "Field modeling with the mmp code," *IEEE Trans. Electromagn. Compat.*, 1993.

[106] P. Leuchtmann, "New expansion functions for long structures in the mmp-code," *7th Annual Review Progress Appl. Computational Electromagn. (ACES)*, 1991.

[107] E. Moreno, D. Erni, C. Hafner, and R. Vahldieck, "Multiple multipole method with automatic multipole setting applied to the simulation of surface plasmons in metallic nanostructures," *J. Opt. Soc. Am. A*, vol. 19, pp. 101–111, Jan 2002.

[108] J. Maysonnave, S. Huppert, F. Wang, S. Maero, C. Berger, W. de Heer, T. B. Norris, L. A. D. Vaulchier, S. Dhillon, J. Tignon, R. Ferreira, and J. Mangeney, "Terahertz generation by dynamical photon drag effect in graphene excited by femtosecond optical pulses," *Nano Letters*, vol. 14, no. 10, pp. 5797–5802, 2014. PMID: 25226076.

[109] L. Novotny and B. Hecht, "Principles of nano-optics," 2012.

[110] V. E. Bochenkov and D. S. Sutherland, "From rings to crescents: A novel fabrication technique uncovers the transition details," *Nano Letters*, vol. 13, no. 3, pp. 1216–1220, 2013. PMID: 23437977.

[111] D. Saeedkia, "Terahertz photoconductive antennas: Principles and applications," in *Antennas and Propagation (EUCAP), Proceedings of the 5th European Conference on*, pp. 3326–3328, April 2011.

[112] S. Preu, G. H. DÃűhler, S. Malzer, L. J. Wang, and A. C. Gossard, "Tunable, continuous-wave terahertz photomixer sources and applications," *Journal of Applied Physics*, vol. 109, no. 6, 2011.

[113] Y. Lee, *Principles of Terahertz Science and Technology*. Lecture Notes in Physics, Springer US, 2009.

[114] K. Tielrooij, J. Song, S. A. Jensen, A. Centeno, A. Pesquera, A. Z. Elorza, M. Bonn, L. Levitov, and F. Koppens, "Photoexcitation cascade and multiple hot-carrier generation in graphene," *Nature Physics*, vol. 9, no. 4, pp. 248–252, 2013.

Appendix A

A.1 Derivation of the second order nonlinearity tensor

Dirac eqaution that describes the electron behavior in graphene is as follows ($\xi = 1$ for the Dirac cone K and $\xi = -1$ for the Dirac cone K'):

$$\begin{aligned} H_0\psi(\mathbf{r}) &= \mathcal{E}\psi(\mathbf{r}) \\ H_0 &= \nu_F(\hat{p}_x\sigma_x + \xi\hat{p}_x\sigma_y) \end{aligned} \tag{A.1}$$

where H_0 is the Hamiltonian of the free standing graphene layer, ν_F is the Fermi velocity in graphene, and $\boldsymbol{\sigma}$'s are the Pauli matrices. The Hamiltonian of Eq. A.1 has the following eigenfunctions:

$$\Psi_{|l,\mathbf{k}\rangle} = \frac{1}{\sqrt{LW}} |l, \mathbf{k}\rangle \, e^{i\mathbf{k}.\mathbf{r}} \tag{A.2}$$

where $|l, \mathbf{k}\rangle$ is as follows:

$$|l, \mathbf{k}\rangle = \frac{1}{\sqrt{2}} \begin{pmatrix} e^{-i\xi\theta_k/2} \\ (-1)^l e^{i\xi\theta_k/2} \end{pmatrix} \tag{A.3}$$

In Eqs. A.3 and A.2, L and W are the length and width of the graphene layer, respectively; $\mathbf{k}$ is the electron wave vector; θ_k is the angle of the wave vector k from the x-axis; and l shows the corresponding wave function in the conduction ($l = 0$) or the valance ($l = 1$) band. The coupling between the electromagnetic wave with electrons in graphene can be formulated using the interaction Hamiltonian.

$$H = \hat{H}_0 + \hat{H}_{int} \tag{A.4}$$

where

$$\hat{H}_{int} = e\nu_F \left(\sigma_x A_x + \xi\sigma_y A_y\right) \tag{A.5}$$

where $\mathbf{A}$ is the magnetic vector potential. For a plane-wave excitation of the form:

$$\begin{aligned}\mathbf{E} &= \sum_\alpha \mathbf{E}_\alpha \cos(\mathbf{k}_\alpha.\mathbf{r} - \omega_\alpha t) \\ &= \frac{1}{2}\sum_\alpha \mathbf{E}(\omega_\alpha)e^{i(\mathbf{k}_\alpha.\mathbf{r}-\omega_\alpha t)} + \mathbf{E}(\omega_{-\alpha})e^{-i(\mathbf{k}_\alpha.\mathbf{r}-\omega_\alpha t)} \\ &= \frac{1}{2}\sum_\alpha \mathbf{E}(\mathbf{k}_\alpha,\omega_\alpha)e^{-i\omega_\alpha t} + \mathbf{E}(\mathbf{k}_{-\alpha},\omega_{-\alpha})e^{i\omega_\alpha t}\end{aligned} \tag{A.6}$$

the interaction Hamiltonian can be written as follows ($\mathbf{E}(\omega_\alpha) = \mathbf{E}(\omega_{-\alpha})$, $\omega_{-\alpha} = -\omega_\alpha$, and $\mathbf{k}_{-\alpha} = -\mathbf{k}_\alpha$):

$$\hat{H}_{int} = \sum_\alpha \frac{e\nu_F}{i2\omega_\alpha}\left(\sigma_x\hat{x} + \xi\sigma_y\hat{y}\right).\mathbf{E}(\mathbf{k}_{\alpha||},\omega_\alpha)e^{-i\omega_\alpha t} = \sum_\alpha \frac{1}{\omega_\alpha}\boldsymbol{\mu}.\mathbf{E}(\mathbf{k}_{\alpha||},\omega_\alpha)e^{-i\omega_\alpha t} \tag{A.7}$$

where $\mathbf{k}_{\alpha||}$ is the tangential part of wave vector $\mathbf{k}_\alpha$ on the graphene layer and $\boldsymbol{\mu} = -ie\nu_F\left(\sigma_x\hat{x} + \xi\sigma_y\hat{y}\right)/2$. The incident beam in our calculations is composed of two plane waves, one propagating perpendicular to the surface of graphene and the other one is obliquely incident.

$$\mathbf{E} = \frac{\mathbf{E}(-\omega_q)}{2}e^{-i(\mathbf{k}_q.\mathbf{r}-\omega_q t)} + \frac{\mathbf{E}(\omega_p)}{2}e^{i(k_p z-\omega_p t)} + c.c. \tag{A.8}$$

where $k_q = \omega_q/c$ and $k_p = \omega_p/c$ defines the wave vectors of incident waves; $\mathbf{E}(\omega_q)$ and $\mathbf{E}(\omega_p)$ are the amplitudes of electric field for the waves with the frequency $-\omega_q$ and ω_p, respectively (Since the electromagnetic field is real, we have $\mathbf{E}(\omega_q) = \mathbf{E}(-\omega_q)$ and $\mathbf{E}(\omega_p) = \mathbf{E}(-\omega_p)$). The DFG of the first two waves in Eq. A.8 will give the positive frequency component ω_d in the DFG while the complex conjugate of terms presented in Eq. A.8 will result in the negative part of the generated wave $-\omega_d$. From now on, we only consider the first two complex waves in Eq. A.8.

$$\mathbf{E}_c = \frac{\mathbf{E}(-\omega_q)}{2}e^{-i(\mathbf{k}_q.\mathbf{r}-\omega_q t)} + \frac{\mathbf{E}(\omega_p)}{2}e^{i(k_p z-\omega_p t)} \tag{A.9}$$

The first ($\rho^{(1)}$) and the second ($\rho^{(2)}$) order perturbations of the density matrix can be calculated from the following formula [51]:

$$\rho^{(1)}_{|n,\mathbf{k}\rangle|m,\kappa\rangle} = \int_{-\infty}^{t} \frac{-i}{\hbar}\left[\hat{H}_{int},\rho^{(0)}\right]_{|n,\mathbf{k}\rangle|m,\boldsymbol{\kappa}\rangle} e^{(i\omega_{|n,\mathbf{k}\rangle|m,\boldsymbol{\kappa}\rangle}+\Gamma)(t'-t)}dt' \tag{A.10}$$

$$\rho^{(2)}_{|n,\mathbf{k}\rangle|m,\kappa\rangle} = \int_{-\infty}^{t} \frac{-i}{\hbar}\left[\hat{H}_{int},\rho^{(1)}\right]_{|n,\mathbf{k}\rangle|m,\boldsymbol{\kappa}\rangle} e^{(i\omega_{|n,\mathbf{k}\rangle|m,\boldsymbol{\kappa}\rangle}+\Gamma)(t'-t)}dt' \tag{A.11}$$

where $\rho^{(0)}$ is the Fermi-Dirac distribution in the absence of the electromagnetic field, Γ is the phenomenological factor showing the electron relaxation time, and $\hbar\omega_{|n,\mathbf{k}\rangle|m,\kappa\rangle}$ is the transition energy from the state $|m,\kappa\rangle$ to the state $|n,\mathbf{k}\rangle$. Using the second order perturbation of density matrix, it is possible to find the induced nonlinear current and consequently the second order conductivity tensor for the DFG in graphene.

$$\mathbf{j}^{(2)}(\omega_d) = 2e\sum_{B.Z.} tr\left\{\hat{\rho}^{(2)}\frac{\partial\hat{H}}{\partial\mathbf{p}}\right\} = \frac{e\nu_F}{2\pi^2}\int \hat{\rho}^{(2)}(\sigma_x\hat{x}+\xi\sigma_y\hat{y})d^2k \tag{A.12}$$

where the factor 2 shows the spin degeneracy, the summation should be carried out for the whole Brillouin zone, and $j_s^{(2)}(\omega_d)$ is related to the second order nonlinearity tensor through:

$$j_s^{(2)}(\omega_d) = \sigma^{(2)}_{sij}(\omega_d,-\omega_q,\omega_p,\mathbf{k}_{q||})E_i(\omega_p)E_j(-\omega_q)e^{-i(\mathbf{k}_{q||}.\mathbf{r}+\omega_d t)} \tag{A.13}$$

It is worth mentioning that in the low energy limit the dynamics of electrons can be described by the Dirac equation around Dirac points K and K' and consequently the integration over the whole Brillouin zone (B.Z.) can be reduced to the integration near the Dirac points K and K'. To calculate the integrals in Eq. A.10 and Eq. A.11, we can write: ($\sum \Psi_{|l,\mathbf{k}''\rangle}\Psi\langle l,\mathbf{k}''| = \mathbf{1}$, where $\mathbf{1}$ is the identity matrix):

$$\left[\hat{H}_{int},\rho^{(N)}\right]_{\Psi|n,\boldsymbol{\kappa}\rangle\Psi|m,\mathbf{k}\rangle} = \sum_{\Psi|l,\boldsymbol{\kappa}''\rangle}\left[(H_{int})_{\Psi|n,\boldsymbol{\kappa}\rangle\Psi|l,\boldsymbol{\kappa}''\rangle}\rho^{(N)}_{\Psi|l,\boldsymbol{\kappa}''\rangle\Psi|m,\mathbf{k}\rangle}\right] - \sum_{\Psi|l,\mathbf{k}''\rangle}\left[(H_{int})_{\Psi|l,\mathbf{k}''\rangle\Psi|m,\mathbf{k}\rangle}\rho^{(N)}_{\Psi|n,\boldsymbol{\kappa}\rangle\Psi|l,\mathbf{k}''\rangle}\right] \tag{A.14}$$

where the matrix elements of $\hat{H}_{int}$ can be further simplified by calculating the spatial integration, e. g.,

$$\begin{aligned}(H_{int})_{\Psi|n,\boldsymbol{\kappa}\rangle\Psi|l,\boldsymbol{\kappa}''\rangle} =& \frac{e^{-i\omega_\alpha t}}{\omega_\alpha}\mathbf{E}(\omega_\alpha).\int_S \Psi^*_{|n,\boldsymbol{\kappa}\rangle}\boldsymbol{\mu}e^{i\mathbf{k}_\alpha.\mathbf{r}}\Psi_{|l,\boldsymbol{\kappa}''\rangle}d^2r \\ =& \frac{e^{-i\omega_\alpha t}}{\omega_\alpha}\boldsymbol{\mu}_{|n,\boldsymbol{\kappa}\rangle|l,\boldsymbol{\kappa}''\rangle}.\mathbf{E}(\omega_\alpha)\end{aligned} \tag{A.15}$$

where S is the surface of graphene and $\boldsymbol{\kappa} = \boldsymbol{\kappa}'' + \mathbf{k}_{\alpha||}$ is the expected result from the conservation of the momentum. Using the similar calculation for different elements of $\hat{H}_{int}$, one can obtain:

$$\begin{aligned}\left[\hat{H}_{int}, \rho^{(N)}\right]_{\Psi|n,\boldsymbol{\kappa}\rangle\Psi|m,\mathbf{k}\rangle} &= \sum_{\alpha} \frac{1}{\omega_\alpha} \sum_{|l,\mathbf{k}''\rangle} \boldsymbol{\mu}_{|n,\boldsymbol{\kappa}\rangle|l,\boldsymbol{\kappa}''\rangle}.\mathbf{E}(\omega_\alpha) e^{-i\omega_\alpha t} \rho^{(N)}_{|l,\boldsymbol{\kappa}''\rangle|m,\mathbf{k}\rangle} \\ &- \sum_{\alpha} \frac{1}{\omega_\alpha} \sum_{|l,\mathbf{k}''\rangle} \boldsymbol{\mu}_{|l,\mathbf{k}''\rangle|m,\mathbf{k}\rangle}.\mathbf{E}(\omega_\alpha) e^{-i\omega_\alpha t} \rho^{(N)}_{|n,\boldsymbol{\kappa}\rangle|l,\mathbf{k}''\rangle} \end{aligned} \tag{A.16}$$

where $\mathbf{k}'' = \mathbf{k} + \mathbf{k}_{\alpha||}$. For the case of $N = 0$, Eq. A.16 can be further simplified to:

$$\left[\hat{H}_{int}, \rho^{(0)}\right]_{\Psi|n,\boldsymbol{\kappa}\rangle\Psi|m,\mathbf{k}\rangle} = \sum_{\alpha} \frac{1}{\omega_\alpha} \left(\rho^{(0)}_{|m,\mathbf{k}\rangle} - \rho^{(0)}_{|n,\boldsymbol{\kappa}\rangle}\right) \boldsymbol{\mu}_{|n,\boldsymbol{\kappa}\rangle|m,\mathbf{k}\rangle}.\mathbf{E}(\omega_\alpha) e^{-i\omega_\alpha t} \tag{A.17}$$

where we used the fact that $\rho^{(0)}_{mn} = 0$ for $m \neq n$ ($\boldsymbol{\kappa} = \mathbf{k} + \mathbf{k}_{\alpha||}$). For the excitation introduced in Eq. A.9, the Eq. A.17 should be written as follows:

$$\begin{aligned}\left[\hat{H}_{int}, \rho^{(0)}\right]_{\Psi|n,\mathbf{k}\rangle\Psi|m,\mathbf{k}\rangle} &= \frac{1}{\omega_p} \left(\rho^{(0)}_{|m,\mathbf{k}\rangle} - \rho^{(0)}_{|n,\mathbf{k}\rangle}\right) \boldsymbol{\mu}_{|n,\mathbf{k}\rangle|m,\mathbf{k}\rangle}.\mathbf{E}(\omega_p) e^{-i\omega_p t} \\ &+ \frac{1}{-\omega_q} \left(\rho^{(0)}_{|m,\mathbf{k}\rangle} - \rho^{(0)}_{|n,\mathbf{k}'\rangle}\right) \boldsymbol{\mu}_{|n,\mathbf{k}'\rangle|m,\mathbf{k}\rangle}.\mathbf{E}(-\omega_q) e^{i\omega_q t} \end{aligned} \tag{A.18}$$

where $\mathbf{k}' = \mathbf{k} - \mathbf{k}_{q||}$. The explicit forms of $\boldsymbol{\mu}_{|n,\mathbf{k}\rangle|m,\mathbf{k}\rangle}$ and $\boldsymbol{\mu}_{|n,\mathbf{k}'\rangle|m,\mathbf{k}\rangle}$ are as follows:

$$\begin{aligned}\boldsymbol{\mu}_{|n,\mathbf{k}\rangle|m,\mathbf{k}\rangle} &= \langle n,\mathbf{k}| - ie\nu_F \left(\sigma_x \hat{x} + \xi\sigma_y \hat{y}\right)/2 \,|m,\mathbf{k}\rangle \\ \boldsymbol{\mu}_{|n,\mathbf{k}'\rangle|m,\mathbf{k}\rangle} &= \langle n,\mathbf{k}'| - ie\nu_F \left(\sigma_x \hat{x} + \xi\sigma_y \hat{y}\right)/2 \,|m,\mathbf{k}\rangle \end{aligned} \tag{A.19}$$

where the state $\langle n,\mathbf{k}|$ is the conjugate transpose of the state $|n,\mathbf{k}\rangle$. We use the representation of Eq. A.19 in our numerical calculations. For the simplicity of derivation, we consider

$$\boldsymbol{\mu}_{nm}.\mathbf{E} = \boldsymbol{\mu}_{|n,\mathbf{k}\rangle|m,\mathbf{k}\rangle}.\mathbf{E}(\omega_p)\frac{e^{-i\omega_p t}}{\omega_p} + \boldsymbol{\mu}_{|n,\mathbf{k}'\rangle|m,\mathbf{k}\rangle}.\mathbf{E}(-\omega_q)\frac{e^{i\omega_q t}}{-\omega_q}. \tag{A.20}$$

Substituting Eq. A.18 into Eq. A.10, we have:

$$\begin{aligned}\rho^{(1)}_{lm} = \rho^{(1)}_{|l,\mathbf{k}\rangle|m,\mathbf{k}\rangle} + \rho^{(1)}_{|l,\mathbf{k}'\rangle|m,\mathbf{k}\rangle} &= -\left\{\hbar^{-1}\left(\rho^{(0)}_{|m,\mathbf{k}\rangle} - \rho^{(0)}_{|l,\mathbf{k}\rangle}\right)\frac{\mu_{|l,\mathbf{k}\rangle|m,\mathbf{k}\rangle} E(\omega_p)/\omega_p}{\left(\omega_{|l,\mathbf{k}\rangle|m,\mathbf{k}\rangle} - \omega_p\right) - i\Gamma}\right\} e^{-i\omega_p t} \\ &+ \left\{\hbar^{-1}\left(\rho^{(0)}_{|m,\mathbf{k}\rangle} - \rho^{(0)}_{|l,\mathbf{k}'\rangle}\right)\frac{\mu_{|l,\mathbf{k}'\rangle|m,\mathbf{k}\rangle} E(-\omega_q)/\omega_q}{\left(\omega_{|l,\mathbf{k}'\rangle|m,\mathbf{k}\rangle} + \omega_q\right) - i\Gamma}\right\} e^{i\omega_q t} \end{aligned} \tag{A.21}$$

The value of $\rho^{(1)}_{lm}$ is used as a short form replacing $\rho^{(1)}_{|l,\mathbf{k}\rangle|m,\mathbf{k}\rangle} + \rho^{(1)}_{|l,\mathbf{k}'\rangle|m,\mathbf{k}\rangle}$.

The second order perturbation of density matrix can be evaluated using the following relation:

$$\left[\hat{H}_{int}, \rho^{(1)}\right]_{nm} = \sum_{l} \left(\boldsymbol{\mu}_{nl}.\mathbf{E}\rho^{(1)}_{lm} - \boldsymbol{\mu}_{lm}.\mathbf{E}\rho^{(1)}_{nl}\right) \tag{A.22}$$

where $\boldsymbol{\mu}_{nl}.\mathbf{E}$ has the following form:

$$\boldsymbol{\mu}_{nl}.\mathbf{E} = \boldsymbol{\mu}_{|n,\mathbf{k}'\rangle|l,\mathbf{k}\rangle}.\mathbf{E}(-\omega_q)\frac{e^{i\omega_q t}}{-\omega_q} + \boldsymbol{\mu}_{|n,\mathbf{k}'\rangle|l,\mathbf{k}'\rangle}.\mathbf{E}(\omega_p)\frac{e^{-i\omega_p t}}{\omega_p}. \tag{A.23}$$

In the product of $\boldsymbol{\mu}_{nl}.\mathbf{E}\rho^{(1)}_{lm}$, we only The same formulation can be used to find the values of $\boldsymbol{\mu}_{lm}.\mathbf{E}\rho^{(1)}_{nl}$. Substituting $\boldsymbol{\mu}_{lm}.\mathbf{E}\rho^{(1)}_{nl}$ and $\boldsymbol{\mu}_{nl}.\mathbf{E}\rho^{(1)}_{nl}$ into Eq. A.22, we get:

$$\begin{aligned}\left[\hat{H}_{int}, \rho^{(1)}\right]_{nm} = \frac{1}{\hbar\omega_p\omega_q}\sum_{l=1}^{2}\Bigg\{ & \left(\rho^{(0)}_{|m,\mathbf{k}\rangle} - \rho^{(0)}_{|l,\mathbf{k}\rangle}\right)\frac{\boldsymbol{\mu}_{|l,\mathbf{k}\rangle|m,\mathbf{k}\rangle}.\mathbf{E}(\omega_p)\mathbf{E}(-\omega_q).\boldsymbol{\mu}_{|n,\mathbf{k}'\rangle|l,\mathbf{k}\rangle}}{\left(\omega_{|l,\mathbf{k}\rangle|m,\mathbf{k}\rangle} - \omega_p\right) - j\Gamma} \\ & + \left(\rho^{(0)}_{|m,\mathbf{k}\rangle} - \rho^{(0)}_{|l,\mathbf{k}'\rangle}\right)\frac{\boldsymbol{\mu}_{|l,\mathbf{k}'\rangle|m,\mathbf{k}\rangle}.\mathbf{E}(-\omega_q)\mathbf{E}(\omega_p).\boldsymbol{\mu}_{|n,\mathbf{k}'\rangle|l,\mathbf{k}'\rangle}}{\left(\omega_{|l,\mathbf{k}'\rangle|m,\mathbf{k}\rangle} + \omega_q\right) - j\Gamma} \\ & - \left(\rho^{(0)}_{|l,\mathbf{k}'\rangle} - \rho^{(0)}_{|n,\mathbf{k}'\rangle}\right)\frac{\boldsymbol{\mu}_{|n,\mathbf{k}'\rangle|l,\mathbf{k}'\rangle}.\mathbf{E}(\omega_p)\mathbf{E}(-\omega_q).\boldsymbol{\mu}_{|l,\mathbf{k}'\rangle|m,\mathbf{k}\rangle}}{\left(\omega_{|n,\mathbf{k}'\rangle|l,\mathbf{k}'\rangle} - \omega_p\right) - j\Gamma} \\ & - \left(\rho^{(0)}_{|l,\mathbf{k}\rangle} - \rho^{(0)}_{|n,\mathbf{k}'\rangle}\right)\frac{\boldsymbol{\mu}_{|n,\mathbf{k}'\rangle|l,\mathbf{k}\rangle}.\mathbf{E}(-\omega_q)\mathbf{E}(\omega_p).\boldsymbol{\mu}_{|l,\mathbf{k}\rangle|m,\mathbf{k}\rangle}}{\left(\omega_{|n,\mathbf{k}'\rangle|l,\mathbf{k}\rangle} + \omega_q\right) - j\Gamma}\Bigg\} e^{-j\omega_d t}\end{aligned} \tag{A.24}$$

Having Eq. A.24, the total induced nonlinear current (Eq. A.12) can be calculated. Using

the total induced nonlinear current, the obtained tensor $\sigma^{(2)}_{sij}$ is as follows:

$$\begin{aligned}
&\sigma^{(2)}_{sij}(\omega_d, -\omega_q, \omega_p, \mathbf{k}_{q||}) \\
&= -\frac{e\nu_F}{2\pi^2\hbar^2\omega_p\omega_q}\sum_{n,m=1}^{2}\sum_{l=1}^{2}\int_{K,K'} d^2k \left\{ \left(\rho^{(0)}_{|m,\mathbf{k}\rangle} - \rho^{(0)}_{|l,\mathbf{k}\rangle}\right) \frac{\mu^i_{|l,\mathbf{k}\rangle|m,\mathbf{k}\rangle}\mu^j_{|n,\mathbf{k}'\rangle|l,\mathbf{k}\rangle}}{\left(\omega_{|l,\mathbf{k}\rangle|m,\mathbf{k}\rangle} - \omega_p\right) - i\Gamma} \right. \\
&+ \left(\rho^{(0)}_{|m,\mathbf{k}\rangle} - \rho^{(0)}_{|l,\mathbf{k}'\rangle}\right) \frac{\mu^j_{|l,\mathbf{k}'\rangle|m,\mathbf{k}\rangle}\mu^i_{|n,\mathbf{k}'\rangle|l,\mathbf{k}'\rangle}}{\left(\omega_{|l,\mathbf{k}'\rangle|m,\mathbf{k}\rangle} + \omega_q\right) - i\Gamma} \\
&- \left(\rho^{(0)}_{|l,\mathbf{k}'\rangle} - \rho^{(0)}_{|n,\mathbf{k}'\rangle}\right) \frac{\mu^i_{|n,\mathbf{k}'\rangle|l,\mathbf{k}'\rangle}\mu^j_{|l,\mathbf{k}'\rangle|m,\mathbf{k}\rangle}}{\left(\omega_{|n,\mathbf{k}'\rangle|l,\mathbf{k}'\rangle} - \omega_p\right) - i\Gamma} \\
&\left. - \left(\rho^{(0)}_{|l,\mathbf{k}\rangle} - \rho^{(0)}_{|n,\mathbf{k}'\rangle}\right) \frac{\mu^j_{|n,\mathbf{k}'\rangle|l,\mathbf{k}\rangle}\mu^i_{|l,\mathbf{k}\rangle|m,\mathbf{k}\rangle}}{\left(\omega_{|n,\mathbf{k}'\rangle|l,\mathbf{k}\rangle} + \omega_q\right) - i\Gamma} \right\} \frac{\eta^s_{|m,\mathbf{k}\rangle|n,\mathbf{k}'\rangle}}{\omega_{|n,\mathbf{k}'\rangle|m,\mathbf{k}\rangle} - \omega_d - i\Gamma}
\end{aligned} \tag{A.25}$$

where $\mathbf{k}_q$ is the wave vector of obliquely incident beam ($\mathbf{k}' = \mathbf{k} - \mathbf{k}_{q||}$), $\eta^s_{|m,\mathbf{k}\rangle|n,\mathbf{k}'\rangle} = \langle n,\mathbf{k}'|\frac{1}{\nu_F}\frac{\partial\hat{H}}{\partial p_s}|m,\mathbf{k}\rangle = \langle n,\mathbf{k}'|(\sigma_x\hat{x} + \xi\sigma_y\hat{y})|m,\mathbf{k}\rangle$.

A.2 The effect of wave momentum in the second order nonlinearity

To separate the effect of wave momentum ($\mathbf{k}_q$) in the second order conductivity tensor (Eq. A.25), we can expand the polarization vector as follows.

$$\mu^j_{|n,\mathbf{k}'\rangle|l,\mathbf{k}\rangle} = \mu^j_{|n,\mathbf{k}\rangle|l,\mathbf{k}\rangle} + (k'_a - k_a)\left.\frac{\partial\mu^j_{|n,\boldsymbol{\kappa}\rangle|l,\mathbf{k}\rangle}}{\partial\kappa_a}\right|_{\boldsymbol{\kappa}=\mathbf{k}} = \mu^j_{|n,\mathbf{k}\rangle|l,\mathbf{k}\rangle} - (k_p)_a\,\varsigma^{aj}_{|n,\mathbf{k}\rangle|l,\mathbf{k}\rangle} \tag{A.26}$$

where k_a shows the Cartesian components of wave vector $\mathbf{k}$, $\mathbf{k}_q$ is the wave vector of obliquely incident wave, and we define

$$\varsigma^{aj}_{|n,\mathbf{k}\rangle|l,\mathbf{k}\rangle} = \left.\frac{\partial\mu^j_{|n,\boldsymbol{\kappa}\rangle|l,\mathbf{k}\rangle}}{\partial\kappa_a}\right|_{\boldsymbol{\kappa}=\mathbf{k}}. \tag{A.27}$$

Similar expansions can be obtained for all the dipole moment terms in A.25. Using the Taylor series expansion of $\rho^{(0)}_{|n,\mathbf{k}'\rangle}$ and $\omega_{|a,\mathbf{k}'\rangle|m,\mathbf{k}\rangle}$, we can also get:

$$\begin{aligned}
\rho^{(0)}_{|n,\mathbf{k}'\rangle} &= \rho^{(0)}_{|n,\mathbf{k}\rangle} + (k_p)_a\,\Delta^a_{|n,\mathbf{k}\rangle} \\
\omega_{|l,\mathbf{k}'\rangle|m,\mathbf{k}\rangle} &\approx \omega_{|l,\mathbf{k}\rangle|m,\mathbf{k}\rangle}.
\end{aligned} \tag{A.28}$$

Where we used the fact that the transition frequency which appears in the denominator does not changes substantial as the direction of wave momentum changes. Substituting equations A.27 and A.28 into A.25 and retaining only the terms that depend linearly on $\mathbf{k}_q$, one can derive the general expression:

$$\sigma^{(2)}_{sij} = \chi^{(2)}_{sij} + T^{(2)}_{sija}\left(k_p\right)_a \tag{A.29}$$

where the tensor $\chi^{(2)}$ and $T^{(2)}_{sija}$ do not depend on the wave vector $\left(k_p\right)_a$. The tensor $T^{(2)}_{sija}$ is a tensor of rank four and determines the effect of incident wave momentum in the second order nonlinearity. The contribution of second term $(T^{(2)}_{sija}\left(k_p\right)_a)$ to the second order nonlinearity is known as the photon-drag effect.

A.3 Derivation of the second order nonlinearity tensor for two obliquely incident plane-waves

The second order perturbation of density matrix for two obliquely incident plane waves is as follows [51]:

$$\begin{aligned}\rho^{(2)}_{nm} = -\frac{1}{\hbar^2\omega_p\omega_2}\sum_{l=1}^{2}\int_{K,K'} d^2k \Bigg\{ & \left(\rho^{(0)}_{|m,\mathbf{k}\rangle} - \rho^{(0)}_{|l,\mathbf{k}_1\rangle}\right)\frac{\boldsymbol{\mu}_{|l,\mathbf{k}_1\rangle|m,\mathbf{k}\rangle}.\mathbf{E}(\omega_1)\mathbf{E}(-\omega_2).\boldsymbol{\mu}_{|n,\mathbf{k}_3\rangle|l,\mathbf{k}_1\rangle}}{\left(\omega_{|l,\mathbf{k}_1\rangle|m,\mathbf{k}\rangle} - \omega_1\right) - j\Gamma} \\ & + \left(\rho^{(0)}_{|m,\mathbf{k}\rangle} - \rho^{(0)}_{|l,\mathbf{k}_2\rangle}\right)\frac{\boldsymbol{\mu}_{|l,\mathbf{k}_2\rangle|m,\mathbf{k}\rangle}.\mathbf{E}(-\omega_2)\mathbf{E}(\omega_1).\boldsymbol{\mu}_{|n,\mathbf{k}_3\rangle|l,\mathbf{k}_2\rangle}}{\left(\omega_{|l,\mathbf{k}_2\rangle|m,\mathbf{k}\rangle} + \omega_2\right) - j\Gamma} \\ & - \left(\rho^{(0)}_{|l,\mathbf{k}_2\rangle} - \rho^{(0)}_{|n,\mathbf{k}_3\rangle}\right)\frac{\boldsymbol{\mu}_{|n,\mathbf{k}_3\rangle|l,\mathbf{k}_2\rangle}.\mathbf{E}(\omega_1)\mathbf{E}(-\omega_2).\boldsymbol{\mu}_{|l,\mathbf{k}_2\rangle|m,\mathbf{k}\rangle}}{\left(\omega_{|n,\mathbf{k}_3\rangle|l,\mathbf{k}_2\rangle} - \omega_1\right) - j\Gamma} \\ & - \left(\rho^{(0)}_{|l,\mathbf{k}_1\rangle} - \rho^{(0)}_{|n,\mathbf{k}_3\rangle}\right)\frac{\boldsymbol{\mu}_{|n,\mathbf{k}_3\rangle|l,\mathbf{k}_1\rangle}.\mathbf{E}(-\omega_2)\mathbf{E}(\omega_1).\boldsymbol{\mu}_{|l,\mathbf{k}_1\rangle|m,\mathbf{k}\rangle}}{\left(\omega_{|n,\mathbf{k}_3\rangle|l,\mathbf{k}_1\rangle} + \omega_2\right) - j\Gamma}\Bigg\}\frac{e^{-j\omega_d t}}{\omega_{|n,\mathbf{k}_3\rangle|m,\mathbf{k}\rangle} - \omega_d - i\Gamma}\end{aligned} \tag{A.30}$$

where Γ is the phenomenological factor showing the electron relaxation time, $\mathbf{k}_1 = \mathbf{k} + \mathbf{q}_{1||}$, $\mathbf{k}_2 = \mathbf{k} - \mathbf{q}_{2||}$, and $\mathbf{k}_3 = \mathbf{k} + \mathbf{q}_{1||} - \mathbf{q}_{2||}$. In writing the Eq. A.30, we used the fact that

$$\left\langle \Psi_{|\nu,\kappa'\rangle}\left|\mu.\mathbf{E}(\omega_1)\right|\Psi_{|l,\kappa\rangle}\right\rangle = \mu_{|\nu,\kappa+\mathbf{q}_1\rangle|l,\kappa\rangle}.\mathbf{E}(\omega_1) \tag{A.31}$$

$$\left\langle \Psi_{|\nu,\kappa'\rangle}\left|\mu.\mathbf{E}(-\omega_2)\right|\Psi_{|l,\kappa\rangle}\right\rangle = \mu_{|\nu,\kappa-\mathbf{q}_2\rangle|l,\kappa\rangle}.\mathbf{E}(-\omega_2) \tag{A.32}$$

where we used the conservation of momentum to find the right hand side and $\mu_{|\nu,\kappa'\rangle|l,\kappa\rangle}$ is given by:

$$\boldsymbol{\mu}_{|\nu,\kappa'\rangle|l,\kappa\rangle} = \langle \nu,\kappa'| - ie\nu_F \left(\sigma_x \hat{x} + \xi\sigma_y \hat{y}\right)/2 \,|l,\kappa\rangle \tag{A.33}$$

Substituting Eq. A.30 into Eq. A.12 and using the definition of Eq. A.13, one can find the second order nonlinearity tensor to be as follows:

$$\begin{aligned}
&\sigma^{(2)}_{sij}(\omega_1,-\omega_2,\mathbf{q}_1,-\mathbf{q}_2) \\
&= -\frac{e\nu_F}{2\pi^2\hbar^2\omega_1\omega_2}\sum_{n,m=1}^{2}\sum_{l=1}^{2}\int_{K,K'} d^2k_1 \Bigg\{ \left(\rho^{(0)}_{|m,\mathbf{k}_1\rangle} - \rho^{(0)}_{|l,\mathbf{k}_2\rangle}\right)\frac{\mu^i_{|l,\mathbf{k}_2\rangle|m,\mathbf{k}_1\rangle}\mu^j_{|n,\mathbf{k}_3\rangle|l,\mathbf{k}_2\rangle}}{\left(\omega_{|l,\mathbf{k}_2\rangle|m,\mathbf{k}_1\rangle} - \omega_1\right) - i\Gamma} \\
&+ \left(\rho^{(0)}_{|m,\mathbf{k}_1\rangle} - \rho^{(0)}_{|l,\mathbf{k}_{2'}\rangle}\right)\frac{\mu^j_{|l,\mathbf{k}_{2'}\rangle|m,\mathbf{k}_1\rangle}\mu^i_{|n,\mathbf{k}_3\rangle|l,\mathbf{k}_{2'}\rangle}}{\left(\omega_{|l,\mathbf{k}_{2'}\rangle|m,\mathbf{k}_1\rangle} + \omega_2\right) - i\Gamma} \\
&- \left(\rho^{(0)}_{|l,\mathbf{k}_{2'}\rangle} - \rho^{(0)}_{|n,\mathbf{k}_3\rangle}\right)\frac{\mu^i_{|n,\mathbf{k}_3\rangle|l,\mathbf{k}_{2'}\rangle}\mu^j_{|l,\mathbf{k}_{2'}\rangle|m,\mathbf{k}_1\rangle}}{\left(\omega_{|n,\mathbf{k}_3\rangle|l,\mathbf{k}_{2'}\rangle} - \omega_1\right) - i\Gamma} \\
&- \left(\rho^{(0)}_{|l,\mathbf{k}_2\rangle} - \rho^{(0)}_{|n,\mathbf{k}_3\rangle}\right)\frac{\mu^j_{|n,\mathbf{k}_3\rangle|l,\mathbf{k}_2\rangle}\mu^i_{|l,\mathbf{k}_2\rangle|m,\mathbf{k}_1\rangle}}{\left(\omega_{|n,\mathbf{k}_3\rangle|l,\mathbf{k}_2\rangle} + \omega_2\right) - i\Gamma}\Bigg\}\frac{\eta^s_{|m,\mathbf{5}k_1\rangle|n,\mathbf{k}_3\rangle}}{\omega_{|n,\mathbf{k}_3\rangle|m,\mathbf{k}_1\rangle} - \omega_d - i\Gamma}
\end{aligned} \tag{A.34}$$

It is worth noting that the tensor $\sigma^{(2)}_{sij}$ can be more simplified considering the fact that two incident beams are high energy while the generated photon in the difference process is weak. The high energy beams only contribute to the interband transition while the generated photon can only be the result of an intraband transition. Figure A.1 (a) shows all the transitions that can be involved in the DFG. By changing the naming convention for states as shown in Figure A.1 (b), it is possible to obtain a more concise form for $\sigma^{(2)}_{sij}$ as follows:

$$\begin{aligned}
\sigma^{(2)}_{sij} = -\frac{2e\nu_F}{\hbar^2\omega_1\omega_2}\int_{K,K'}\frac{d^2k_1}{4\pi^2}\Bigg\{\Bigg[&\frac{\rho^{(0)}_{\mathbf{k}_1} - \rho^{(0)}_{\mathbf{k}_2}}{(\omega_{\mathbf{21}} - \omega_1) - i\Gamma} \\
&- \frac{\rho^{(0)}_{\mathbf{k}_2} - \rho^{(0)}_{\mathbf{k}_3}}{(\omega_{\mathbf{32}} + \omega_2) - i\Gamma}\Bigg]\frac{\mu^i_{\mathbf{21}}\mu^j_{\mathbf{32}}\eta^s_{\mathbf{13}}}{\omega_{\mathbf{13}} - \omega_d - i\Gamma} + \Bigg[\frac{\rho^{(0)}_{\mathbf{k}_4} - \rho^{(0)}_{\mathbf{k}_1}}{(\omega_{\mathbf{14}} + \omega_2) - i\Gamma} \\
&- \frac{\rho^{(0)}_{\mathbf{k}_1} - \rho^{(0)}_{\mathbf{k}_2}}{(\omega_{\mathbf{21}} - \omega_1) - i\Gamma}\Bigg]\frac{\mu^j_{\mathbf{14}}\mu^i_{\mathbf{21}}\eta^s_{\mathbf{42}}}{\omega_{\mathbf{42}} - \omega_d - i\Gamma}\Bigg\}
\end{aligned} \tag{A.35}$$

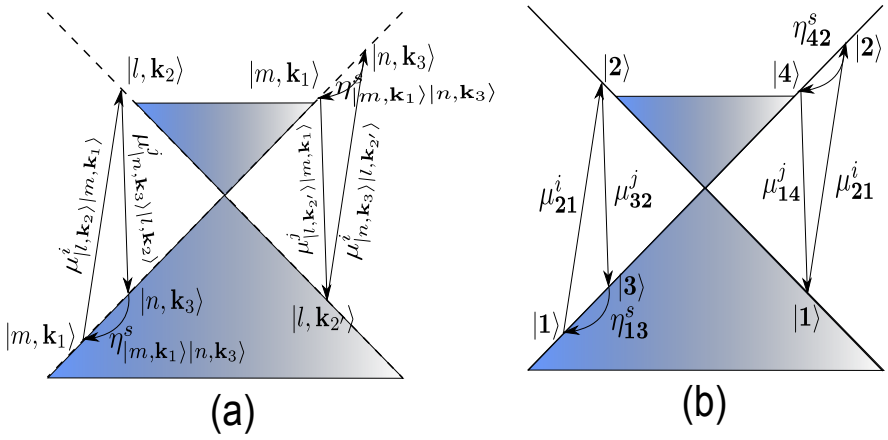

Figure A.1: (a) The schematic of transitions involved in the DFG process. (b) The same transitions using a new convention for naming the sates. The new convention makes the nonlinearity expression concise.

Figure A.2 shows the dependency of the nonlinear conductivity σ_{xyy} and σ_{xxx} to the incident wave vector. The drag-induced nonlinearity is a linearly function of the incident wave momentum.

A.4 The effect of DC biasing

The effect of DC current is to shift the Fermi surface and to cause a perturbation in the electron states. Assuming an induced shift $\Delta\mathbf{k}$ in the Fermi surface due to the change of initial electron states, the DC current can be obtained using the following transport formula:

$$\mathbf{J}^{dc} = g_s g_v \sum_{l=1}^{2} \int \mathbf{j}^e_{|l,\mathbf{k}\rangle} \left(\rho^{(0)}_{|l,\mathbf{k}-\Delta\mathbf{k}\rangle} - \rho^{(0)}_{|l,\mathbf{k}\rangle} \right) D(\mathbf{k}) T_{|l,\mathbf{k}\rangle} d^2k \tag{A.36}$$

where $\mathbf{J}^{dc}$ is the total DC current, $g_s = 2$ is the spin degeneracy, $g_v = 2$ is the valley degeneracy in graphene, $D(\mathbf{k}) = 1/(2\pi)^2$ is the 2D density of states, $\left(\rho^{(0)}_{|l,\mathbf{k}-\Delta\mathbf{k}\rangle} - \rho^{(0)}_{|l,\mathbf{k}\rangle} \right)$ is the per-

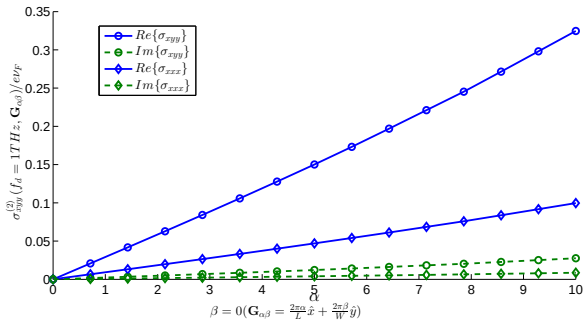

Figure A.2: The nonlinear conductivity of graphene for the difference frequency of $f_d = 1THz$ calculated as a function of the incident wave vector. The elements of second order conductivity tensor are a linear function of the incident wave momentum.

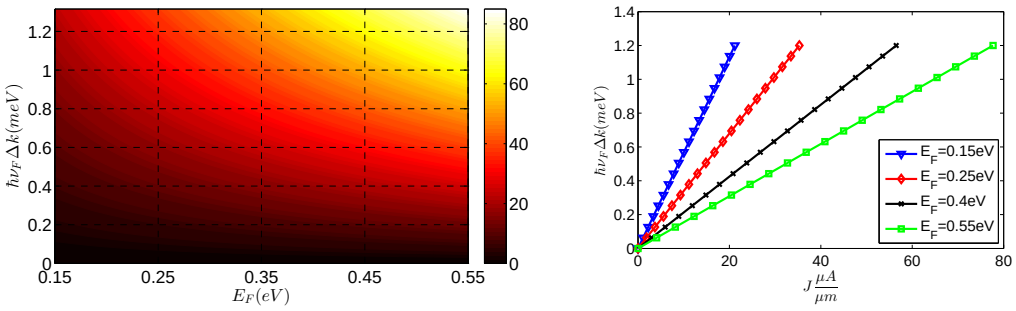

(a) (b)

Figure A.3: Dependency of $\hbar\nu_F\Delta k(meV)$ (a) and its slope (b) to the DC current for different values of the Fermi level.

turbation of the Fermi-Dirac distribution, $T_{|l,\mathbf{k}\rangle}$ is the transmission probability of the electron in state $|l,\mathbf{k}\rangle$ ($T_{|l,\mathbf{k}\rangle} = 1$ for ballistic transport), and $\mathbf{j}^e_{|l,\mathbf{k}\rangle} = e\nu_F(-1)^l\,[cos\theta_k\hat{x} + sin\theta_k\hat{y}]$ is the DC current due to an electron (or hole) with the momentum $\mathbf{p}_e = \hbar\mathbf{k}$. The value of $\mathbf{j}^e_{|l,\mathbf{k}\rangle}$ can be calculated using the following formula [17]:

$$\mathbf{j}^e_{|l,\mathbf{k}\rangle} = e\nu_F\,\langle l,\mathbf{k}|\,\sigma_x\hat{x} + \sigma_y\hat{y}\,|l,\mathbf{k}\rangle = e\nu_F(-1)^l\,[cos\theta_k\hat{x} + sin\theta_k\hat{y}] \tag{A.37}$$

Considering the fact that $\sum_{l=1}^{2}\int \mathbf{j}^e_{|l,\mathbf{k}\rangle}\rho^{(0)}_{|l,\mathbf{k}\rangle}D(\mathbf{k})T_{|l,\mathbf{k}\rangle}d^2k = 0$ and using the symmetry of the band-diagram, the Eq. A.36 can be written in a more concise form as:

$$\mathbf{J}^{dc}(\Delta\mathbf{k}) = g_s g_v \sum_{l=1}^{2}\int \mathbf{j}^e_{|l,\mathbf{k}\rangle}\rho^{(0)}_{|l,\mathbf{k}-\Delta\mathbf{k}\rangle}D(\mathbf{k})T_{|l,\mathbf{k}\rangle}d^2k \tag{A.38}$$

Eq. A.38 can be used to find the relation between the shift in the Fermi surface and the DC current. Figure A.3a shows the dependency of the Δk on the current density for different values of the Fermi level. As can be seen in Fig. A.3b, the slope $J_{dc}/\Delta k$ increases as the Fermi level increases. It is worth mentioning that because of the symmetry in the band-diagram, the dependency of J_y to Δk_y is identical to the dependency of J_x on Δk_x.

Appendix B

B.1 The active region modeling

A successful design of a photomixer antenna needs the accurate modeling of graphene active region. The main purpose of such a characterization is to obtain the impedance between two metal contacts of antenna. The impedance of the gap between antenna plays an important role in the efficiency and total gain of antenna. To have an exact model, the effect of electromagnetic field is considered as a perturbation in the steady-state current flow of electrons in graphene. Here we suppose that the time-varying applied potential has a linear profile in graphene layer. Assuming that one of the contacts is grounded the potential of the other contact can be written as:

$$U(t) = U_1 e^{-i\omega t} + U_1 e^{i\omega t} \tag{B.1}$$

where $\omega/2\pi$ and U_1 are the frequency and the amplitude of electromagnetic field. Because of the time periodicity of applied field the electron wave-function in graphene should be:

$$\psi(x, y, t) = \sum_n \psi_n(x, y) e^{-i(\mathcal{E}+n\hbar\omega)t/\hbar} \tag{B.2}$$

where $\psi_n(x, y)$s are the coefficients of $e^{-i(\mathcal{E}+n\hbar\omega)t/\hbar}$ time-harmonics. Assuming a linearly increasing potential inside the gap, the Dirac equation can be written as:

$$\begin{aligned} \nu_F(\hat{p}_x - i\hat{p}_y)\psi^B + U(t)\frac{x}{l}\psi^A &= i\hbar\partial_t\psi^A \\ \nu_F(\hat{p}_x + i\hat{p}_y)\psi^A + U(t)\frac{x}{l}\psi^B &= i\hbar\partial_t\psi^B \end{aligned} \tag{B.3}$$

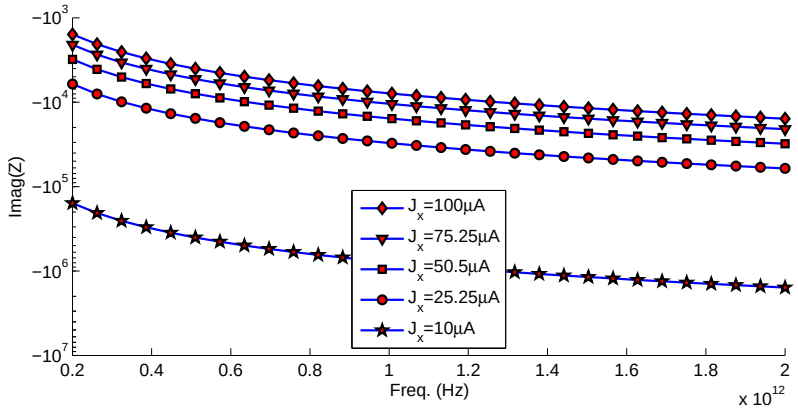

Figure B.1: The imaginary part of gap impedance of graphene active region as a function of DC current ($\mathcal{E} = 100meV$). The real part of graphene is approximately zero.

By substituting the Eq. B.2 into the Dirac equation, one may obtain the following set of equations:

$$\begin{aligned}
\nu_F(\hat{p}_x - i\hat{p}_y)\psi_n^B + \frac{x}{l}U_1\psi_{n-1}^A + \frac{x}{l}U_1\psi_{n+1}^A &= (\mathcal{E} + n\hbar\omega)\psi_n^A \\
\nu_F(\hat{p}_x + i\hat{p}_y)\psi_n^A + \frac{x}{l}U_1\psi_{n-1}^B + \frac{x}{l}U_1\psi_{n+1}^B &= (\mathcal{E} + n\hbar\omega)\psi_n^B
\end{aligned} \tag{B.4}$$

Since the amplitude of time-varying field is negligible comparing to the DC current for the case of photomixer, the first order current in graphene is only the DC current:

$$\begin{pmatrix}\psi_0^A \\ \psi_0^B\end{pmatrix} = \frac{1}{\sqrt{(2)}}\begin{pmatrix}e^{-i\phi/2} \\ e^{i\phi/2}\end{pmatrix} e^{i\vec{p}_0.\vec{r}}, \quad \nu_F \left\|\vec{p}_0\right\| = \mathcal{E} \tag{B.5}$$

Substituting Eq. B.5 into the Eq. B.4, one can obtain:

$$\begin{aligned}
&\nu_F^2(\hat{p}_x + i\hat{p}_y)(\hat{p}_x - i\hat{p}_y)\psi_1^B + \frac{U_1}{l}\nu_F(\hat{p}_x + i\hat{p}_y)\left\{x\psi_0^A\right\} \\
&= (\mathcal{E} + n\hbar\omega)\left\{(\mathcal{E} + n\hbar\omega)\psi_1^B - \frac{x}{l}U_1\psi_0^B\right\} \\
&- \hbar^2\nu_F^2\nabla^2\psi_1^B - (\mathcal{E} + n\hbar\omega)^2\psi_1^B - i\hbar\frac{U_1}{l}\nu_F\psi_0^A + \frac{x}{l}U_1\mathcal{E}\psi_0^B \\
&= -(\mathcal{E} + n\hbar\omega)\frac{x}{l}U_1\psi_0^B
\end{aligned} \tag{B.6}$$

After solving the equation Eq. B.6 for ψ_1^A and ψ_1^B (Here we suppose that the second order nonlinearity is negligible comparing to the linear response):

$$\psi_1^{A(B)} = \phi_1^{A(B)} e^{i\vec{p}_1.\vec{r}/\hbar}, \quad \nu_F \left\|\vec{p}_1\right\| = \mathcal{E} + \hbar\omega$$
$$\phi_1^{A(B)} = C_2^{A(B)} x e^{i\vec{P}.r/\hbar} + C_3^{A(B)} e^{i\vec{P}.r/\hbar} \tag{B.7}$$

where

$$\vec{P} = \vec{p}_0 - \vec{p}_1$$
$$C_2^{A(B)} = -\frac{\beta^{A(B)}\hbar^2}{2\vec{p}_1.\vec{P} + \left|\vec{P}\right|^2}$$
$$C_3^{A(B)} = -\frac{\alpha^{A(B)}\hbar^2}{2\vec{p}_1.\vec{P} + \left|\vec{P}\right|^2} + \frac{2\hat{x}.(\vec{p}_1 + \vec{P})\beta^{A(B)}\hbar^3 i}{\left(2\vec{P}_1.\vec{P} + \left|\vec{P}\right|^2\right)^2} \tag{B.8}$$

and

$$\left(\alpha^B\right)^* = \alpha^A = \frac{-iU_1 e^{i\phi/2}}{\sqrt{2}l\hbar\nu_F}, \quad \left(\beta^B\right)^* = \beta^A = \frac{(2\mathcal{E} + \hbar\omega)U_1 e^{-i\phi/2}}{\sqrt{2}l\hbar^2\nu_F^2}. \tag{B.9}$$

The linear response of system can be written as:

$$J_x = 2e\nu_F \mathcal{R}\left\{\psi_0^B \psi_1^{A*} e^{i\omega t} + \psi_0^B \psi_{-1}^{A*} e^{-i\omega t} + \psi_0^A \psi_1^{B*} e^{i\omega t} + \psi_0^A \psi_{-1}^{B*} e^{-i\omega t}\right\}$$

The impedance between leads can be obtained as a function of carrier density. The carrier density, on the other hand, can be obtained from the DC current. So, one can write:

$$|Z(\omega)| = |U1/(J_x J_{x0})| \tag{B.10}$$

where Z is the impedance of antenna gap. It should be noted that the input impedance can be measured as a function of DC current (an approximate value of the Fermi energy level is enough to evaluate the input impedance). Another interesting point is the factor $2\vec{p}_1.\vec{P} + \left|\vec{P}\right|^2$ which determines the amplitude of current. According to this factor the relative angle between DC and AC current also affect the input impedance of antenna. For the case of photo-mixer both currents are in the same direction. Fig. B.1 shows the impedance of active region as a function of DC current.